Seismic data processing with an expanded Common Reflection Surface workflow

Dissertation

Zur Erlangung des Doktorgrades der
Naturwissenschaften im Department Geowissenschaften
der
Universität Hamburg

vorgelegt von

Stefan Dümmong

aus

Wedel

Hamburg
2010

Als Dissertation angenommen vom Department Geowissenschaften der Universität Hamburg

Auf Grund der Gutachten von Prof. Dr. Dirk Gajewski
und PD Dr. Christian Hübscher

Hamburg, den 03. Februar 2010

Prof. Dr. Jürgen Oßenbrügge
Leiter des Departments für Geowissenschaften

Seismic data processing with an expanded Common Reflection Surface workflow

Stefan Dümmong

email: *sdu@statoil.com*

keywords: *Seismic imaging; multiparameter stacking; multiple attenuation; Eastern Mediterranean*

Contents

ABSTRACT

The so-called CRS workflow is a processing scheme for seismic data based on the kinematic wavefield attributes estimated during the Common Reflection Surface (CRS) stack, the so-called CRS attributes. I extended the CRS workflow with a multiple suppression tool and incorporated the prestack data enhancement tool by Baykulov and Gajewski (2009a). The introduced expanded CRS workflow contains a multiparameter stacking tool, the CRS stack, a multiple attenuation tool based on CRS attributes, a prestack data enhancement technique by means of partial CRS stacks, a tomographic tool also based on CRS attributes, and a subsequent time or depth migration algorithm. This quick and stable processing workflow allows to produce data of enhanced quality for reliable post- and prestack depth migrations, suppress multiple reflections in the data, and generates a velocity model for an initial depth migration. The CRS stack theory will be reviewed in the first chapter of the thesis. Afterwards, the newly developed multiple attenuation tool will be discussed in detail. Additionally, it will be also shown how the prestack data enhancement tool can be incorporated into the CRS workflow and how it serves as an interface for achieving the data condition requirements of other non CRS related methods. Furthermore, NIP-wave tomography will be discussed and compared to another tomographic tool in a complex geological setting. To illustrate the potential of this workflow, results of an imaging project on a marine industry data set from the Eastern Mediteranean / Levantine basin will be presented throughout the thesis. The results are satisfying and allowed a detailed geologic interpretation based on depth migrated sections of the data set, which is presented in the last chapter.

1 INTRODUCTION

The CRS workflow (Hertweck et al., 2007a) is a powerful tool for a stable and quick seismic data processing chain from time to depth imaging. It relies on a hyperbolic second order approximation of the reflection response. Currently, it consists of the Common Reflection Surface (CRS) stack (Mann, 2002), the Normal Incidence Point (NIP)-wave tomography (Duveneck, 2004b), and a corresponding post- or prestack depth migration algorithm.
The CRS stack is a multiparameter stacking method. Due to the fact that it considers a hyperbolic surface instead of a hyperbola, it can produce superior results compared to the conventional Common Midpoint (CMP) stack in terms of signal to noise (S/N) ratio. The determined stacking parameters serve as input data for the so-called NIP-wave tomography. NIP-wave tomography generates from CRS attributes a migration velocity model that can be used for further processing tasks, e.g., time or depth imaging projects. It determines the model in an inversion process. The input parameters for NIP-wave tomography are estimated in the poststack data domain, which simplifies the input data generation significantly. Due to the fact, that only poststack input data instead of prestack input data is considered, NIP-wave tomography generates faster a reliably velocity model than other tomography methods relying on traveltime only.

Some of the facts that hamper the application of this workflow are insufficient data quality, data sparseness in terms of receiver and source distribution along the measurement surface, and multiple reflections present in the data. The first two factors reduce the applicability of any method and influence the quality of the resulting section negatively. The third factor, i.e., multiple reflections directly reduce the applicability of the methods in the CRS workflow, due to the fact that they mask primary reflections in the data, which then cannot be properly described by the CRS attributes, i.e., the stacking parameter. Even worse, if they are considered unwanted, the subsequent NIP-wave tomography process is likely to produce unphysical results, because it can only handle primaries correctly.

To overcome these drawbacks, a prestack data enhancement tool was presented by Baykulov and Gajewski (2009a) and initial approaches to address multiples within the CRS workflow were presented by Gamboa et al. (2003) and Dümmong and Gajewski (2008). In this work, we incorporate these tools into the CRS workflow and further develop the multiple attenuation approach after Dümmong and Gajewski (2008) to obtain an integrated and reliable processing chain (see Figure 1). The resulting expanded CRS workflow can be applied directly on preprocessed data (i.e., geometry processed and denoised data). The final result of the CRS workflow is an initial depth migrated image, which can be refined by a subsequent residual moveout velocity analysis. The individual items of the expanded CRS workflow can also be combined depending on the objective of the processing project. Single items of this workflow can also be used in processing chains compromising non-CRS related tools.

In the following chapters, we will discuss the individual items of the expanded CRS workflow. We will first review the derivation of the CRS stacking formula which is obtained with the help of a second order Taylor expansion of the square of the traveltime. Additionally, we also discuss the current implementations, i.e., the so-called pragmatic search strategies, after Mann (2002) and Müller (2007) and present ways to introduce geological constrained parameter searches into the stacking parameter determination.

Afterwards, we take a look at the development of the surface related multiple attenuation approach in the frame of the CRS workflow. Two approaches for multiple attenuation within the CRS workflow are developed and implemented in this thesis. One tool focus on a fast prediction of multiple reflections in the poststack data domain, i.e., the CRS stacked domain, and afterwards generates prestack seismograms of the identified multiples with the help of their CRS attributes. The seismograms are then adaptively filtered and subtracted from the original data. The second tool for multiple attenuation focusses more on achieving the requirements of Surface Related Multiple Elimination (SRME) (Verschuur et al., 1992). Here, total regularity of the data in terms of source and receiver spacing is required, which makes it difficult to directly incorporate this technique into existing workflows. We are presenting an approach for regularising the prestack data to meet the needs of SRME with the help of partial CRS stacks. These locally performed multiparameter stacks allow to interpolate missing traces for a subsequent application of SRME. Results

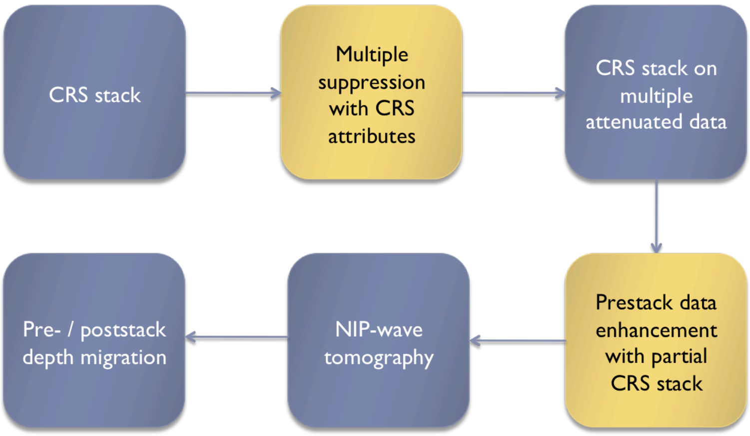

Figure 1: Schematic illustration of the expanded CRS workflow, a new multiple attenuation and a prestack data enhancement tool is added (highlighted yellow).

of the multiple attenuation approaches will be presented on two marine data sets. One data set is a short streamer academic acquisition offshore the Maldives Islands and one is a industry data set from the Eastern Mediterranean / Levantine basin.

Afterwards, we concentrate on the application of the CRS stack and NIP-wave tomography in complex geological situations. We discuss the abilities of velocity model building of NIP-wave tomography in comparison with prestack stereotomography (Billette and Lambaré, 1998) in complex geological situations. As mentioned before NIP-wave tomography is based on wavefield attributes obtained during the Common Reflection Surface (CRS) stack, and thus on the underlying hyperbolic second-order traveltime approximation. In contrast to that prestack stereotomography describes traveltimes by local slopes (i.e., linearly) in the prestack data domain. To analyse the impact of the different traveltime approximations and the different input data domains on velocity model building we have applied two implementations of these techniques to two profiles of the marine data-set from the Levantine Basin / Eastern Mediterranean.

Following this, the potential for seismic imaging of the expanded CRS workflow is illustrated by an geologic interpretation of the data from the Eastern Mediterranean. Here, we processed the whole industry data set from the Eastern Mediterranean / Levantine basin with the introduced expanded CRS workflow or a slightly modified version of it. The consequent last step was then to perform a depth migration project, where we used a Kirchhoff depth migration algorithm for imaging the subsurface structures. For this purpose, we used velocity models determined by NIP-wave tomography. Since the obtained Common Image gathers (CIGs) already showed a good flatness, which indicates a good quality of the obtained model, we used the results for a subsequent geological interpretation directly on the resulting depth sections. Additionally to these results, we also had access other marine seismic surveys from the University of Hamburg, a 3D seismic data cube from the University of Minnesota, and satellite data from ARK Geophysical company, which completed the data basis for the interpretation project. The so obtained results confined the stratigraphic model for the Messinian evaporates after Hübscher and Netzeband (2007a). Additionally, the results lead to new insights into the salt tectonics of the Messinian salt layer, the behaviour of deep rooted fault systems, and the deep basin structure in the Eastern Mediterranean / Levantine basin.

2 GEOLOGICAL CONSTRAINS IN THE CRS PARAMETER SEARCH

2.1 Introduction

After acquisition and preprocessing (i.e., geometry processing and denoising) of seismic data, stacking is the next step in the seismic data processing chain. Here, the concept of covering one subsurface element with many seismic rays (multicoverage data) is exploited. This means, that redundant information belonging to the same subsurface element is searched and stacked coherently together. The measure used within the stacking process for the coherency evaluation of the data is usually semblance (Neidell and Taner, 1971). The traveltime of a seismic ray between a source and a receiver is not equal for varying offsets between source and receiver pairs. The time difference between the varying source and receiver pairs is called Normal Moveout (NMO). In a second order approximation, the traveltimes of a seismic reflection event can be described in a hyperbolic way (Hubral and Krey, 1980). This means, that a reflection event can be approximated by a hyperbola, which can be described by one or more stacking parameters. This forms the basis of the so-called Normal Moveout (NMO) velocity analysis, which basically aims at removing the NMO of the seismic reflection event.
Before the NMO velocity analysis, the data is sorted into Common Midpoint (CMP) gathers, i.e., all traces having approximately the same midpoint between different source and receiver pairs in the data. Afterwards, the semblance value of a certain reflection event inside a CMP gather is estimated by fitting a hyperbola to the data. For a single horizontal layer, the hyperbolic assumption is exact. In an arbitrary medium, this is generally not fulfilled and the traveltime curve is approximated. The fitted hyperbola is described by one parameter, the so-called stacking velocity.
During the NMO velocity analysis, the following procedure is repeated: For every CMP position and reflection event, a hyperbola is fitted to the data in such way, that the semblance value for this event is maximised. This, combined with sorting the data into CMPs is the so-called CMP concept (Mayne, 1962). An extension of the CMP concept is the Common Reflection Surface (CRS) stack (e.g., Müller (1999); Mann (2002)), where the traveltime is no longer approximated by a hyperbola, but by a hyperbolic surface, i.e., three stacking parameters have to be searched instead of one. Due to the fact, that a hyperbolic surface described in offset and midpoint cordinates has an also extension covering neighboring CMP positions, more than one CMP is normally considered in the CRS stacking process. This means, that a hyperbolic surface is fitted to the data, NMO corrected, and stacked in the corresponding zero offset position of the data. This process results in an enhancement of the stacking fold, and therefore in a higher signal to noise ratio in the corresponding stacked section.
The CRS stacking procedure is implemented as a three dimensional semblance optimisation (e.g., Mann (2002); Müller (2007)), whereas in 3D it is a eight dimensional optimisation. In the existing implementations the parameter estimation is split up in subsequent lower dimensional semblance optimisations for special geometrical configurations, which reduces the computational costs of the method, especially in 3D. Due to the automated implementation of the optimisations, physical unreasonable stacking parameter determinations occur in areas of low coherency, i.e., where no or weak reflection events are present. In these circumstances, the algorithms hardly ever determines geological reasonable parameters. To overcome this limitation, we will introduce parameter search strategies that can be linked to geological features. These features may be known before the processing starts, which will then lead to a geological constrained parameter estimation.

In the following, we will review the underlying CRS theory, describe the current implementation, and introduce geological constrained parameter searches into the CRS parameter optimisations. Finally, we will show results of an initial test of these attempts on a marine industry data set from the Eastern Mediterranean / Levantine Basin.

2.2 Theory of the CRS stack

In the following we will review the derivation of the CRS stacking formula. The formula can be obtained by a Taylor expansion of the square of the traveltime t up to second order

$$\begin{aligned} t^2(s_i, g_i) = t_0^2 + \frac{\partial t^2}{\partial s_i}\triangle s_i + \frac{\partial t^2}{\partial g_i}\triangle g_i + \frac{\partial^2 t^2}{\partial s_i \partial g_i}\triangle s_i \triangle g_i + \\ \frac{1}{2}\frac{\partial^2 t^2}{\partial s_i \partial s_j}\triangle s_i \triangle s_j + \frac{1}{2}\frac{\partial^2 t^2}{\partial g_i \partial g_j}\triangle g_i \triangle g_j + \theta(3) \end{aligned} \tag{1}$$

with s_i and g_i the source and receiver coordinates, respectively. t_0 is the zero offset traveltime. When we apply the chain and product rule and resort the equations we arrive at

$$\begin{aligned} t^2(s_i, g_i) = t_0^2 + \frac{\partial^2 t^2}{\partial s_i \partial s_j}\triangle s_i \triangle s_j + \frac{\partial^2 t^2}{\partial g_i \partial g_j}\triangle g_i \triangle g_j + \\ 2t_0 \frac{\partial t}{\partial s_i}\triangle s_i + 2t_0 \frac{\partial t}{\partial g_i}\triangle g_i + 2\frac{\partial^2 t^2}{\partial s_i \partial g_j}\triangle s_i \triangle g_j + \\ t_0(2\frac{\partial^2 t}{\partial s_i \partial g_j}\triangle s_i \triangle g_j + \frac{\partial^2 t}{\partial s_i \partial s_j}\triangle s_i \triangle s_j + \\ \frac{\partial^2 t}{\partial g_i \partial g_j}\triangle g_i \triangle g_j). \end{aligned} \tag{2}$$

Finally, we simplify the equation and obtain the same result as already described in Vanelle (2002)

$$\begin{aligned} t^2(s_i, g_i) = (t_0 + \frac{\partial t}{\partial s_i}\triangle s_i + \frac{\partial t}{\partial g_i}\triangle g_i)^2 + \\ t_0(2\frac{\partial^2 t}{\partial s_i \partial g_j}\triangle s_i \triangle g_j + \frac{\partial^2 t}{\partial s_i \partial s_j}\triangle s_i \triangle s_j + \\ \frac{\partial^2 t}{\partial g_i \partial g_j}\triangle g_i \triangle g_j). \end{aligned} \tag{3}$$

We now define the abbreviations:

$$a = -\frac{\partial t}{\partial s_i} \quad \text{and} \quad b = \frac{\partial t}{\partial g_i} \tag{4}$$

as well as

$$C = -\frac{\partial^2 t}{\partial s_i \partial g_j}, \quad D = -\frac{\partial^2 t}{\partial s_i \partial s_j} \quad \text{and} \quad E = \frac{\partial^2 t}{\partial g_i \partial g_j}. \tag{5}$$

With the above mentioned abbreviations equation (3) simplifies further to

$$\begin{aligned} t^2(s_i, g_i) = (t_0 - a\triangle s + b\triangle g)^2 + \\ t_0(2C\triangle s\triangle g - D\triangle s^2 + E\triangle g^2), \end{aligned} \tag{6}$$

which corresponds to the so-called general NMO formula (Vanelle, 2002). The equation was derived by approximating the traveltime with a second order Taylor series and is therefore valid in an arbitrary medium assuming hyperbolic moveout.

We can now substitute the source and receiver coordinates s and g with the midpoint x_m and half offset h coordinate

$$x_m = \frac{g+s}{2} \quad \text{and} \quad h = \frac{g-s}{2}. \tag{7}$$

The general NMO formula then reads

$$\begin{aligned} t^2(x_m,h) = (t_0 - a(x_m-h) + b(x_m+h))^2 + \\ t_0(2C(x_m-h)(x_m+h) - D(x_m-h)^2 + \\ E(x_m+h)^2). \end{aligned} \tag{8}$$

When we simplify this equation, we obtain the general NMO formula in midpoint and half offset coordinates

$$\begin{aligned} t^2(x_m,h) = (t_0 + (b-a)x_m + (b-a)h)^2 + \\ t_0(x_m^2(2C-D+E) + h^2(-2C-D+E) + \\ 2x_m h(D+E)). \end{aligned} \tag{9}$$

As mentioned before, this formula is valid for every acquisition configuration. When we move to the zero offset case, which is considered in this paper, we can introduce symmetry relations for some parameters. Due to the reciprocity of the ray path and by assuming monotypic waves, we can write:

$$a = -b \quad \text{and} \quad D = -E. \tag{10}$$

Inserting this into the general NMO formula in midpoint and half offset coordinates (equation 9), we obtain the Taylor expansion of the squared traveltime for a zero offset configuration, which corresponds to the CRS formula

$$\begin{aligned} t^2(x_m,h) = (t_0 + 2bx_m)^2 + \\ t_0((2C+2E)x_m^2 + (2E-2C) + h^2). \end{aligned} \tag{11}$$

When we now introduce the following abbreviations

$$b = \frac{sin(\beta_0)}{v_0} \tag{12}$$

$$C + E = \frac{cos^2(\beta_0)K_N}{v_0} \tag{13}$$

$$E - C = \frac{cos^2(\beta_0)K_{NIP}}{v_0}, \tag{14}$$

we get the conventional CRS formula given by Jäger et al. (2001):

$$\begin{aligned} t^2(x_m,h) = (t_0 + \frac{2sin(\beta_0)}{v_0}\triangle x_m)^2 + \\ \frac{2t_0cos^2(\beta_0)}{v_0}(K_N\triangle x_m^2 + K_{NIP}\triangle h^2), \end{aligned} \tag{15}$$

in which v_0 can be associated with the near surface velocity, β_0 with the angle of emergence for the considered zero offset ray, K_N with the so-called Normal-wave curvature, and K_{NIP} with the Normal-Incidence-Point-wave curvature. The latter two parameters can be seen as combinations of second order derivatives of the traveltime with respect to different coordinates, but they can also be interpreted as wavefront curvatures from artificial experiment configurations. The Normal-wave can be seen as a wave front emerging from a circular exploding reflector element in depth and the Normal-Incidence-Point-wave can be interpreted as a wave front emerging from a point source at the Normal-Incidence-Point on the considered reflector (for more details, see Hubral and Krey (1980)).

The CRS formula (equation 15) describes a hyperbolic surface (see Figure 2 for an illustration of the CRS operator) which is parameterized in midpoint and half offset coordinates and can therefore be used as a stacking operator, that also considers the moveout towards neighbouring CMP locations (midpoints). This leads to some consequences for the resulting stacked section. First of all, due to the fact that neighbouring CMPs are also considered more traces can be taken into account, i.e., the stacking fold is enhanced. This results in a better signal to noise (S/N) ratio in the final stacked section, which will be superior compared to a conventional CMP stacked section (Mann, 2002). Additionally, the CRS stack produces the so-called CRS attributes, which form the basis for subsequent applications, which will be described later on.

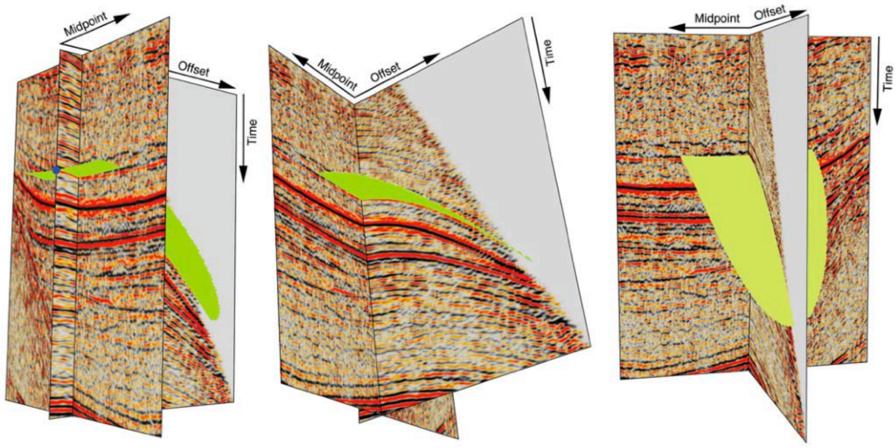

Figure 2: The hyperbolic CRS stacking operator in midpoint and half offset coordinates after Hertweck et al. (2007b).

The stacking operator can not be arbitrary enlarged, because we have approximated the travetime with a second order Taylor series expansion. Therefore, we have to restrict the spatial extend of the CRS operator. For the midpoint coordinate, the extend of the operator can be expressed in terms of the first projected Fresnel zone (Mann, 2002), which corresponds to the lateral resolution of a seismic wave. The projected Fresnel zone around a receiver at the surface can be expressed as (e.g., Schleicher et al. (1997)):

$$| t_D(x) - t_R(x) | \leq \frac{T}{2}, \tag{16}$$

where t_D is the traveltime of a diffraction, t_R the traveltime of a reflection, and T the main period of the considered signal. To simplify this description in a way that can be directly applied to the CRS stacking case, Mann (2002) showed that the size of the projected Fresnel zone W_F can also be approximated by

$$W_F = v\sqrt{\frac{T^2}{4} + Tt_0} \approx v\sqrt{Tt_0}. \tag{17}$$

In this equation a homogeneous half space is assumed and v corresponds to the average velocity in the overburden.

For the half offset coordinate no such explicit or approximate formula can be given. Here, we have to use a rule of thumb of a target to offset ratio of approximately $1:1$. The spatial extend of the CRS stacking operator is called aperture.

2.3 Implementation

The following description mainly focusses on the implementations of Mann (2002) and Müller (2007). We restrict the description to the 2D case, but it is straight forward to extend the approaches to the 3D case, as it was also done by Müller (2007).

The implementation of the 2D CRS stack is realised as a three (in 3D eight) parameter optimisation algorithm. By fitting a hyperbolic surface to the data, the semblance is optimised for every sample in the considered CMP gather. Semblance is defined after Neidell and Taner (1971) as:

$$S = \frac{\sum_{j=-W/2}^{W/2} \left(\sum_{i=1}^{N} f_{i,j+k(i)} \right)^2}{N \sum_{j=-W/2}^{W/2} \sum_{i=1}^{N} f_{i,j+k(i)}^2} \tag{18}$$

Here $f_{i,j}$ denotes the amplitude of the j^{th} sample of the i^{th} of N traces. A time window of width W is defined around the CRS operator at $k(i)$. A good choice for the length of the time window is the dominant period in the data.
A drawback of the semblance criterion is the assumption of constant amplitude and phase along the stacking operator. In reality this is not always fulfilled, due to the fact that the reflection coefficient is angle dependent. Gelchinsky et al. (1985) present several alternative coherency criteria, which incorporate this fact correctly. Nevertheless, semblance is widely used, since the alternative coherency criteria are computationally more expensive.

The simultaneous optimisation of three parameters is a challenging task. Currently, no implementation exists that simultaneously optimises all three parameters right from the start. Approaches to tackle this problems are under development, e.g., the method suggested by Santos et al. (2008) for a fast CRS parameter estimation could be used for a good starting parameter set for a subsequent multidimensional optimisation.
The current implementation simplifies the parameter search. The CRS operator is considered in typical acquisition geometries, this reduces the number of parameters to determine and speeds up the calculation. This approach is called the pragmatic search strategy (Mann, 2002). This search strategy and how to incorporate geological constrains into the subsequent searches will be discussed in the following.

CMP search In the initial step of the CRS stack the CMP configuration is considered, i.e., $x_m = 0$. Equation (15) reduces to a formula with two unknowns, the angle β_0 and the NIP-wave curvature:

$$t^2(x_m, h) = t_0^2 + \frac{2t_0 cos^2(\beta_0) K_{NIP}}{v_0} h^2. \tag{19}$$

This equation can be simplified via the equation

$$\frac{t_0 cos^2(\beta_0) K_{NIP}}{v_0} = \frac{2}{v_{NMO}^2} \tag{20}$$

to the conventional NMO formula

$$t^2(x_m, h) = t_0^2 + \frac{4h^2}{v_{NMO}^2}. \tag{21}$$

Thus, the first step of the pragmatic parameter search strategy reduces to conventional stacking velocity analysis. Due to the fact, that the parameter is estimated in an automatic way by semblance optimisation, the stacking velocity is determined for every sample in the data set. This is done by performing a grid search with varying stacking velocity intervals, i.e., one stacking velocity interval is defined for the minimum time in the data and one for the maximum, in between the intervals are interpolated linearly. Then grid searches are performed in these intervals to detect the best stacking velocity for every ZO sample.

Introducing geological parameter constrains in an automated way at this step of the CRS parameter determination is quite complicated and not straight forward. One way to introduce geologically reasonable constrains to the search would be to avoid the automatic determination of stacking velocities of coherent noise (e.g., multiples). This can be done by incorporating only certain stacking velocity ranges as guides from previous processing steps. These guide velocities would have to be picked manually according to the expected geological situation. However, the elimination of multiples before the stacking process would lead to better parameter determinations and is highly recommended.

To restrict the parameter search without manual user interaction, i.e., velocity picking, we have to make assumptions on the geological situation. One generally quite often used criteria is, that the stacking velocity only increases or stays constant with increasing time. Transferred to the geological situation, this means that the sediments in the subsurface produce no negative velocity contrast (i.e., velocity inversion) of such a strength that the stacking velocity decreases. This is fulfilled in a high number of circumstances, thus the assumption of a general increasing or constant stacking velocity can be applied to a wide range of geological situations.
To incorporate this in an automated parameter determination, we implemented a so-called dynamic stacking velocity range in the parameter search. We can restrict the lower boundary of the stacking velocity search interval to the determined stacking parameter of the previous sample. However, in the case of an erroneous parameter estimation, this procedure is likely to produce erroneous results. Therefore, we only adjust the lower stacking velocity boundary of events with a high semblance value (see Figure 3 for an illustration of the scheme). Under the assumption of only increasing or constant stacking velocities, this means that we dynamically restrict the stacking velocity ranges in a data oriented way. This will provide a more reasonable stacking velocity estimation, when a guide file is not available. Additionally, it prevents the automatic algorithm from fluctuating parameter determination in the water column, stacking up multiples coherently, and large parameter fluctuations in deeper parts of seismic sections with low S/N ratios. For low coherent events, e.g. for bad quality land data, the algorithm will not introduce restrictions to the search intervals.

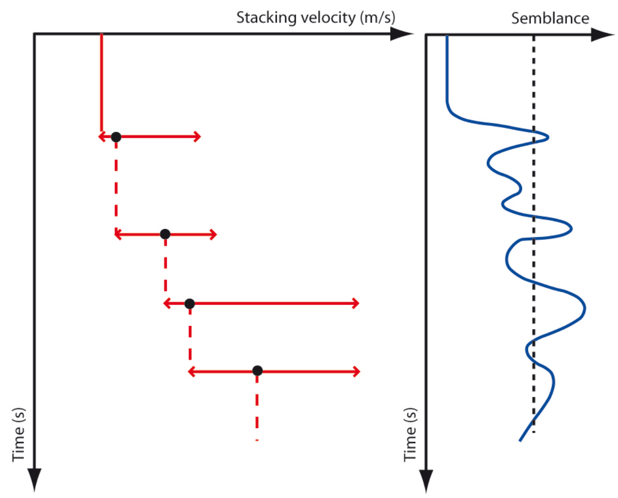

Figure 3: Schematic illustration of the dynamic stacking range implementation. Every time an event reaches the coherence threshold (dotted black line), the lower boundary of the stacking velocity search interval is adjusted.

Zero offset search The second parameter search will be done in the zero offset configuration, i.e., $h = 0$. This means the parameters are determined in the poststack data domain, e.g., in the stacked section of the previous search. Here, one drawback of the pragmatic search strategy becomes visible. In the case of an automatically generated low quality CMP stacking result, the following ZO searches will not determine good parameters either. To avoid this, one could produce a CMP stacking result manually in the conventional way. With careful investigation and processing experience, a sufficient stacking result in terms of image quality might be achieved and the subsequent searches would benefit from that.

Similar to the CMP search, the stacking parameters of the ZO search are determined by grid searches optimising the semblance. These searches are again restricted by varying parameter intervals. In the zero offset case, equation (15) reduces to

$$t^2(x_m, h=0) = (t_0 + \frac{2sin(\beta_0)}{v_0} x_m)^2 + \frac{2t_0 cos^2(\beta_0) K_N}{v_0} x_m^2. \tag{22}$$

In this equation two parameters are unknown. The simplifying assumption of a plane wave, i.e., $K_N = 0$ (Hubral and Krey, 1980), leads to the equation:

$$t^2(x_m, h=0)_{K_N=0} = (t_0 + \frac{2sin(\beta_0)}{v_0} x_m)^2. \tag{23}$$

Based on this, the angle of emergence can be determined in a one parameter optimisation. Afterwards the Normal-wave curvature can be determined with equation(22). Please note, that for a reliable estimation of K_N the aperture for the second optimisation have to be enlarged compared the to determination of the angle of emergence. Otherwise, K_N will be determined as approximately zero, due to the fact that equation (23) already determined the optimal fit of the stacking operator for this aperture. Finally, the remaining CRS parameter, i.e., the NIP-wave curvature, can be calculated with the help of the angle of emergence and the stacking velocity (via equation(20)).

Geological constrains to restrict the parameter searches can be introduced quite well during the zero offset optimisations, because the basis for the searches is a stacked section, which already provides indications on the geological situation. Dominant structural information can be derived and incorporated into the parameter estimations. Since the angle of emergence is a direct indication on the time dip of the considered reflection, the angle of emergence determination can be restricted to a certain angle intervals. Without a good restriction, especially in areas of bad signal to noise ratio, steep dipping noise events might be detected, that do not correspond to the geological situation. In Figure 4 such a situation is displayed. In this data set from the North German Basin, we hardly see geological structures in the section, but some coherent steep dipping events are imaged (from Baykulov et al. (2008)). From geological knowledge we can expect more or less horizontal events in this case. In these situations the interpreter may have an idea of the expected dip and may therefore assess the angle of emergence.
In the following, we will present how to incorporate this knowledge in the angle of emergence determination. Please note, that the following considerations for the angle of emergence determination are also helpful for the determination of the curvature of the Normal wave, since the parameter is determined on the same input data, i.e., the CMP stacked section.

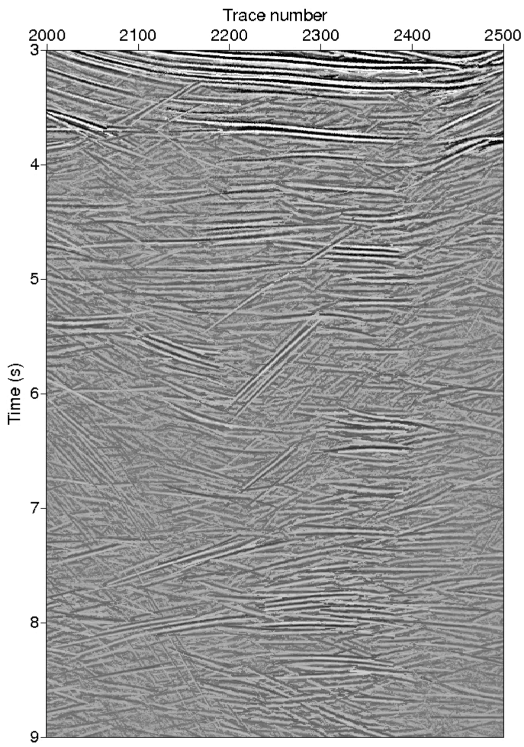

Figure 4: Stacked section from the North German Basin (from Baykulov et al. (2008)). Many unwanted steep dipping coherent noise events occur in the section that hamper geologically reasonable parameter determination.

We now consider the situation, that we approximately know the minimum and maximum time dip α_{min}, α_{max} of the main geological structures in the data. That means we can restrict the grid search intervals for the angle of emergence to $\alpha_{min} \leq \beta_0 \leq \alpha_{max}$. Furthermore, in the current implementation of the CRS stack a guide file can be introduced to the search, similar to the guide file restriction in the CMP search.
Restricting the grid search interval helps to force the estimation of the angle of emergence to the relevant

area of interest. However, in the case of conflicting dip situations, for example where a strong unwanted event crosses a weak wanted event, the angle might be determined at the border of the corresponding search interval, i.e., it clips at the border of the search interval, although it is restricted corresponding to the expected dip of the wanted event. This clipping is an unwanted effect and is caused by the slow decrease of the coherency function of the strong unwanted event. Thus, the correct determination of the parameter for the weak wanted event is nearly impossible in the presence of the strong unwanted event by just restricting the search intervals.

To overcome these limitations, we consider the CMP stacking result again. If the geological situation allows, we are able to modify the CMP stack in the desired sense, i.e., to restrict the dips in the sections and remove the unwanted events, before the actual search is started. Thus, we will examine dip filtering on the CMP stack sections for this purpose.
According to Yilmaz (2001), events that dip in the (t, x) domain can be separated in the (f, k) domain according to their dip. As an initial step in this process a 2D Fourier transformation is applied, transforming the (t, x) space into the (f, k) space. The forward transform reads:

$$F(f,k) = \frac{1}{2\pi}\int_{-\infty}^{\infty}\int_{-\infty}^{\infty} e^{-2\pi i(ft+kx)} f(t,x)dtdx. \tag{24}$$

In the (f, k) domain, the data is decomposed into plane waves, and can therefore be discriminated according to the dip of the corresponding plane wave. Due to this, the data can be manipulated according to the desired dips., i.e. the unwanted dips can be attenuated. This has to be done with a tapered function to avoid unwanted undulations in the (t, x) domain. Afterwards, the stack is transformed back to the (t, x) domain. The backward transform reads:

$$f(t,x) = \frac{1}{2\pi}\int_{-\infty}^{\infty}\int_{-\infty}^{\infty} e^{2\pi i(tf+xk)} F(f,k)dfdk. \tag{25}$$

We now have access to a dip filtered stacked section, where we attenuated unwanted events, e.g., diffractions or steep dipping coherent noise. We use this intermediate result to restrict the subsequent parameter searches to the relevant events. With a proper choice of the filter parameters and the search interval, previously observed clipping effects at the borders of the search interval will not occur. It is important to note, that this will only work properly if the considered events have a significantly different dip than the unwanted events (e.g., diffractions). In many cases these circumstances are fulfilled. Otherwise, the procedure can be applied in certain data areas, e.g., as a windowed application. Furthermore, the determination of the Normal wave curvature will also benefit from the dip filtering, since the parameter estimation is focussed to the relevant events in the section. Please note, that only the CRS attributes are determined in the dip filtered sections. For producing the final ZO section the original data is used.

CRS stack After estimating all necessary parameters (K_{NIP}, K_N, β_0) in the corresponding subsequent searches, equation (15) is considered again and the data is CRS stacked. This can now be done with the geological constrained parameters. The stacking result will probably not reach maximum possible coherency values, but focus on the geological relevant events, as well as any subsequent procedure relying on the CRS stacking result (e.g, poststack time migration).

Optimisation According to the implementations of Mann (2002) and Müller (2007), the previous determined parameters can be further optimised. The optimisation will in most cases not enhance the quality of the stack section, but the determined parameters. This is of great importance when applying subsequent applications based on these CRS attributes. In Mann (2002) the CRS attributes are optimised jointly after their independent determination. A flexible polyhedron search is used (Nelder and Mead, 1965). In contrast to that, Müller (2007) uses a technique based on simulated annealing (Kirkpatrick et al., 1983). Here, the flexible polyhedron search is extended by a so-called continuous optimisation by simulated annealing algorithm (Press et al., 2002). This optimisation procedure can be applied after each initial grid search, i.e., after the CMP or the ZO search, or for the final parameter optimisation all parameter sets are optimised together.

Further considerations In this paper only the implementations important for imaging marine seismic data are considered. To obtain a complete overview of the CRS stack technology many more implementation details have to be taken into account.
For land data, estimations and corrections of residual static shifts can be considered (Koglin, 2005), handling of surface topography can be included (Zhang, 2003; Heilmann et al., 2006), or prestack data enhancement by partial CRS stacks (Baykulov and Gajewski, 2009a) can be used. Furthermore, parameter determination in other acquisition geometries can be applied (Dümmong, 2006). As another aspect the CRS stack technology can be adopted to the processing of vertical seismic profiling (von Steht and Mann, 2008). A further implementation includes the stacking for a desired Common offset plane (Bergler, 2001). In addition to this, the CRS stacking technology does not only produce a high quality stacked section, but also determines the input parameters for several subsequent applications, like a tomography scheme (Duveneck, 2004b), multiple suppression methods (Gamboa et al., 2003; Dümmong and Gajewski, 2008), or minimum aperture determination for time migrations (Spinner and Mann, 2007). All these tools can be used to build an integrated workflow based on CRS attributes, the so-called CRS workflow (Hertweck et al., 2007a).

2.4 Field data example

To illustrate the application of geological constrains in the CRS parameter searches, we will process a subset of an industry data set from the Eastern Mediterranean / Levantine basin. The data covers the so-called Messinian evaporites, which form a strong vertical velocity contrast in the subsurface (bigger than $2000m/s$). The data was recorded using a $7175m$ long streamer. In this application, we use maximum offsets of $3000m$. The CMP spacing is $12.5m$. We will discuss the CRS processing of the data and the subsequent results with special emphasis on the geological constrains introduced into the processing flow as mentioned in the previous sections. For the sake of comparison we will also show processed sections using the conventional parameter searches.

First, we apply the above described stacking velocity constrains (Figure 5(c)) and compare the results with the interval constrained search (Figure 5(a)), a guide file constrained result (Figure 5(b)), and the desired reference result, picked manually (Figure 5(d)). As we can see, the result of the interval constrained search suffers from many parameter fluctuations. These fluctuations are originating for example from multiple reflections present in the data from about $3s$ on. Although the search interval is set to higher values than typical multiple velocities, still stacking velocities at the border of these search intervals are determined and significant lower stacking velocity values than expected are estimated. Also some artefacts are present around $2.5s$, which are corresponding to not reliable determined (i.e., low coherency values) parameters. When a guide file (including a variation of $100m/s$ around the guide velocity) is introduced to limit the search (Figure 5(b)), the stacking velocity field is significantly enhanced and much less fluctuations occur. The influence of the multiple reflections and the artefacts are reduced. To obtain such a result without the knowledge of a guide file would be desirable. In Figure 5(c), we see the result of the dynamic geologically constrained search. We observe, that velocity fluctuations and the influence of the multiples are reduced. The overall impression looks comparable to the result obtained with the guide file constrains. However, we also see some slightly too high estimated velocities from $3s$ on and some artefacts when comparing to Figure 5(b). Nevertheless, the obtained absolute values of the stacking velocities are also represented in the reference result (Figure 5(d)) provided together with the industry data. Therefore, we could obtain a similar stacking velocity field, without using a guide file.

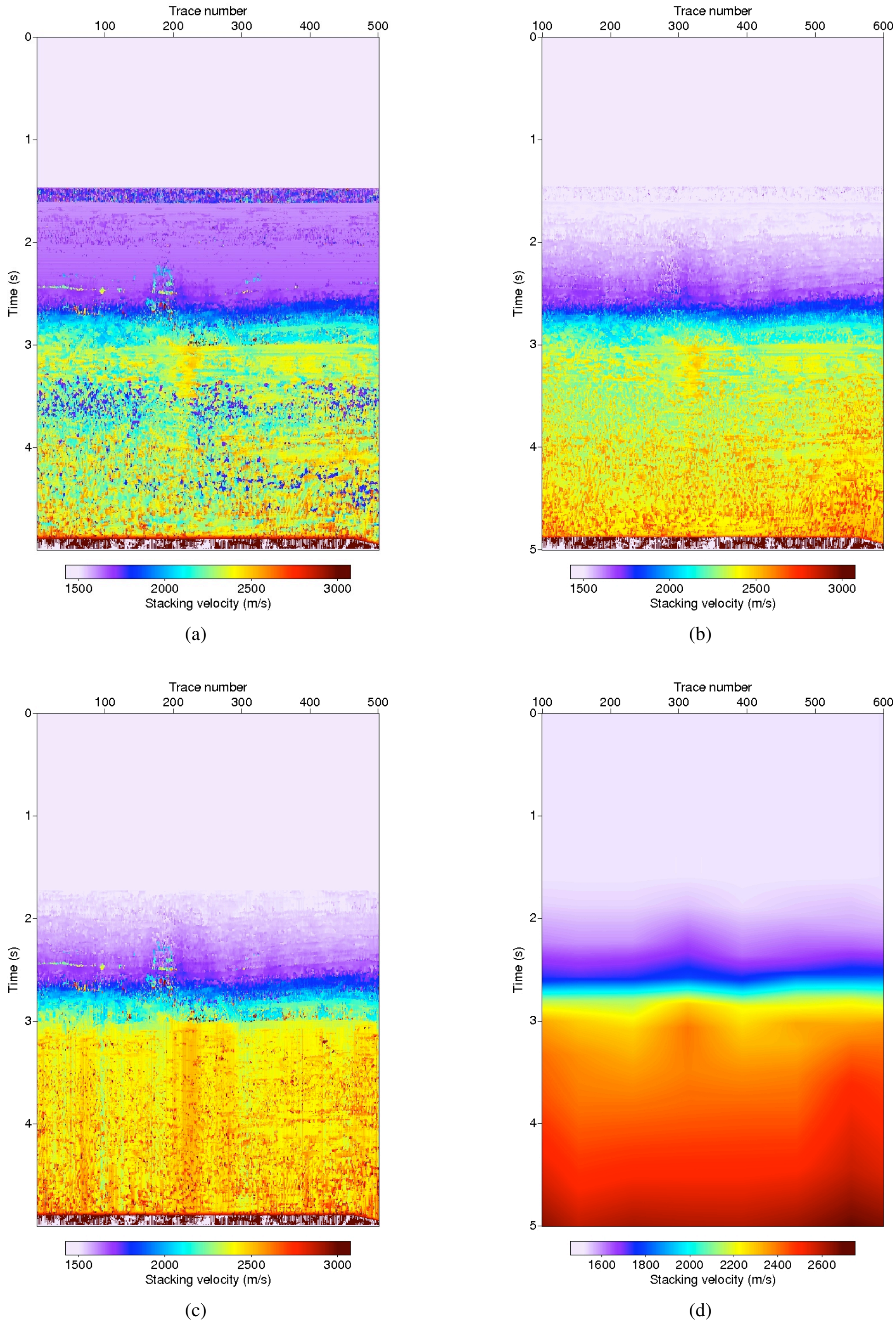

Figure 5: Stacking velocity results from the CMP search. In (a) the search interval constrained result, in (b) the guide file constrained result, in (c) the dynamically geological constrained search, and in (d) the reference result picked manually for the main events in the section (please note the different scale for the image (d)).

Going further in the CRS processing chain, we perform the ZO searches, where we try to introduce geological constrains in the β_0 and R_N searches. For this purpose, we processed the data in the conventional way by restricting the parameter ranges and we also applied the geological constrained approach described above incorporating dip filtering. First, we take a look at some of the stacking results. In Figure 6(a) the CMP stacking result is imaged. In this data set, a lot of diffracting events are present which hamper the ZO parameter estimation of the primaries. Fortunately, the diffractions have a significantly different dip than the reflections, so they can be removed by dip filtering. It is also worth to mention that a lot of unwanted Radon filtering noise, e.g., residuals of multiples, can be removed by the dip filter. The result after application of the dip filter can be seen in Figure 6(b). This section is almost free of unwanted events and will serve as input for the geological constrained ZO parameter estimation. In Figure 6(c) the removed events are imaged. As we can see, a lot of unwanted events were removed.

We now take a look at the ZO parameter sections, i.e., the angle of emergence β_0 and the curvature of the Normal-wave K_N. In Figures 7(a) and 7(b), we see the results of the interval restricted search and the dip filtered search, respectively. As we can see from the comparison of both sections, the proposed search strategy determines less parameter fluctuations and focusses mainly on the reflections. In the result of the interval restricted search, we see some search interval clipping effects (angle values of ± 10 degree), especially in the areas of the steep dipping diffraction events. The search interval was already restricted to ± 10 degrees to focus on the reflections only. Via dip filtering, we could better force the parameter search to the relevant events in the section and thus determine the parameters in a less biased way.

Next, we will take a closer look at the K_N sections that were determined in the second ZO search. For visualisation purposes, we imaged the curvature $K_N = 1/R_N$ instead of the radius R_N. In Figure 7(c), we see the result of the interval restricted search and in Figure 7(d) we see the result of the dip filtered search. In comparison, we hardly see any differences beneath the ocean floor. In the area above the ocean floor, a top mute was applied in the interval restricted search, thus no parameters can be determined there. However, when we take a closer look at the part of the section that was heavily contaminated with multiples (from 3s on), it seems that the result of the dip filtering approach shows slightly less parameter fluctuations. Nevertheless, in general the difference between these two parameter sections is small. One reason, why the difference is small, is the nature of the parameter itself; R_N approximates the curvature of a reflection, which is for this section quite small, regardless of the dip.

After the geological constrained parameter determination, the actual CRS stacking can follow, which will be carried out on the original data, without dip filtering procedures applied. The result will be more focussed on the important events, i.e., reflection events. A parameter extraction for a subsequent procedure e.g., NIP-wave tomography will benefit from the improved parameter determination.

The next step in the CRS workflow would be velocity model building. However, multiple reflections may still be present in the data. Most velocity model building techniques require primary reflection only data sets. In the next chapter, we therefore address two possibilities of attenuating multiple reflections with the help of CRS parameters.

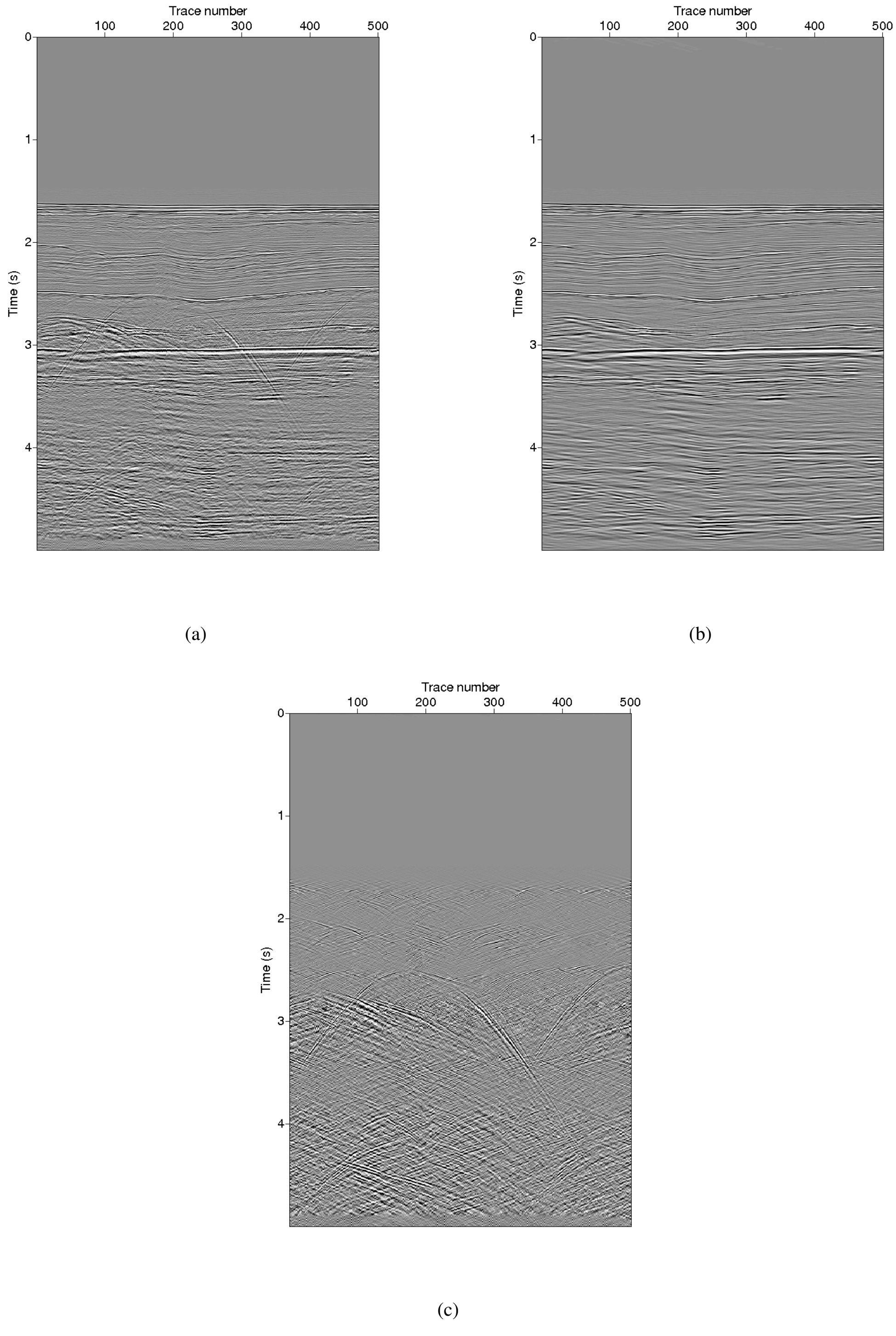

Figure 6: Results of the dip filtering on the CMP stack sections before the ZO parameter optimizations. In (a) the original result of the CMP stack is imaged, in (b) the result after dip filtering, and in (c) the removed events are displayed.

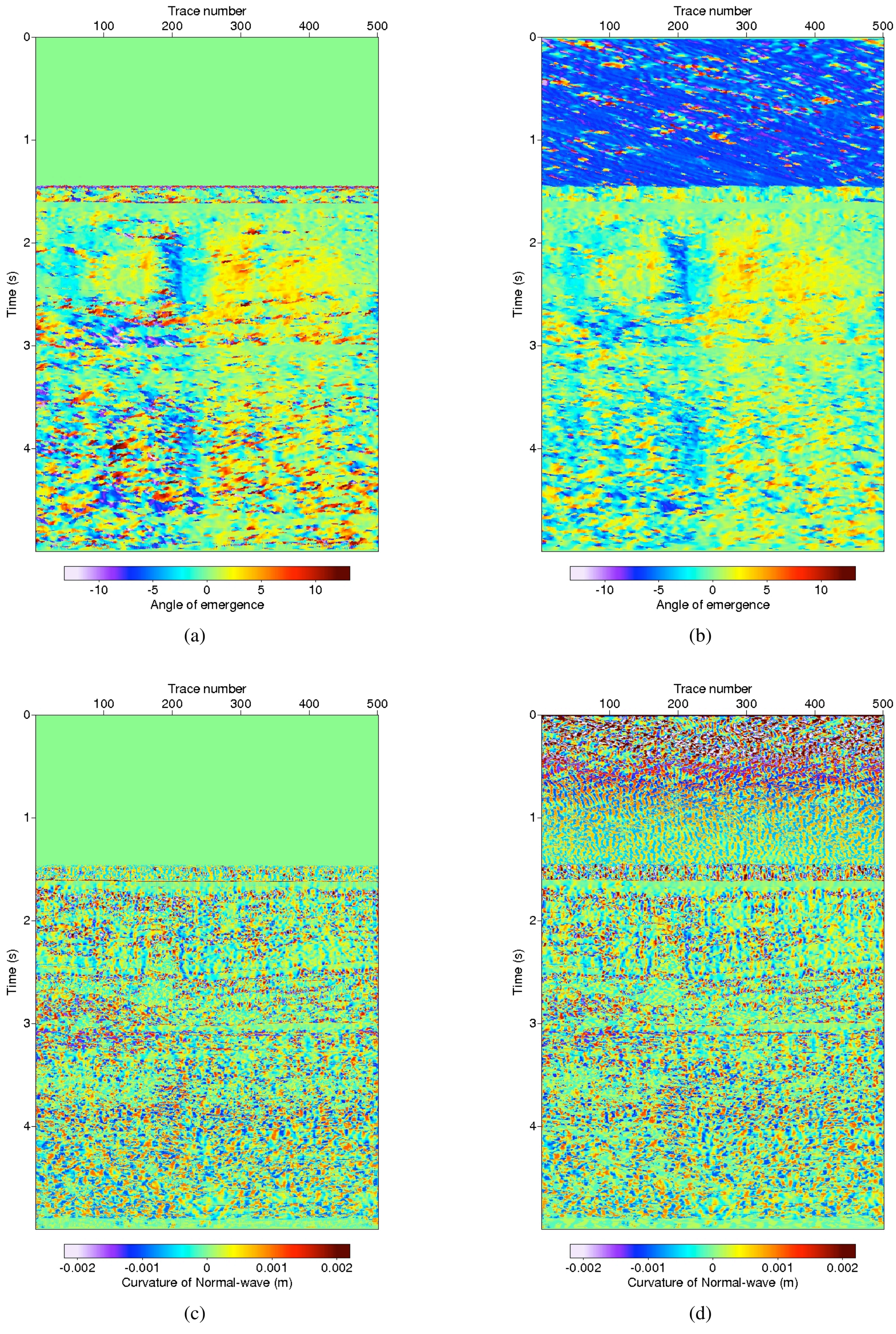

Figure 7: Results of the ZO parameter estimation. In (a) and (b) the angle of emergence determinations without and with dip filtering are imaged, in (c) and (d) the R_N estimations without and with dip filtering are imaged. The fluctuation above the ocean floor reflection in (b) and (d) originate from weak coherent events in the water column, i.e., no top mute was applied.

3 MULTIPLE ATTENUATION WITH CRS ATTRIBUTES

3.1 Introduction

The CRS-workflow (Hertweck et al., 2007a) is a powerful tool for a stable and quick processing chain from time to depth imaging. Currently, it consists of the Common Reflection Surface (CRS) stack (Mann, 2002), the Normal Incidence Point (NIP)-wave tomography (Duveneck, 2004b), and the application of a post- or prestack depth migration algorithm using the NIP-wave tomography model. One of the facts that limit the outcome of this workflow are multiples present in the data. Initial approaches to adress this issue within the CRS-workflow were presented by Gamboa et al. (2003) and Dümmong and Gajewski (2008). The latter one is extended in the first part of this paper.
Some of the most common techniques for multiple suppression are the Surface Related Multiple Elimination (SRME) method of Verschuur et al. (1992), the inverse scattering series of Wegelein et al. (1997), and the hyperbolic radon transform (e.g., Ryo (1982)). For shallow water environments predictive deconvolution (e.g., Peacook and Treitel (1969)) is also widely used. All of these methods have their advantages and disadvantages. None of the methods could be directly included into the CRS-workflow due to additional requirements, like regularization of the data, wavelet knowledge, manual picking, etc. In this study we present two alternative approaches in order to directly incorporate multiple suppression into the CRS-worflow.

The basic idea of the first CRS based surface related multiple attenuation approach is to predict the multiples in the high quality CRS stacked sections, to refine these predictions afterwards, to generate prestack multiple seismograms with the help of CRS attributes, afterwards adaptively filter these seismograms and subtracting them from the original input data. It is important to note, that the prediction of the multiples is not perfect, even after the application of the prediction refinement. In this paper, we rather present an attempt to maximize the fit between the prediction and the actual multiples in the stack.

Additionally, we extended the first approach by no longer considering a 1D approximation in the prediction, i.e. poststack predition. We use partial CRS stacks to regularise our prestack data and perform a multiple prediction directly in the prestack data domain. This approach is similar to the original SRME process, where the wavefield propagation in the subsurface is correctly considered (Verschuur et al., 1992). Here, the CRS attributes are used to prepare the input data for the processing with SRME. Furthermore, we will present an approach of SRME which is independent from the knowledge of the source wavelet.

3.2 Theory

Multiple prediction Multiple prediction by auto-convolution of stacked traces (i.e., poststack SRME) is based on the work of Verschuur et al. (1992) and the ideas presented in Kelamis and Verschuur (1996). The original SRME process is simplified to the 1D case, and is therefore applied to a single trace or stacked data. In the case of the CRS workflow this is the CRS stack section. In this poststack SRME approach, it is simplifying assumed that the stacked data result from plane waves propagating in a locally homogenous medium. This is not fulfilled in the real earth and results in prediction errors. However, when we look at the assumptions made during hyperbolic stacking, i.e., the approximation is only exact for a homogenous medium with one flat reflector, we see that the same assumptions are made. For moderate inhomogeneous media the poststack SRME process can predict multiples quite well (Verschuur, 2006). Nevertheless, the prediction errors have to be addressed to improve the accuracy of the predicted multiples. This is described in the next section.

In contrast to the results presented in Dümmong and Gajewski (2008), which was basically a target oriented approach, the methodology was extended to all surface related multiples by auto-convolving the whole stacked section with itself. Here, no picking is necessary. The basic idea is, that an auto-convolution of a seismic trace $P(t)$ with itself results in a first order surface related multiple prediction $M_1(t)$ (after Verschuur (2006)):

$$M_1(t) = -P(t) * P(t) \tag{26}$$

where $P(t)$ is constructed by $P(t) = s(t) * I(t)$ with $s(t)$ the wavelet and $I(t)$ the impulse response of the earth. Next the first order multiples can serve as a source for the second order multiples:

$$M_2(t) = M_1(t) * P(t) = -P(t) * P(t) * P(t) \tag{27}$$

This can be repeated until n-th order (see Figure 8 for an illustration of the process).

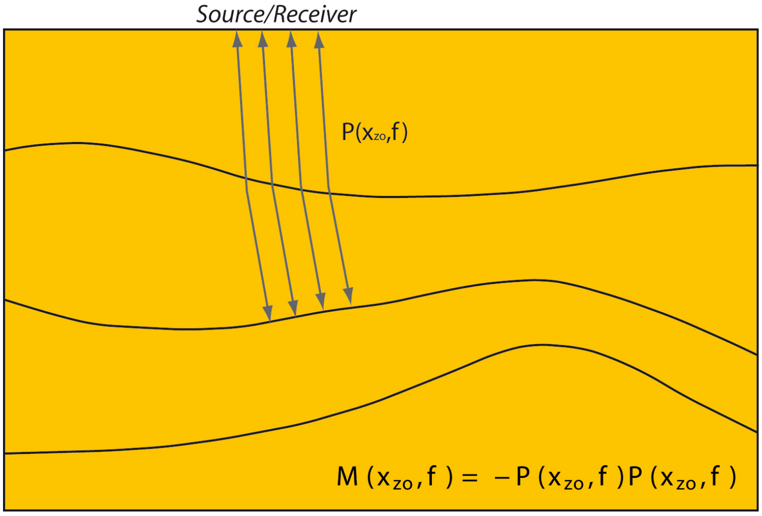

Figure 8: Schematic illustration of the poststack multiple prediction process using auto-convolution.

Since we are using the whole stacked section, we obtain predictions of all surface related multiples at once. However, due to the mentioned 1D approximation prediction errors for large traveltimes and steep dipping events are inherent. Also the wavelet is not considered correctly during the prediction process, which results in errors. In the next section we present an approach for correcting the biased predictions.

Correction term In the search for a correction term for poststack multiple prediction, we employ an image processing algorithm. The problem of correcting the poststack prediction of the multiples is related to finding the best overlap between two similar images. One image comprises the biased multiple prediction. The other image comprises the stacked section, which we processed such that multiples are not attenuated, i.e., we also included low stacking velocities. In this way, we determine the "correct" ZO position of the multiples on the stacked section. The problem is to find the best agreement between these two images, i.e., between the multiple prediction and the original stacked data. For this, we need to determine the shift between the two images in order to obtain the best fit between them. This can be done by a normalized 2D cross-correlation process. Since cross-correlation is a stationary process, it can only find an overall displacement for the whole section, which is not always a suitable idea due to event depended prediction errors. However, the 2D cross-correlation algorithm can also be extended to the case of detecting subimages, which directly leads to a windowed application of the correction term, and therefore an event oriented correction.

Normalized cross correlation algorithms are widely used for different applications, e.g., pattern matching algorithms. Applications include time lapse seismic data imaging (Hale, 2007), cell tracking in nano-biology (Perez-Careta et al., 2008), or fingerprint recognition (Karna et al., 2008).

To algin two 2D seismic images of the same size, one can use a normalised 2D cross correlation (Hale, 2007). The cross correlation of a stacked section and the multiple prediction can be written as

$$CC(\delta_x, \delta_t) = \frac{1}{ntr * nt} * \Big(\sum_{x=0}^{ntr-1} \sum_{t=0}^{nt-1} A_{x,t} * B_{x+\delta_x, t+\delta_t} \Big) \tag{28}$$

where $A_{x,t}$ represents the stacked section, $B_{x,t}$ the multiple prediction, δ_x, δ_t denote the shift in space and time, respectively, ntr the number of traces, and nt the number of samples. In this equation, A and B are normalized by the total number of samples in the data ($ntr * nt$). When this formula is applied, the correlation maximum gives an estimate of the total shift to best align the two sections. The shift is performed in space and time direction. Since this process is stationary, i.e., only a global shift can be estimated, it can only be applied in a limited number of cases, where the geological setting is not too complex and a global shift produces a sufficient correction. The process will be applied more often in a windowed way, which leads to the determination of subimages within a larger image, e.g. localizing a small portion of the multiple prediction on the total stacked section and estimating the shift to apply.

In this case, equation (28) cannot be used directly, because the two seismic sections do not have the same size. Additional steps have to be performed. An intuitive way would be to pad the smaller seismic section with zeros. When doing so, we encountered problems in the estimation of the deviation between the images. The smaller image (i.e., the multiple prediction) were placed in wrong positions. Investigation of this problem revealed, that this happens mainly due to larger mean values in the larger image (i.e., the stacked section). The 2D cross correlation in equation (28) simplified calculates

$$CC = \sum_x \sum_t A_{x,t} * B_{x,t} \tag{29}$$

if $A_{x,t}$ has larger mean values than $B_{x,t}$, these mean values will be represented through out the whole cross correlation function. The determination of the maximum of the cross correlation function, e.g., the shift to apply, then suffers from the more complicated behaviour of the correlation function.

If the two section would have the same mean and variance from the mean, the localization would be successful. Therefore, a modification of the cross correlation function is necessary. We need to balance the two image prior to the 2D cross correlation process in such a way, that we normalise the images by their standard deviation. Assuming that x_1 and t_1 are the samples in the larger section, x_2 and t_2 are the corresponding samples in the smaller multiple prediction, and ntr_1, nt_1, ntr_2, and nt_2 are the corresponding number of traces and samples, one can reformulate:

$$CC(\epsilon_x + \delta_x, \epsilon_t + \delta_t) = \frac{1}{\sigma_{\dot{A}} * \sigma_{\dot{B}}} * \sum_{x=0}^{ntr_2-1} \sum_{t=0}^{nt_2-1} \Big(\dot{A} - \bar{A}\Big) * \Big(\dot{B} - \bar{B}\Big) \tag{30}$$

where $\dot{A}$ is the considered part of the larger image at position $x+\epsilon_x$,$t+\epsilon_t$ and $\dot{B}$ is the subimage at position $x+\epsilon_x$,$t+\epsilon_t$ including the shift δ_x, δ_t,

$$\dot{A} = A_{x+\epsilon_x, t+\epsilon_t} \tag{31}$$

$$\dot{B} = B_{x+\epsilon_x+\delta_x, t+\epsilon_t+\delta_t} \tag{32}$$

Equation (30) was modified in several places (compare to equation (28)). $\bar{A}$ and $\bar{B}$ denote the mean of the stack and the multiple prediction, whereas $\sigma_{\dot{A}}$ and $\sigma_{\dot{B}}$ represent the standard deviations.

The two major differences between equations (28) and (30) are discussed in the following and suggestions for an effective implementation are given. First, the summation in equation (30) is not performed over the entire stacked section. This is not very efficient in terms of implementation. Instead we set all areas outside the smaller image to zero, in order to always sum over all samples. Second, in equation (30) we have to subtract the mean of the sections and normalize them by the standart deviation. This requires additional preprocessing steps. When we combine these two steps, we obtain a similar equation to equation (28) for the preprocessed images.

The normalization of the stacked image can be achieved by a lowpass smoothing filter to construct the mean, subtract it from the stacked section, and afterwards normalize it by the standart deviation. The normalisation preprocessing of the portion of the predicted multiples is slightly more complicated, due to the lack of information outside the actual prediction. Because of this, the calculation of the mean and the standart deviation results in numerical errors, i.e., large values at the borders between the actual prediction and the zero padded areas outside the prediction. Therefore, the length of the smoothing filter has to adjusted to balance the values at the borders of the smaller image. Here, we divided the number of samples of the prediction by two, to have significant contributions also at the edges of the smaller multiple prediction section.

After the correction of the multiple prediction in a windowed way, gaps in the predictions can occur, due to differential shifts of different portions of the multiple prediction. To use the corrected prediction in the subsequent steps, we have to interpolate between the corrected subimages, this can be done according to Hale (2007) or with simple sinc interpolation if the corrected predictions are sufficiently close together. Using overlapping windows in time and space also leads to a solution of the described problem and is mostly used in this work.

After obtaining a corrected multiple prediction, it can be used in the next step, to generate prestack seismograms, adaptive filtering of these seismograms, and finally to subtract them from the original data. These last two steps will be called adaptive subtraction in the following.

Adaptive subtraction and data reconstruction To perform adaptive subtraction prestack seismograms have to be generated. For this purpose, the CRS attributes of the corresponding multiples have to be reliably estimated. Since in the automatic determination of the CRS attributes outliers and erroneous parameter determination can occur, manual picking or a good constraint parameter search for the multiple parameters have be to performed. Additionally, small fluctuations of CRS attributes especially at the temporal or spatial borders of an event can occur. These should be reduced by event consistent smoothing (Hertweck et al., 2005) before prestack data generation.
We then use the CRS attributes to generate multiple pre-stack seismograms. The CRS attributes of the multiples are known, because we determined the correct position of the multiples on the stack and therefore also the corresponding stacking parameters. Since any adaptive subtraction process heavily relies on the accuracy of the prediction, we include the stacked wavelet in the generation of the seismograms to get closer to the actual waveform of the multiple. The multiples are generated in terms of the second order hyperbolic approximation, and thus the original data need to be muted to fit this approximation during the subtraction process. Mann (2002) proposed an offset to target ratio of approximately $1:1$. During the data generation, the multiple data set is separated in three different parts. One part where the multiples reached high coherency values in the stacked section (i.e., reliable CRS attributes), one where they reached intermediate coherency values, and one where the parameter optimisation reached low coherency values. This separation helps to constrain the adaptive subtraction process.

For adaptively subtracting the multiples a Wiener Optimum filter, e.g.,Yilmaz (2001), is used. The Wiener Optimum filter can be described as a filter f_t that is determined in order to best match the input x_t to the desired output z_t. This can be formulated in the following way (see e.g., Müller (2001)):

$$y_t = \sum_{\tau=0}^{m} f_\tau x_{t-\tau} \rightarrow z_t \tag{33}$$

where m determines the filter length. We can now formulate an expression for the energy S and the following optimisation equation can be formulated:

$$S = \sum_{t=0}^{q} (y_t - z_t)^2 = \sum_{t=0}^{q} \Big(\sum_{\tau=0}^{m} f_\tau x_{t-\tau} - z_t \Big)^2 \rightarrow Min \tag{34}$$

where $z(t)$ represents the original data, f_t the Wiener filter coefficients, and $x(t)$ the multiple prediction. q is determined by the maximum number of samples to consider in the matching process, i.e., the trace length. S is the error energy which is to be minimised in a least square sense.

The adaptive filter algorithm is used CMP wise in an application with moving windows in time and space to achieve the best fit with the original data. First well fitted multiples are subtracted with a mild filter (i.e., short filter length, typical $0.04s - 0.08s$), then intermediate fitted multiples with a more aggressive filter (i.e., long filter length, typical greater than $0.08s$) and finally the rest of the multiples with a very aggressive filter.
However, also for multiples with high coherency values residual errors may be present in the result. As mentioned before, the 2D cross correlation process is a stationary process and thus only a total shift for the prediction can be found. Therefore, even in the windowed application of this approach, prediction errors are present after applying the correction term. This sometimes leads to filter artefacts in the data, where primary energy is also removed.

Using partial CRS stacks for prestack gather enhancement (Baykulov and Gajewski, 2009b) these filter artefacts can be significantly reduced. Initially, this procedure was implemented to enhance low fold data and interpolate missing shots. The partial CRS stack technology (Baykulov and Gajewski, 2009b) computes a stacking surface around a specified point defined by its offset and traveltime in a chosen CMP location, and performs the summation of data along that surface. The result of this summation is assigned to a sample within the same CMP at the certain offset and time in the vicinity of the original point. Repeating this procedure for all desired points, generates a partially stacked CRS supergather. The partial CRS stacking surface is defined by the zero-offset time of the considered offset point and the corresponding CRS attributes estimated during an initial CRS stack on the multiple attenuated data. Additionally, the stacking surface is restricted by its extension, i.e. the so-called apertures. To ensure local stacking, these apertures have to be chosen quite small. Since any offset may be considered, a trace regularization can be achieved within the considered CMP. Moreover, partial stacking increases the S/N ratio of prestack seismograms by destructive summation of incoherent noise and thus also has the ability to heal amplitudes affected by filtering artefcats by summing their coherent energy together.
To apply this procedure, we have to determine CRS attributes for the primary reflections in the data. Therefore, the data after multiple removal is analyzed for the CRS attributes. Since multiples are already attenuated, the stacking parameters can be determined quite reliable. Afterwards, we apply the partial CRS stacks to improve the prestack data quality and reduce the filtering artefacts from the adaptive subtraction of the multiples. After the application of partial CRS stack technique, the resulting CMP stacked section shows less filtering artefacts than the conventional CMP stack.

In the following, the implementation of the described methodology and the integration of it into the existing CRS workflow (Hertweck et al., 2007a) will be described in detail.

3.3 Integration into the CRS workflow

The described approach for multiple attenuation is displayed schematically in Figure 9. It can be handled as an extra item in the CRS workflow, before the depth imaging part. The multiple attenuation approach can be summarised and applied as follows:
First, a CRS stack is generated with special emphasis on stacking the surface related multiple reflections to obtain reliable CRS attributes for them. Therefore, the stacking velocity intervals are focussed on lower velocities then one would usually do. Afterwards, the multiples are predicted on the poststack section by auto-convolving each stacked trace with itself. This can be done automatically without user interaction.

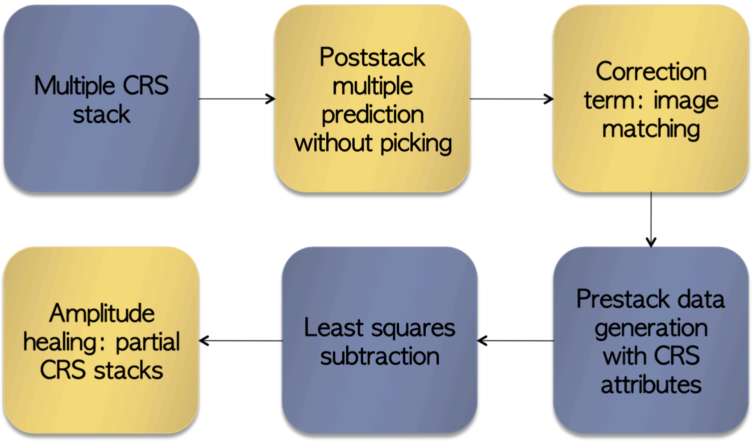

Figure 9: Schematic illustration of the CRS based multiple suppression approach.

In the next step, the correction process is applied. Here, the prediction is best matched to the stacked section, resulting from the first step. Depending on the prediction erros, the process is applied in a windowed way (local comparison) or as a general shift (global comparison) for all multiples. In the current implementation only even numbers for the number of samples and traces are allowed, due restrictions of the underlying Fast-Fourier-Transformation algorithms. The data has to be windowed correspondingly. To avoid edge effects at the borders of the sections, e.g., when shifting the prediction, zero traces should be added to both sides of the sections.

Based on the corrected prediction, prestack seismograms of the multiples are generated. This is done by calculating traveltime curves from the corresponding CRS attributes and taking the stacked wavelet into account. To constrain the subsequent adaptive subtraction process, the multiple events are separated in three data sets according to their coherency values. This avoids aggressive application of the adaptive filter in regions with reliably determined multiples. Multiples with low coherency values can be addressed aggressively. Multiples falling below a certain coherency threshold are rejected, this helps to constrain the adaptive subtraction process to the major multiples.

Afterwards, the adaptive subtraction process is applied. Here, every CMP is considered independently with moving windows in time and space.

If the filtering also affected primaries, prestack data enhancement by partial CRS stacks may follow. Here, the CRS parameters can help to reconstruct affected data parts to their original quality. The necessary CRS attributes are estimated after the adaptive multiple subtraction. The resulting stack might be affected by filter artefacts, but the underlying stacking attributes can still be obtained quite reliably. Afterwards, the partial CRS stack technique can reconstruct data without filter artefacts, i.e., heal the affected amplitudes.

It should be mentioned, that for a quick application of the described procedure the generation of a CMP stack is sufficient. For this case, the prestack seismograms are generated by using the estimated stacking velocities. The CMP stack should produce sufficient coherent energy to process all multiples within a second order hyperbolic assumption.

After applying this multiple suppression approach, the depth imaging part of the CRS workflow may follow, i.e., NIP-wave tomography and a corresponding migration algorithm. Here, primary only data sets are mandatory as input, which can be generated by applying this part of the CRS workflow.

3.4 Field data examples

The above described procedure was applied to two marine data sets. In the following, the results from a data set from the Maldives Islands and from the Eastern Mediterranean / Levantine basin will be discussed in more detail. The first data set was acquired using university equipment (i.e., short streamer, dominant frequency about $100Hz$, etc.) and the second one represents a typical marine industry data set (i.e., long streamer, stronger sources, dominant frequency about $30Hz$, etc.).

Maldives Islands data set The Maldives Islands data set was acquired in 2007 by the University of Hamburg and has a short streamer acquisition geometry with maximum offsets of 600m and a CMP spacing of 6.25m. The data was acquired in a shallow water environment. The dominant frequency is about 100Hz. The data was recorded up to two seconds TWT and covers a complex reef system between the islands of the Maldives. The data has a poor offset-depth ratio of 0.3. Sedimentary structures are present, that generate a band of surface related multiple reflections. These can be seen on the stacked section in Figure 10(a). Between 0.9s and 1.4s from CMP 200 to 1400 a band of multiple reflections covers primary reflections.

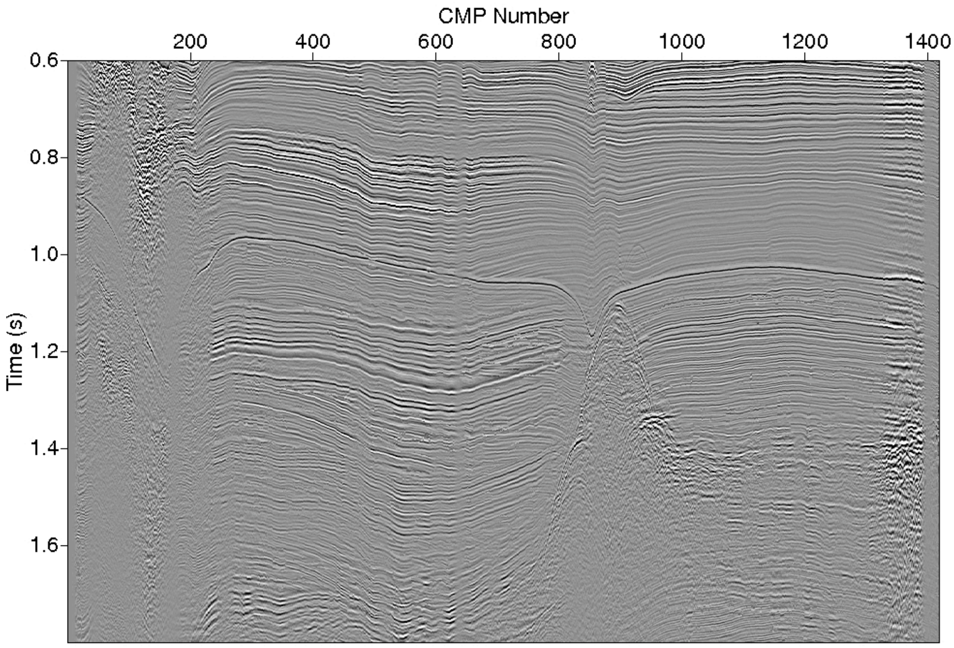

(a)

Figure 10: Stacked section of the Maldives data set. Multiple reflections occur as whole bands and cover primaries mainly in the areas between CMP 200 and 1400 and 0.9s and 1.4s TWT.

After the multiple prediction was generated by poststack auto-convolution, the prediction was corrected by a global shift based on the result of the image matching algorithm. The whole prediction was shifted 2 traces to the left and 13 samples down. The resulting cross correlation function is displayed in Figure 11(a). The difference of the maximum of the correlation function to the zero lag determines the shift to apply.

In this case, the overall shift seems to work quite well. However, to illustrate the ability of the image matching process an application of the windowed application is also presented. Here, we cut a small portion of the multiple prediction comprising 500 traces and 500 samples and try to find the correct position on the stack (local matching). The zero padded portion of the prediction serves as input to the algorithm. At the start the prediction is located at the origin, i.e., position $(0, 0)$ in traces and samples, respectively. After the cross correlation process, the prediction is moved to the correct position (see in Figure 12(a)). The estimated shift is $(999, 1013)$ traces and samples, with respect to the origin.

With the corrected multiple prediction, we can generate prestack seismograms using the CRS attributes of the previously stacked multiples. The wavelets and amplitudes of the stacked sections are used to describe the multiples in the prestack data domain. To start the adaptive subtraction process, the original input data are usually muted according to the hyperbolic approximation. This was not necessary for this data, due to the relatively small offset of 600m. The result of the adaptive subtraction process is then CRS stacked and a multiple attenuated stack is obtained. The stacking result is displayed in Figure 13(a). Especially, in areas around CMP 1200 between 0.9s and 1.4s TWT primary reflection became visible that were previously covered by multiples (compare with Figure 11(a)).

When we look at the prestack data, the subtraction result can also be investigated. In Figure 14(a) the original data is imaged (CMP number 500), in Figure 14(b) the subtraction result and in Figure 14(c) the subtracted multiple energy is displayed. As can be seen on the subtraction result, some residuals are still present in the data. Especially at the position of the ocean bottom multiple (around $1s$ TWT), the least squares subtractions did not completely match the original data.

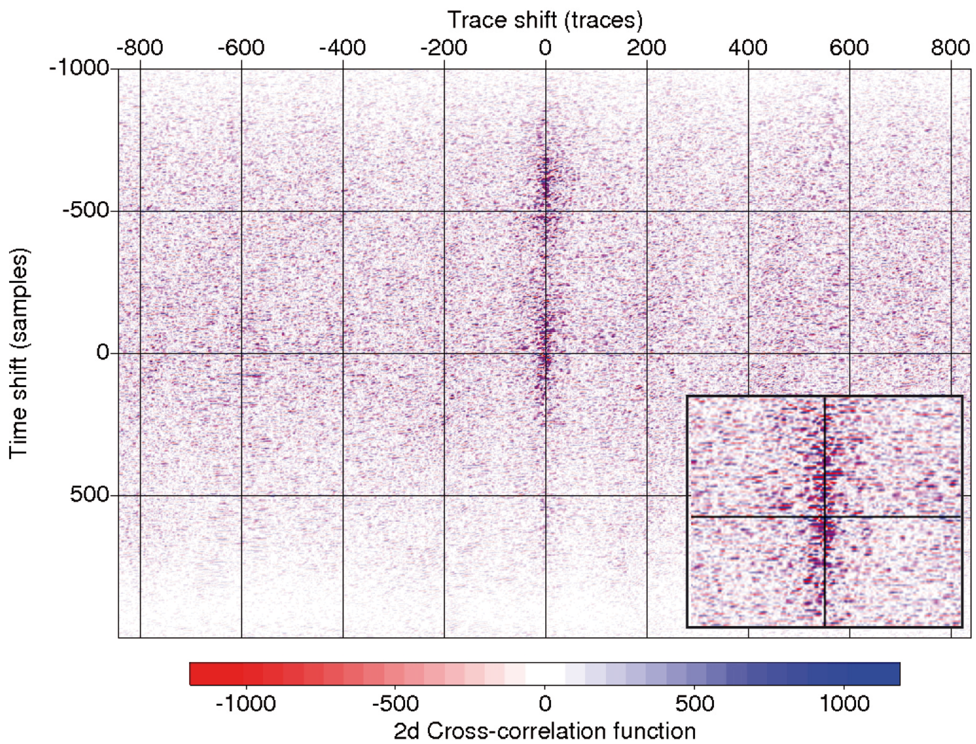

(a)

Figure 11: 2D cross correlation function. The maximum of the cross correlation function predicts a shift of 2 traces to the left and 13 samples in the positive time direction. In the lower right part, the zoomed zero lag of the cross correlation function is displayed.

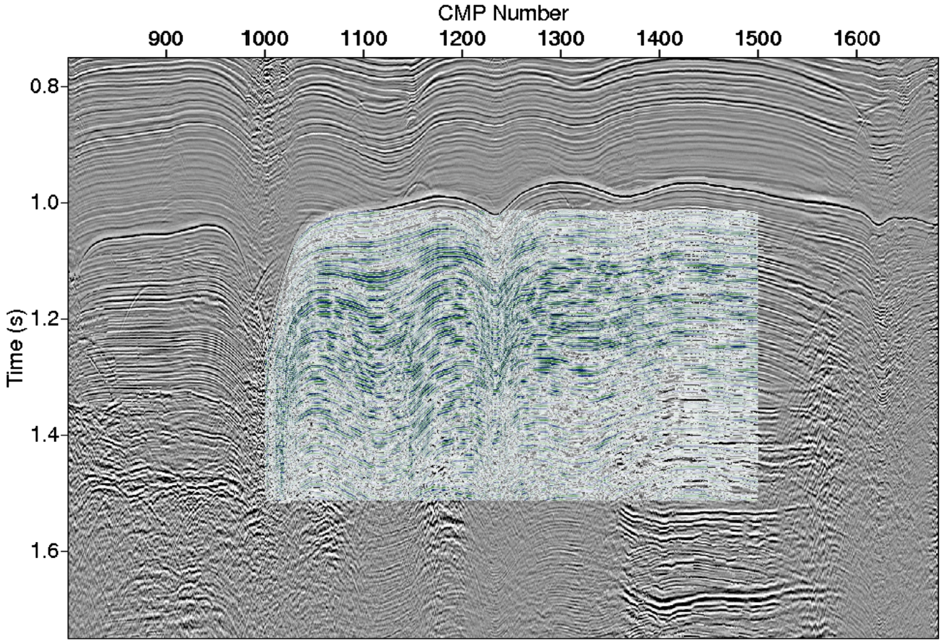

(a)

Figure 12: The original stacked section with multiples (in gray scale) overlaid by the estimated windowed shift of the portion of the predicted multiples (in green and white).

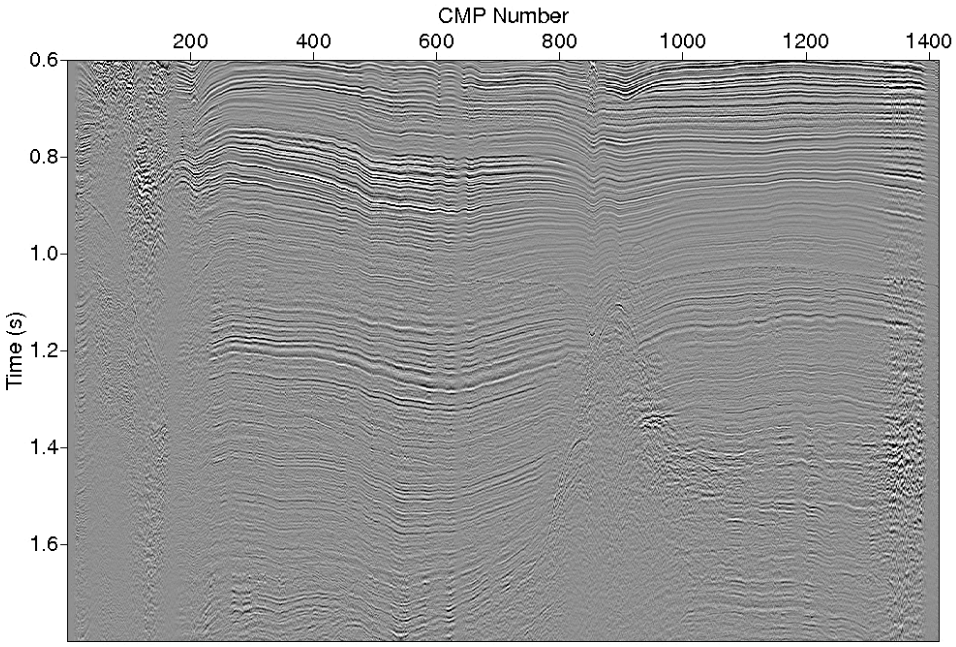

(a)

Figure 13: CRS stacked section of the profile after multiple attenuation. Primary events previously masked become visible.

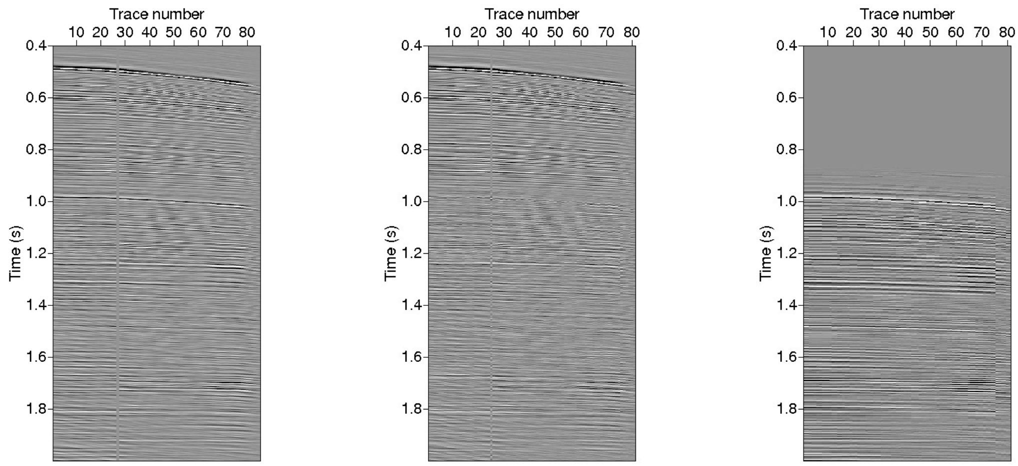

(a) (b) (c)

Figure 14: Prestack result of the adaptive subtraction. In (a) the original data, in (b) the subtraction result and in (c) the subtracted prediction is imaged. Some residuals are still present in (a).

When looking at another line of the data set, in the area around CMP 1400 in Figure 15(a), one can see filter artefacts (i.e., the amplitudes of the primary reflections are distorted). In these areas multiple removal also affected primary reflections. This is a problem especially for short streamer acquisition, where primaries and multiples have almost the same moveout. This feature occurs due to the fact that the stacking velocity of primaries and multiples is quite similar and therefore the moveout discrimination is not significantly large enough. We applied partial CRS stacks to recover the affected primaries. This is displayed in Figure 15(b), where the stack result of the reconstructed data is imaged. The filter artefacts were successfully removed after partial CRS stacking with small apertures to ensure no unnecessary reflection smearing. As an additional effect, the signal to noise ratio in the data is also enhanced.

Eastern Mediterranean data set The data set from the Eastern Mediterranean / Levantine basin is a typical 2D industry data set with maximum offsets of 7325m, a shot spacing of 25m and a receiver spacing of 12.5m. In contrast to the previous data set, the main frequency is about 30Hz and the offset depth ratio is about 0.8 for the deepest targets considered here. For this study, we used 3000m offset and a recording time of 5.0s. The data cover a salt layer, the so-called Messinian evaporites, which form a strong vertical impedance contrast. This contrast and the disturbed overburden are the main multiple generating structures. A large number of surface related multiples are generated from the pre-Messinian sediments and the Messinian salt layer. The multiples from the salt layer almost have the same moveout as the primary reflections underneath the salt body. Additionally, the multiples generated at the top of the evaporite layer are very difficult to process due to strong 3D effects, i.e. multiple reflections originating from off the profile line. These multiples can not be considered correctly in this 2D study. The multiples are masking sub-salt reflections with very weak amplitudes. All these aspects are significant problems, when we try to recover the primary reflections in this data set.

To process the data set, first a stacked section including all multiples was generated (see Figure 16(a)). As indicated before, the salt body and the sediments above generated a set of multiple reflections, that can be seen from 3.25s onward. Here, hardly any primary reflection is visible. The stacked traces were then used to predict the multiples by auto convolution. To better match the original data, the multiple prediction was corrected with the windowed cross correlation approach. In this case, the main shift was determined in the vertical direction, thus the matching was performed by cutting the section into three slices from 0.0s to 3.8s, from 3.5s to 4.5s, and from 4.0s to 5.0s. The overlap was chosen to avoid

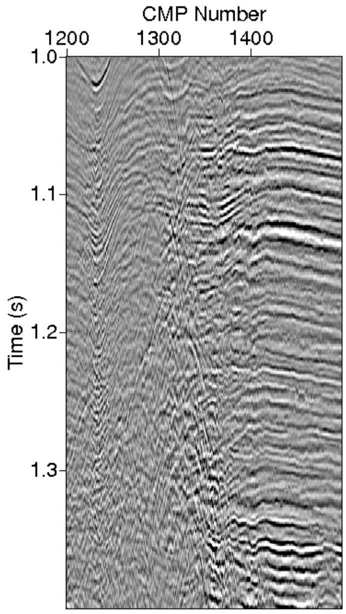

(a)

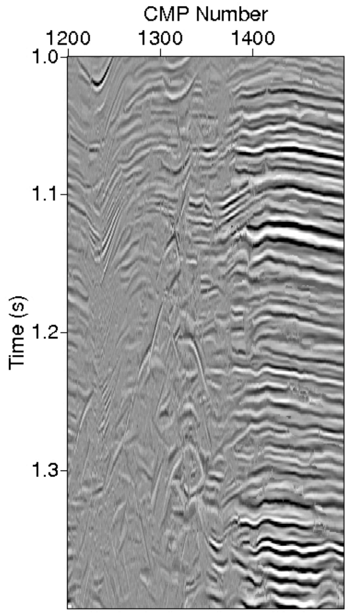

(b)

Figure 15: Comparison between the CRS stacking result of the multiple attenuated data set (a) and after reconstruction using partial CRS stacks (b). Especially between 1.0s and 1.2s filter artefacts could be removed and the quality of the reflections was enhanced.

interpolation, if gaps occur after the correction. The corrected predicition is displayed in Figure 16(b). In comparison to Figure 16(a) the prediction now matches the original stack quite well, i.e., the corresponding ZO positions of the multiples are identified.

In Figure 16(b), an amplitude matching was applied, that the prediction matches the original stack even more. The following generation of the prestack gathers using CRS attributes benefits from this, because the stacked waveform and amplitudes are considered in the next step. The prestack multiple seismograms were separated into three data volumes, separating the data into high coherent (most reliable; semblance values greater than 0.6), intermediate coherent (moderate reliable; semblance values between 0.6 and 0.2), and low coherent (less reliable; semblance values less than 0.2) data. This helps to ensure a mild least square subtraction, i.e., short filter lengths, for the well fitted multiples and aggressive subtraction, i.e., larger filter length, for the less good fitted multiples. The filter length varied from 0.04 to 0.08s.
In Figure 17(a) the stacking result after the multiples attenuation is displayed. We see that a lot of multiple energy was removed and the primaries become visible. However, still a quite high noise level is present in the section and some multiples were not attenuated by this suppression strategy, especially the ones originating from the disturbed top of salt. These areas suffer from wrong parameter estimation, due the fact that no reliable stacking operator was found. This is mainly caused by strong 3D effects, which also hamper the CRS parameter determination. Thus, the multiple reflections could not be described properly and the subtraction is imperfect, leading to residuals.

However, in comparison with the results obtained by standard Radon filtering techniques (Figure 17(b)), the multiple suppression approach based on CRS attributes, produces similar results. The results of Radon filtering where obtained with a commercial processing package as a part of a whole imaging process. Owing to this, the section is overall more balanced in terms of amplitudes and phase conversions

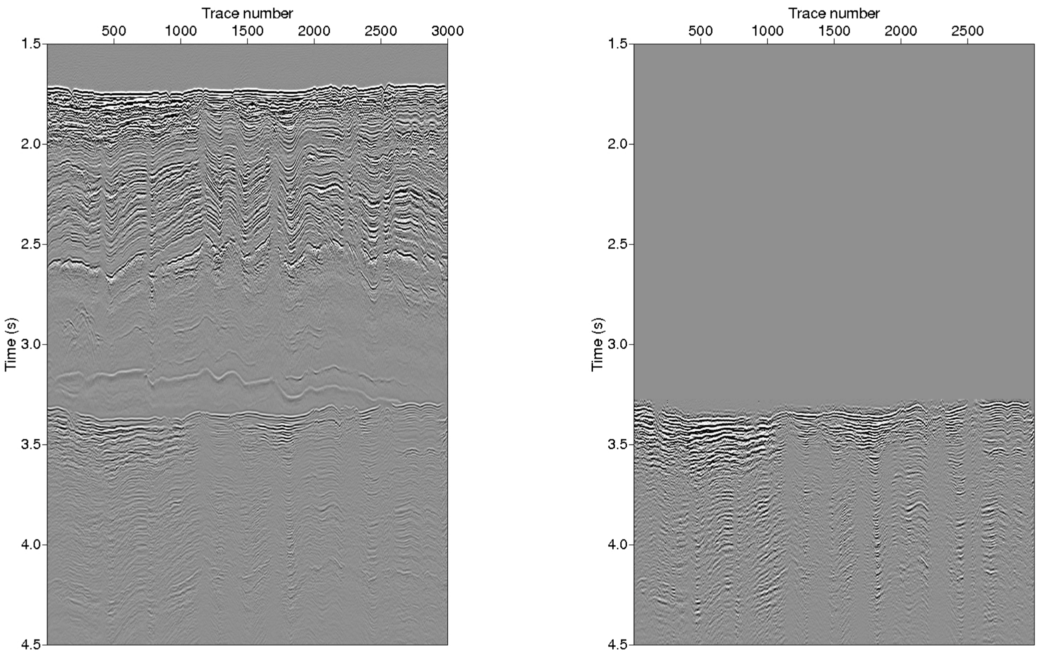

(a) (b)

Figure 16: The stacked section with multiples (a). The multiples appear from 3.25s onward and mask primary reflections. Prediction of the multiples after the correction by windowed image matching (b). The prediction matches the multiples on the stack almost perfectly, besides a different amplitude scaling applied for visualization purposes.

occur, because of deconvolution processes. However, residuals of the multiples occur in almost the same parts of the section as for the result obtained with the presented CRS based approach. Besides that, the data from Radon filtering looks over-processed and lost some of its characteristics, e.g., phases, amplitudes, etc., compared to the original data. Moreover, the ocean floor multiple appears to be more visible. In the end, both approaches do not produce satisfying results, which is probably caused by the fact, that both algorithms rely on the determined stacking parameter. In this geologic situation, the sub salt reflections and the multiples originating from the top of salt almost have the same stacking velocity, which might lead to this result. Additionally, the parameter determination is very challenging, due to strong 3D effects.

When we look at the prestack adaptive subtraction results (Figure 18(a), 18(b), and 18(c)), we see that for both results multiple residuals are present. The CRS approach seems to better attenuate the first order ocean floor multiples, i.e., the multiple with highest coherency values. Radon filtering provides better results in the lower parts of the section, where the CRS stack obtained low coherency values for the events. Therefore, we conclude that the CRS approach can provide good multiple attenuation results, if the CRS parameters describe the multiple reflections sufficiently well.

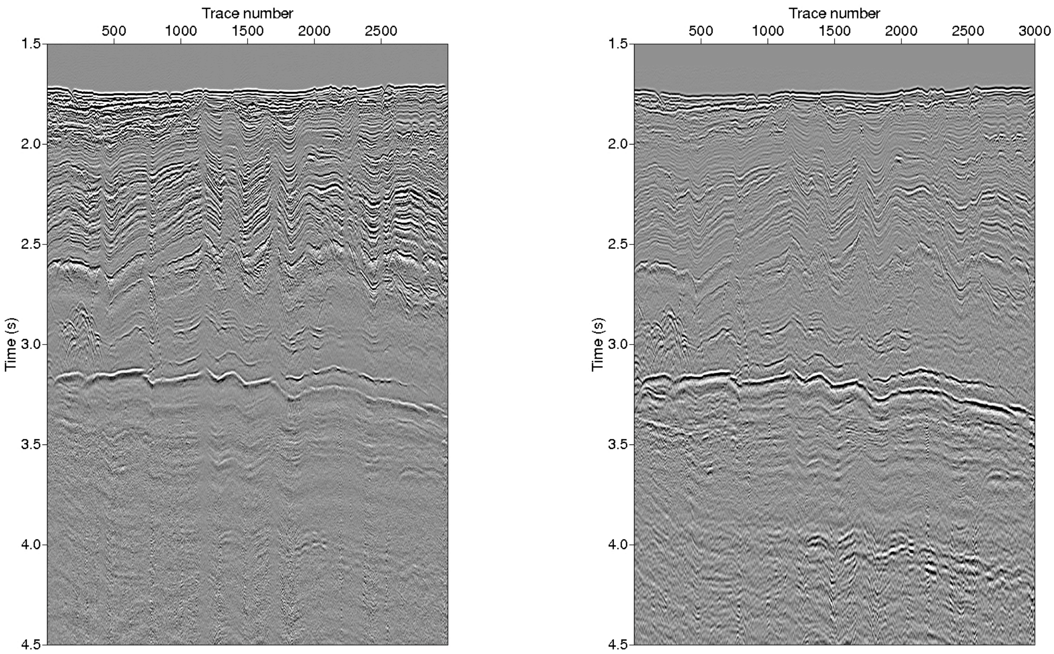

(a) (b)

Figure 17: The stacked section after CRS based multiple removal (a). The multiples that appeared from 3.25s onward were heavily reduced and primary reflections occur. But also residuals as well as filtering artefacts are visible. Stacked section after Radon multiple removal (b). The multiples were also heavily reduced and primary reflections occur, but again residuals as well as filtering artefacts are visible, in some parts more pronounced than for the CRS approach.

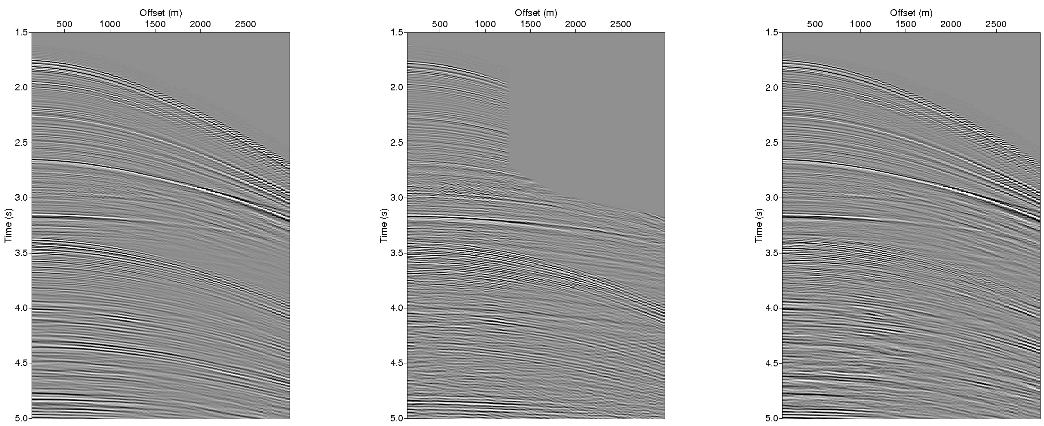

(a) (b) (c)

Figure 18: Comparison between a CMP gather from the original data without multiple attenuation (a) the same CMP gather with Radon filtering applied (b), and the CRS based approach (c). We see that the Radon as well as CRS based left residual multiple energy in the section, but the CRS based approach could better attack the ocean floor multiple than the Radon approach.

This study shows the potential of the method quite clearly. As long as the multiple reflections can be described by a hyperbolic second order approximation and good coherency values can be obtained by the stacking process, the removal will be successful. However, if the description by the CRS attributes is not sufficiently good, the multiple attenuation also suffers. Due to that, the current approach is applicable for moderate complex media, but should be extended to more complex media. For this case, the prediction should consider the wave propagation more correctly in the subsurface, to yield a more accurate multiple prediction.

Such an extension, where we combine CRS parameters and a 2D SRME prediction, is described in the next section.

3.5 Extension of the method

The straight forward extension of the presented multiple suppression approach would be to find a correction term that takes every single multiple reflection independently into account and to find better CRS parameters for the multiple reflections. Unfortunately, this is impossible with pattern recognition based algorithms and the current automatic implementation of the CRS stack. Therefore, substantial changes to the presented algorithm are necessary. This leads to the 2D prediction in the prestack data domain as performed by the 2D SRME method, which is formulated by Verschuur (2006):

$$M_0(x_r, x_s, f) = -\int_{x_k} X_0(x_r, x_k, f) P(x_k, x_s, f) dx_k. \tag{35}$$

In equation (35), M_0 is one considered multiple event, $P(x_k, x_s, f)$ is the total prestack data in the frequency domain specified with respect to the source coordinate x_s, $X_0(x_r, x_k, f)$ is the impulse response of the earth with respect to the receiver coordinate x_r, and x_k is the integration index over all considered lateral coordinates. Note that after the integration only one raypath for one event in X_0 and one event in P is considered (Figure 19(a)). Also note, that for an optimal prediction result, we need an equal fold in shot and receiver gathers including the near offset traces, which is usually not fulfilled for field data. In equation

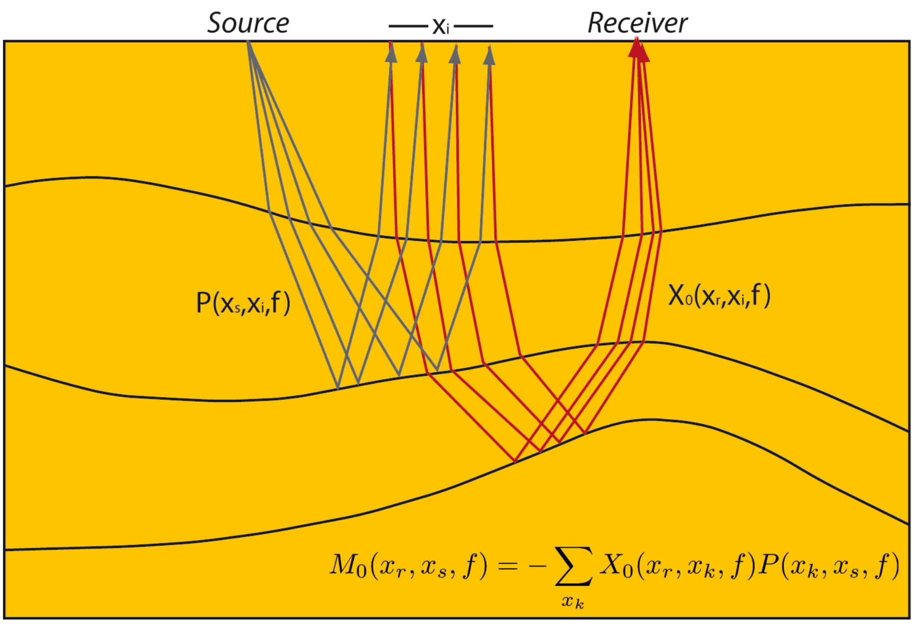

(a)

Figure 19: Schematic illustration of the 2D SRME concept after Verschuur (2006).

(35) the complete ray path of the multiple is constructed and no media approximation is involved as in the

section before. In practice, the integral can be substituted by a summation over all considered locations and the equation can be rewritten as a matrix multiplication:

$$M_0 = -X_0 P \tag{36}$$

Thus, an implicit relation between the multiple free data P_0 and the original field data can be given by

$$P = P_0 + M_0 = P_0 - X_0 P. \tag{37}$$

In equation (35), we considered the impulse response of the earth. If we now connect the wavefield properties $A(f)$, i.e., the source wavelet, with the earth model we obtain

$$P = P_0 + A(f) P_0 P. \tag{38}$$

If we now take the original input data as an initial starting model for the multiple prediction, we can formulate a series expansion for the multiple free data:

$$P_0 = P - A(f)P^2 + A^2(f)P^3 - A^3(f)P^4 + ... \tag{39}$$

Multiple removal now means, performing a trace by trace convolution for every shot and receiver gather in the data, a non linear optimisation process for the source wavelet, and performing a adaptive subtraction from the original data. The requirements of coincident offsets in source and receiver gathers is one of the major drawback of the method as already indicated by Verschuur (2006). A second drawback of the approach is the need of the source signal $A(f)$. $A(f)$ is normally determined by an optimisation process inside every term of the series expansion mentioned above (equation 38). This can be done in a non-linear optimisation process (e.g., Verschuur et al. (1992), Carvalho and Weglein (1994)). Verschuur and Berkhout (1997) proposed an linearised iterative procedure to achieve faster convergence.

We propose to combine the accuracy of the SRME prediction with the ability of the CRS attributes to generate regular data in terms of spatial distribution. Therefore, we use the abilities of the partial CRS stacks to regularise the prestack data (Baykulov and Gajewski, 2009b) and afterwards perform the SRME process for predicting and subtracting the multiples present in the data. In this procedure CRS serves as a pre-process to condition the input data for SRME.
To regularise the data with partial CRS stacks, especially in the near offset range, we add the stacked trace to the prestack data. The stacked trace serves as a zero offset trace and we can interpolate the missing near offset traces by partial CRS stacks. Another benefit of this data regularisation is the enhancement of the data quality in terms of S/N ratio. Since the base of partial CRS stacks are the CRS attributes, they have to be determined reliable for the considered reflections. This can cause problems in areas of conflicting dip situations, where the current implementation of partial CRS stacks only handles one determined dip. The data regularisation approach allows to predicted data for negative offsets, close data gaps, and interpolate shots, which will improve the SRME prediction. All together, the combination of partial CRS stacks and SRME appears to be a valuable tool especially for multiple removal in land data.
Furthermore, we do not consider the source signal $A(f)$ in the SRME prediction. This will obviously lead to prediction errors, but avoids the non-linear optimisation processes. Instead, we take the erroneous multiple prediction from the convolution model and match the multiple prediction to the original data by the image matching process illustrated before. This can be done, as long as the wavelet does not change with offset, i.e., we are not considering overcritical reflections and neglecting small phase shift originating from attenuation effects. With these assumptions, we can consider the prediction error for the multiples as linear and hence a global shift application is valid. This simplifies and restricts the original SRME process from its generality, but saves a non-linear optimisation process and considers the data properly within the CRS approximations. Thus, we perform a cost efficient SRME process, which is applicable within our assumptions. Of course, the data regularisation with partial CRS stacks can also provide regularised data for the original SRME process.
The combined CRS-SRME process in the prestack data domain should overcome the limitations given by the first CRS multiple attenuation approach described earlier in this thesis, since the accurate 2D wave propagation in the subsurface is considered. However, the prediction process in the poststack data domain

is still faster and produces also good results for a wide range of multiple reflections.

The extended approach can be best illustrated by looking at Figures 20(a), 20(b), and 20(c) where we display an irregular shot gather from a synthetic data set including a simulated zero offset trace, the regularised shot gather by partial CRS stack, and the corresponding multiple prediction from the above described approach. As we can see from the images, the prestack data quality is enhanced in terms of S/N ratio, the data is regularised, and no predictions errors occur, since the exact traveltimes of the multiples are predicted. The prediction is performed in a 2D medium and the source wavelet is considered afterwards by the image matching process.

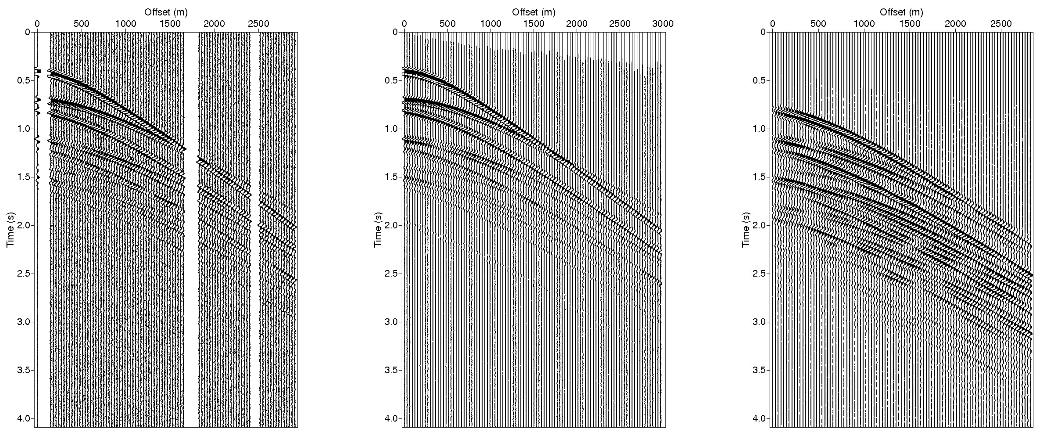

(a) (b) (c)

Figure 20: Comparison between a sparse synthetic shot record (a), a regularised shot record by partial CRS stacks (b), and the first order SRME prediction obtained with the regularised data (c). For a 2D medium no prediction errors occur.

This approach will now be applied to the Eastern Mediterranean data set, where we encountered problems with the first approach in this paper. To test the approach, we decreased the data volume such that we deleted arbitrary traces to generate data gaps. In the next section, we will regularise the data, predict the multiples, and afterwards subtract them in a least squares sense.

Eastern Mediterranean data set We will consider a small portion of the Eastern Mediterranean data set and process about 400 shots, which results in 600 CMP positions. Again, the data is processed up to 5s traveltime. As indicated before, with the help of partial CRS stacks we closed the initial offset gap in the data, interpolated missing traces, and regularised the data to an equal shot and receiver spacing. Thus, we have perfectly suited data for a trace by trace convolution with common shot and common receiver gathers (see Figures 21(a) and 21(b)). Afterwards, we consider the source wavelet and match the prediction to the original shot gather by image matching to perform the multiple attenuation. The result of the prediction for a single shot position shown in Figure 22(b) and the corresponding multiple attenuated shot in Figure 22(c).

In the first image, we see the original gather including a simulated zero offset trace (21(a)). We can observe the missing initial offsets and some abundant traces. On the right hand side of the image, we see the regularised data (21(b)). Both the missing traces as well as the initial offset gap could be interpolated by the data regularisation. With this data we then start the multiple prediction process.

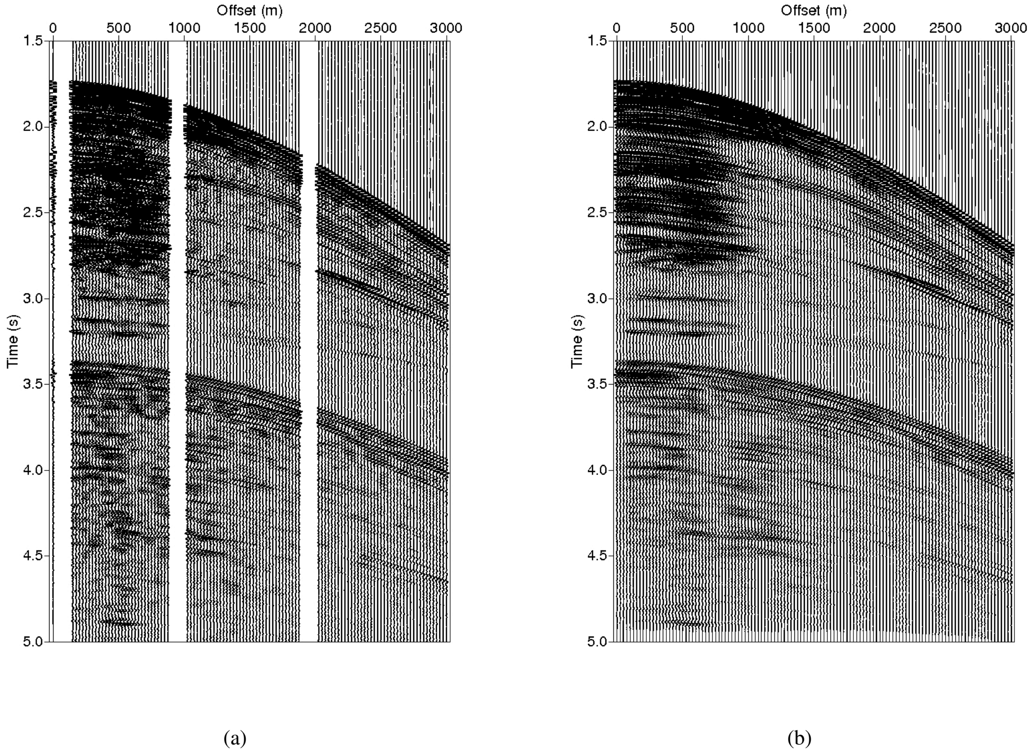

Figure 21: Comparison between a sparse shot record including a simulated zero offset trace (a) from the Eastern Mediterranean data set and a regularised shot record by partial CRS stacks (b). The missing traces could be interpolated and the missing initial offset gap is closed.

In Figure 22(b) we see the result of the simplified SRME prediction. In comparison with Figure 22(a) we see that the multiple prediction fits quite well the multiples in the original field data. In 22(c), we see the result after the adaptive filtering process. A lot more multiple energy was removed from the gather compared to the approach presented before (see Figure 18(c)). Primary reflections are starting to become visible, which were masked by multiples before. The algorithm seems to work better for the medium offset areas (500m to 1500m) than for the near and far offset areas. This might be an effect of the proposed strategy and is in contrast to the general experience, that SRME attenuates multiples particularly well for larger offsets (e.g., Verschuur (2006)). However, some residuals of the multiples are still present in the shot. For most of these reflections the apex has a lateral shift away from zero offset. These reflections are not correctly considered during the previous CRS processing and are thus not correctly considered in the multiple prediction. Nevertheless, in general a satisfying result was obtained. In Figure 23(a) the Radon multiple attenuation result of the corresponding shot section is displayed. Here, residuals are present, especially in the area around the first ocean floor multiple. Primary reflections are hardly visible. Figure 23(b) shows the same shot record with multiple attenuation by the simplified SRME approach applied. To additionally enhance the result and remove unwanted residuals, we applied partial CRS stacks after the adaptive subtraction to reduce filter artefacts and attenuate residuals of the multiple attenuation by a destacking process. We had to determine the CRS attributes of the primaries prior to the application of the partial CRS stacks. Therefore, we muted the near offset traces, where multiples were not distinguishable from primaries in most cases. As can be seen in the shot record, the multiple residuals decreased and more primary reflections become visible. Also the overall noise in the shot record is reduced.

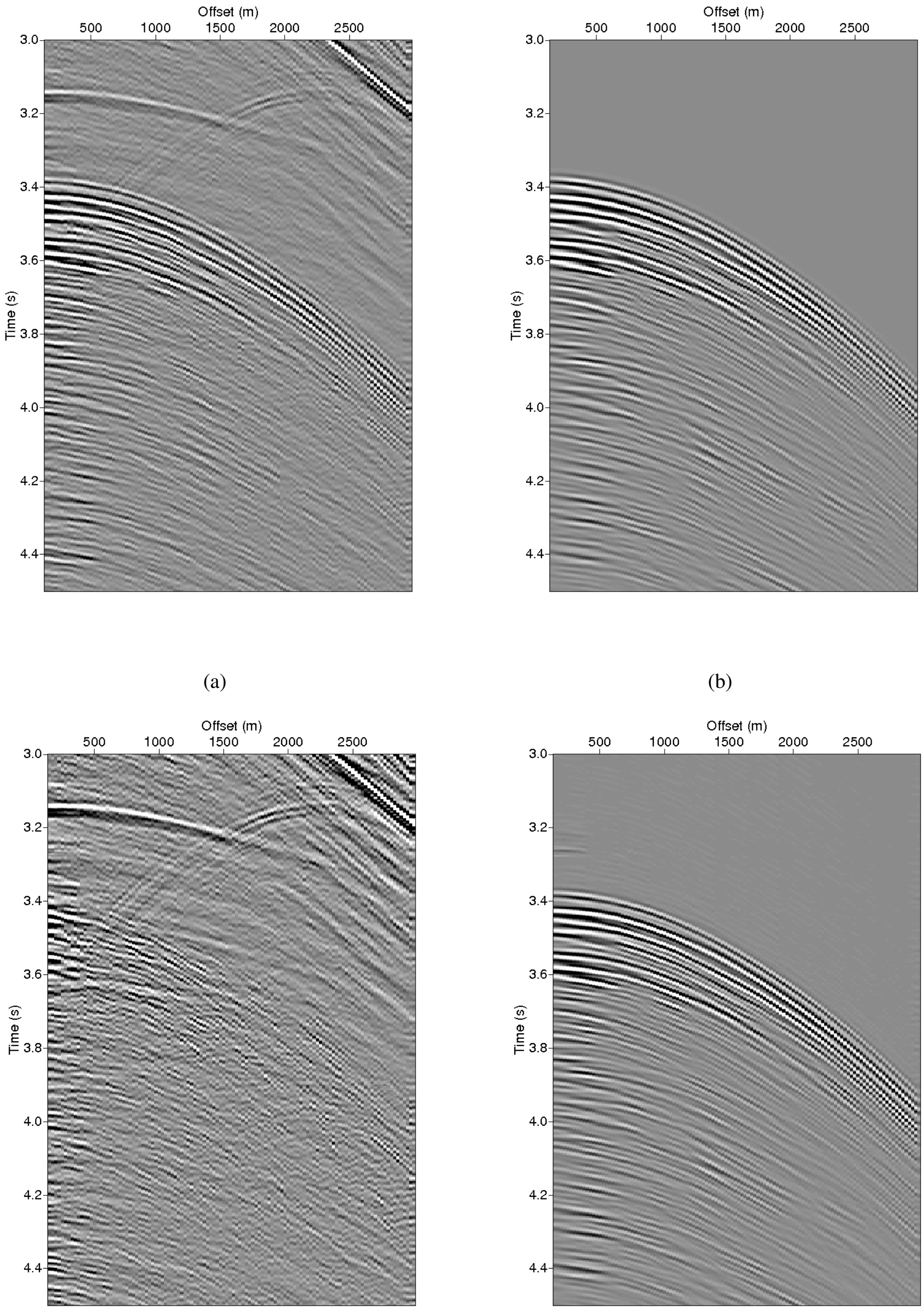

(a) (b)

(c) (d)

Figure 22: Comparison between the original shot record (a) from the Eastern Mediterranean data set, the simplified SRME prediction (b), the corresponding multiple attenuated shot record (c), and the removed multiple energy (d). A lot of multiple energy could be successfully removed from the shot and primaries become visible, but still residuals are present due to small phase shifts in the prediction.

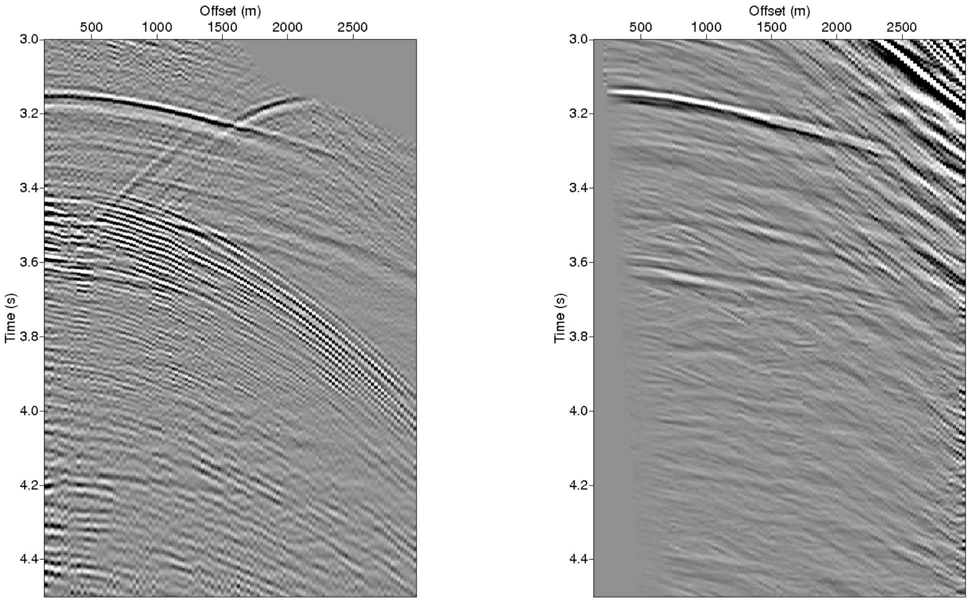

(a) (b)

Figure 23: Comparison between shot records with Radon filtering applied (a) and the multiple attenuation result of the simplified SRME approach, enhanced by partial CRS stacking (b).

In Figure 24(a) the stacked section of the multiple attenuated data is displayed. Most of the multiple reflections are significantly attenuated, but also removal residuals, i.e., steep dipping reflections, starting to occur. The primaries are only weakly visible, also because no further pre-processing was applied. For comparison, Figure 24(b) shows the stacking result without multiple attenuation. Without multiple attenuation, most of the primary reflections are masked and only multiple reflections originating from the structures above are imaged. In Figure 24(c) the result of the Radon filtering is presented. Some residuals for the ocean floor multiple and other multiple events occur from 4s onward. Most primary reflections are visible. Additionally, the section seems more pre-processed (i.e., amplitude balancing, deconvolution), because it is a by product of another imaging workflow applied in a commercial package. The section is overall more balanced and scaled. In Figure 24(d) the stacked section with reduced filtering artefacts using partial CRS stacks is displayed. As we could expect, primaries are further enhanced and filter artefacts are attenuated.

After attenuating multiple reflections in the data, velocity model building may follow as a next step in the CRS workflow. To illustrate the abilities and restrictions of NIP-wave tomography, we will compare it with an alternative tomographic approach, namely prestack stereotomography.

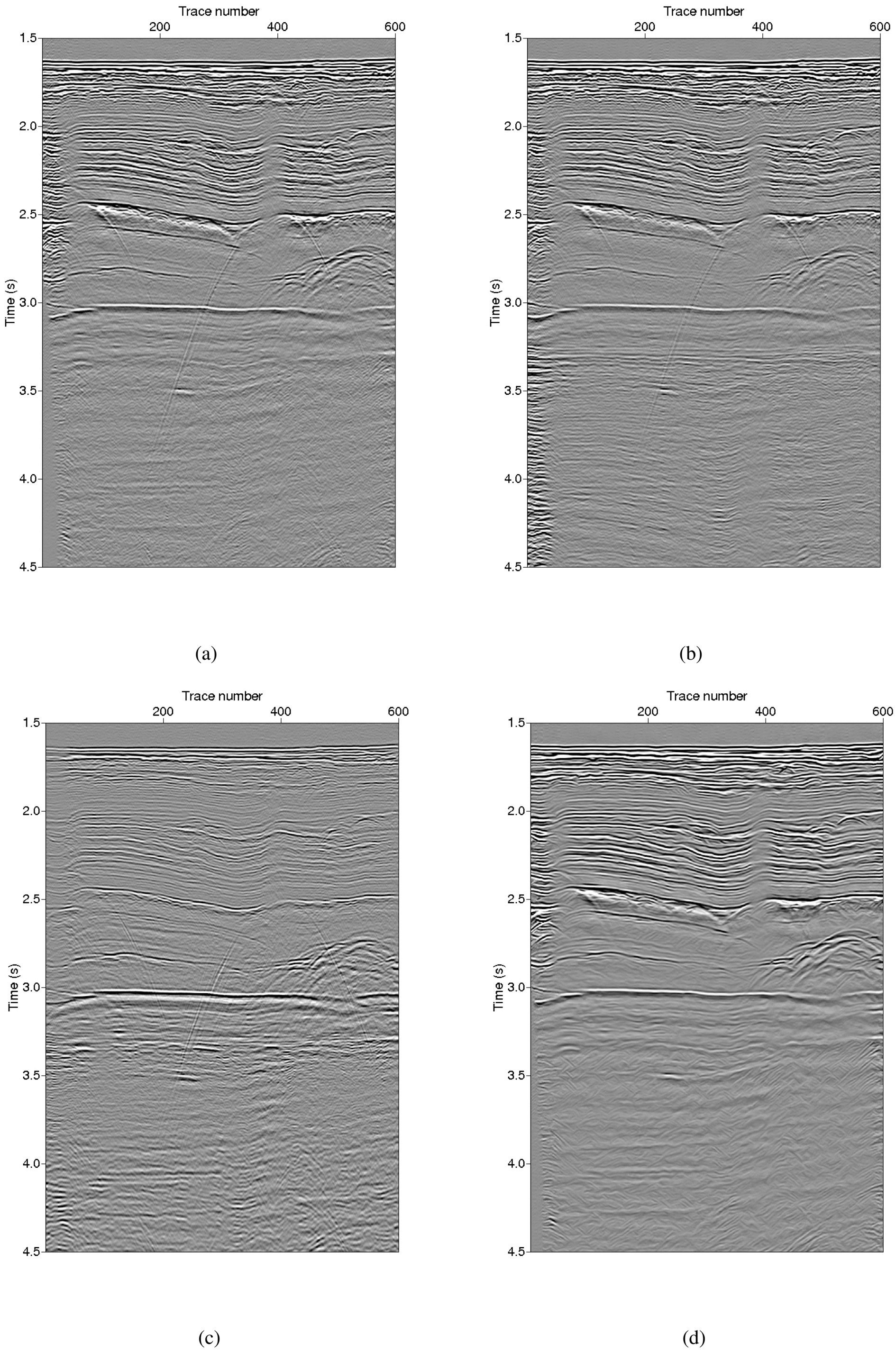

Figure 24: Comparison between stacked sections obtained with the CRS-SRME approach (a), without multiple attenuation (b), with Radon filtering (c), and with further residual suppression by partial CRS stacks (d).

4 COMPARISON OF PRESTACK STEREOTOMOGRAPHY AND NIP-WAVE TOMOGRAPHY FOR VELOCITY MODEL BUILDING: INSTANCES FROM THE MESSINIAN EVAPORITES

4.1 Introduction

For the transformation of the recorded seismic data to the desired depth section, a good migration velocity model is always required. Different approaches for velocity model estimation were proposed in the past. They can be mainly divided into two groups: migration-based methods and pre-migration tomographic methods. Two examples from the second group are NIP-wave tomography by Duveneck (2004c) and prestack stereotomography by Billette and Lambaré (1998).
NIP-wave tomography depends on wavefield attributes resulting from the Common Reflection Surface (CRS) stack (Müller, 1999; Mann, 2002), and is therefore based on a hyperbolic second-order traveltime approximation. The parameters used for velocity model estimation are the second order derivatives of the traveltime (wavefront curvatures), the first order derivatives of the traveltime (slowness), the one-way traveltime, and the lateral positions picked from CRS attribute sections. All parameters refer to NIP rays of a corresponding reflector element in depth. Picking of these attributes is facilitated in the poststack data domain with its higher signal to noise ratio. For NIP-wave tomography, the extracted wavefield parameters do not need to belong to a continuous event.
In stereotomography, reflected events are described by traveltimes and local slopes which are directly linked to the horizontal component of the slowness vector. These slopes, their related traveltimes, and spatial positions at the surface are used for the estimation of a velocity model. All input parameters for stereotomography are estimated for pairs of ray segments referring to the same subsurface element. The input data is obtained in the prestack data domain or in the depth migrated domain (Chauris et al., 2002) by automated picking, but can also be extracted manually. Since only locally coherent events are considered no assumptions on the lateral heterogeneity of the velocity distribution nor the continuity of any interfaces are made. As in NIP-wave tomography, no assumption on the continuity of the reflections are made.
Both methods have been implemented as grid tomographic approaches, therefore leading to a smooth velocity model. Unlike in conventional horizon based schemes no interpretation of events is necessary; however, the vertical resolution of structural boundaries is limited by the grid size and the description of the velocity model. In this article, we compare two implementations of these methods to analyze the impact of the differences in their formulation on velocity model inversion. We have applied both techniques to two sections of a field marine data-set from the Levantine Basin / Eastern Mediterranean. Because of the presence of thick tabular Messinian evaporites strong vertical and lateral velocity contrasts (> 2000 m/s) are expected. The comparison should be drawn with special emphasis on the application of both methods. Theoretical differences are also discussed, but since they also depend on implementationary details, the focus is set on practical issues. The main criteria to assess the obtained results is the flatness of Common Image gathers (CIGs) after a prestack depth migration.

4.2 Theoretical background

4.2.1 NIP-wave tomography NIP-wave tomography (Duveneck, 2004b,c,a) uses the concept of focusing a NIP-wave-front back to its hypothetical source (Hubral and Krey, 1980) which is related to the principle of depth focusing analysis in the determination of migration velocities (MacKay and Abma, 1992).
The NIP-wave is a hypothetical wave which starts at the Normal Incidence Point (NIP) of a reflector in depth and arrives with a certain angle at the corresponding Zero Offset position at the surface. Thus the NIP-waves are linked to certain reflector elements in the subsurface for a given velocity model. All NIP-waves focus at zero time if the velocity model is consistent with the data.

The input data for NIP-wave tomography is obtained from the CRS stack and the accompanying attribute sections (wavefield attributes). The CRS stack is a multiparameter stacking method based on a hyperbolic second-order traveltime approximation in offset and CMP coordinates. The necessary parameters describing the CRS traveltime surface are the wavefield attributes. They are used to estimate a smooth velocity distribution.

Since NIP-wave tomography is based on a second-order approximation of the traveltimes the algorithm is limited to regions with moderate lateral velocity variations. However, the advantage of estimating all parameters in the CRS stacked sections with a higher signal to noise ratio improves the robustness of the attributes and their picking. Therefore, NIP-wave tomography is more likely to be applicable to data with low signal to noise ratio.

The inversion problem for the 2D case can be formulated in the following way: the emerging NIP-wavefront is characterized by four parameters: the traveltime of the normal ray τ, the corresponding coordinate at the surface x, the horizontal slowness component p, and the second spatial derivative of the traveltime M_{NIP}. Consequently, an emerging NIP-wave can be characterized by the data point (τ, p, x, M_{NIP}). The true subsurface locations (X, Z) and the local geological dips α, defining the normal ray take-off direction, are initially unknown. They are determined during the inversion process along with the smooth velocity distribution which is described by B-splines in the fourth order. The velocity distribution is determined in the following way: dynamic ray tracing is performed starting at the considered pick location in depth. The fourth order of B-splines is required, since the Fréchet derivatives of the ray-tracing operator require continuous third derivatives of the velocity field. The subsurface model description is given by (X, Z, v_{ij}), where v_{ij} denotes the B-spline coefficients. By minimizing the misfit between the modeled data and the data points extracted from the CRS stack in a least square sense, the algorithm iteratively determines the velocity model that fits the data best. The inversion problem is solved by a conjugate gradient scheme. Since the minimization of the misfit between the modelled data and the input data is a ill-posed problem, additional constraints have to be introduced to stabilize the inversion. This is done by requiring the velocity model to have minimum second derivatives, this means that NIP-wave tomography estimates the simplest or smoothest model which explains the data.

4.2.2 Prestack stereotomography Prestack stereotomography was proposed, developed, and applied first by Billette and Lambaré (1998). In contrast to conventional tomographic approaches, it uses in addition to traveltimes also slope information to invert the data and is based on the concept of locally coherent events. These are seismic events which can be tracked over a limited number of traces around a central trace in the prestack data domain. In stereotomography, the attributes of these events are used for the estimation of a smooth velocity model.

Seismic events are characterized by the position of their central trace, i.e., their associated source and receiver position (S, R), by their central two-way traveltime T_{SR}, and by their local slopes (p_R, p_S), i.e., the tangents on the traveltime curves at the central trace in a common-shot and a common-receiver-gather, respectively. Since only locally coherent events are considered, each set of parameters (S, R, T_{SR}, p_S, p_R) provides information on the velocity model independently of all other events. Consequently, no assumptions on interfaces nor on the velocity distribution are necessary.
As in all slope tomographic methods (for example Sword (1987)), in addition to traveltime information, the slopes constrain the velocity model as they are directly linked to the horizontal component of the slowness vector. As described in Billette and Lambaré (1998), each event corresponds to a pair of ray segments from a reflection / diffraction point X in the subsurface to either the source or the receiver. Each ray segment is completely defined by its starting and ending point, its angle of emergence or incidence (θ_S, θ_R), and the associated one-way traveltime (T_S, T_R) to the source and receiver, respectively. In the case of a correct velocity model, both segments will satisfy the following boundary conditions: they must join each other, i.e., terminate at the same reflection/diffraction point in depth and they must explain the positions, slopes and two-way traveltimes of the event at the surface.
If the velocity model is incorrect, these conditions cannot be satisfied by both ray segments simultaneously. This means that at least one of the boundary conditions has to be relaxed (become variable). This principle is used by stereotomography: the difference between the parameters describing the relaxed boundary condition and the ideal situation (i.e. a pair of ray segments in the correct model) is used to constrain the velocity model. Based on this, an inverse problem is formulated in which the model space is described by the velocity field and a group of ray segment pairs.

In practice, the boundary conditions at the surface are relaxed and a cost function containing the misfits in source and receiver positions, associated slopes, and traveltimes is evaluated. The data measured at the surface is fitted in a least-squares sense to data modeled by ray-tracing which is performed in a smooth velocity model described by cardinal cubic B-splines. Thus, the model space in stereotomography is composed of a discrete description of the velocity field denoted by the B-spline coefficients v_{ij}, a group of reflecting/diffracting points, two angles of emergence and two one-way traveltimes. These parameters are updated by a joint inversion until they explain each data point (S, R, p_S, p_R, T_{SR}) within prescribed error margins. For the inversion, a conjugate gradient scheme is used. As in NIP-wave tomography the inversion problem is ill-posed and therefore a regularization term has to be added to the cost function. In prestack stereotomography this is done using a Tikhonov regularization. Depending on the magnitude of the associated damping factor this regularization penalizes strong velocity variations and allows to smooth the velocity model without biasing the solution.

4.2.3 Common principles and differences There are two major differences between prestack stereotomography and NIP-wave tomography. First, the input data for the tomographic inversion is obtained in two different data domains. In the prestack stereotomography implementation used here the data is obtained in the prestack data domain, but it can also be obtained in the prestack time or depth migrated domain. The data is represented by spatial positions, two-way traveltimes, and local slopes. In contrast, the input data for NIP-wave tomography is obtained in the poststack data domain. Each data point is described by its spatial position, the normal ray traveltime, and its associated first and second order spatial derivatives. The distinct advantage lies in the fact that the input data for the inversion can be obtained more easily in the poststack data domain with its higher signal to noise ratio.
However, the use of traveltime information in form of spatial derivatives of the underlying hyperbolic traveltime approximation, limits the applicability of NIP-wave tomography to velocity distributions of moderate lateral variation. In prestack stereotomography the traveltimes are described more locally and no such limitations are present. Thus the representation of the traveltimes is the second major difference between both methods.
Further differences are mainly related to implementationary details of both tomographic schemes. They concern the description of the smooth velocity distribution and the regularization of the inverse problem. Due to the above mentioned higher order of B-splines used as well as the inherent regularization of the inverse problem, we assume that the velocity distribution of NIP-wave tomography will be generally smoother than the one of prestack stereotomography.

4.3 Data examples

4.3.1 Geological setting The data set from the central Levantine Basin / Eastern Mediterranean covers a basinal succession or mobile unit (MU) of the Messinian Evaporites, a Pliocene-Quaternary overburden, and the upper pre-Messinian succession (Fig 25(a)). The data is represented by a 2D line, with 25 m shot spacing, 12.5 m receiver spacing, and with a maximum offset of 7325 m. According to the chronostratigraphic scheme of Clauzon et al. (1996) or Krijgsman et al. (1999) the precipitation of the MU started around 5.6 Ma during the Messinian Salinity Crisis (MSC). The end of the MU formation and the rapidity with which the Mediterranean basin was refilled at the end of the MSC - between a few thousand years (Clauzon et al., 1996) and about 200000 years (Krijgsman et al., 1999) - are still a matter of debate. In the following and according to Ryan et al. (1970), the base of the Pliocene-Quaternary succession will be called M-reflection and the base of the MU N-reflection.
Recent publications showed a complex seismic stratigraphy of the MU in the Levantine Basin (Gradmann et al., 2005; Netzeband et al., 2006a; Bertoni and Cartwright, 2006), which can be divided into six sequences (Hübscher et al., 2007; Hübscher and Netzeband, 2007b). Sequences ME-I, II, IV are seismically transparent (see Figure 26(a)) and sequences ME-III and ME-V reveal several internal and subparallel reflections (Hübscher and Netzeband, 2007b). The absence of seismic reflections is typical of salt bodies (Mitchum et al., 1977) and so the internal velocity is expected higher than 4 km/s (Netzeband et al., 2006a). The internal reflections have been interpreted as intercalated (and presumably overpressurized) clastics by Garfunkel et al. (1979) and Gradmann et al. (2005). However, 3D-seismic data analysis proved a high lateral continuity of seismic reflection characters and identified polarity changes which are more indicative

of chemical sedimentation processes (Bertoni and Cartwright, 2007).
The deformation pattern of the intra-evaporitic sequences include folds and thrust faulting, which gives evidence for extensive salt tectonics and shortening, respectively, during the depositional phase. Both, the identified evaporitic facies of the individual intra-evaporitic sequences and the driving forces for the syn-depositional shortening remain unclear. Post-depositional gravity gliding caused salt rollers in the extensional marginal domain, compressional folds, and faults within the Levante basin (Gradmann et al., 2005; Hübscher and Netzeband, 2007b).

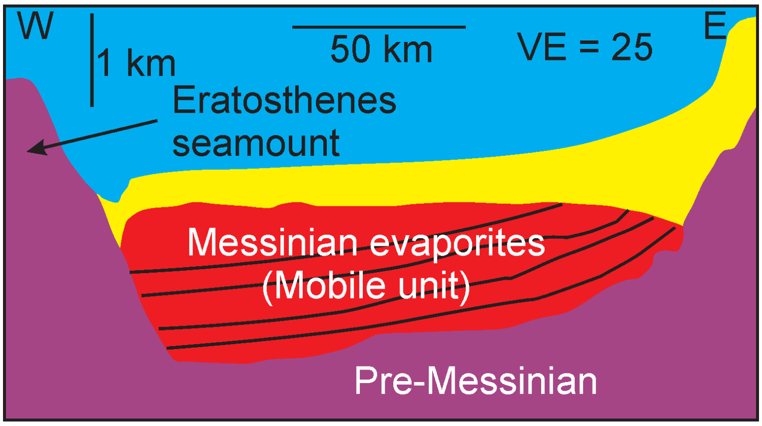

(a)

Figure 25: Linedrawing of a depth migrated seismic section from the Levantine Basin/Eastern Mediterranean (after Hübscher and Netzeband (2007b)). Up to 2km thick Messinian evaporites are covered by a Pliocene-Quaternary succession.

As velocity model building and depth-migration in salt bearing basins is a challenging task this data set represents an excellent test data set for the comparison of both methods. The vertical velocity contrast between the MU and the overburden is bigger than 2 km/s, since interval-velocities of $4.3 - 4.4$ km/s were determined for the evaporites and $1.7 - 2.1$ km/s for the overburden, respectively (Netzeband et al., 2006b). If the MU is folded, strong lateral velocity contrasts occur at their top. Small thickness undulations of the MU cause apparent reflection undulations beneath (velocity pull-ups/-downs), which may be spuriously interpreted as folds or faults. The intra-evaporitic reflections reveal much weaker amplitudes than the top or base of the MU.
In the following we will present a comparison of the two tomographic methods on two data examples. One is a distal section, with quasi horizontal geologic layers, dominated by a strong vertical velocity contrast between the sediments and the salt body and a large fault structure in the salt. We will use this section to compare the vertical resolution of the obtained velocity models. The second data example is a proximal section with a very heterogenous geological setting. Typical salt roller structures occur where the salt body pinches out against the shelf. The strong lateral velocity variations allow the comparison of the lateral resolution of both methods. The comparison should be drawn with special emphasis on the data domain, where the input data for the inversion is generated and the resolution of the obtained velocity model under the same equal initial conditions for the inversion in terms of the preprocessing, the B-spline grid spacing, and the starting model. Common image gathers (CIGs) are used to evaluate the results. They are obtained using a Kirchhoff first arrival approach with a maximum offset of 3500 m. The same prestack depth migration tool is used for both methods.

4.3.2 Distal data example

Description of the section The first data example covers 1000 CMP locations. The associated CRS stack section is displayed in Fig 26(a). Down to 2.7 s two-way traveltime (TWT) the post-messinian sediments can be observed. The MU can be identified between 2.7 s and 3.5 s. The reflection at approximately 2.7 s corresponds to the top of salt reflection (M) and the reflection at 3.5 s to the bottom of salt (N). The internal reflection pattern of the MU can also be recognized. Below the N-reflection the pre-messinian sediments are visible. At an inline distance of 122 km, a large fault structure can be identified, which pierces the sea floor. From the stacked section it remains unclear, whether the fault terminates at the base of the salt or if it continues in depth.

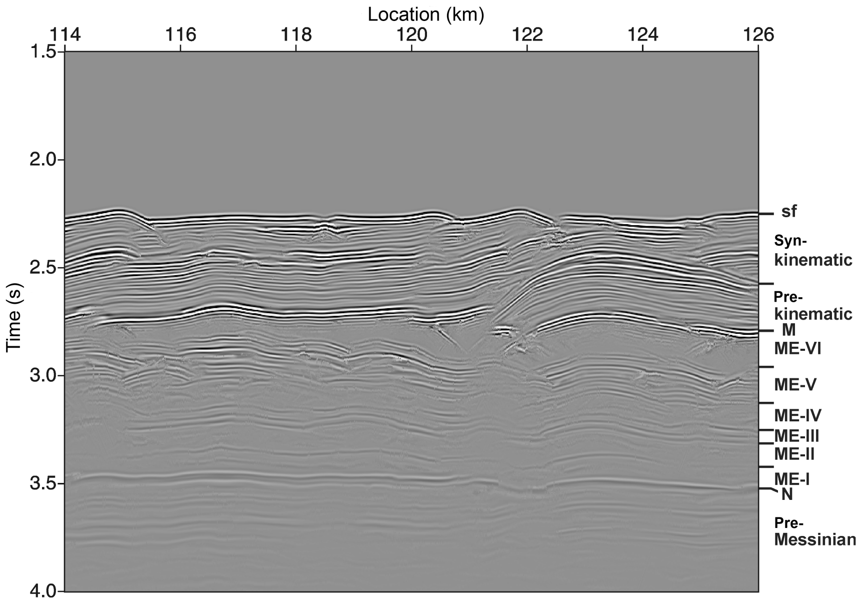

(a)

Figure 26: Distal data example. Between 2.7 s and 3.5 s the mobile unit (MU) of the Messinian evaporites can be identified. The MU reveals six evaporitic sequences (Hübscher et al., 2007). The Pliocene-Quaternary overburden is subdivided into a pre- and synkinematic sequence.

This data example seems to be particularly suitable for investigating the vertical resolution of both tomographic methods. The methods have to deal with a strong velocity contrast between the sediments and the salt body. Furthermore, the potential of the methods to estimate velocities across a large fault structure can be analyzed.

Application of NIP-wave tomography To process the data example (Figure 26(a)) with NIP-wave tomography, we performed multiple suppression via $f - k$ filtering and a CRS stack in order to acquire the necessary kinematic wavefield attributes. The CRS aperture was optimized to obtain reliable wavefield attributes for the automatic picking algorithm which produces the input data of NIP-wave tomography. Furthermore, an event consistent parameter smoothing (Hertweck et al., 2005) was applied to the wavefield attributes in order to remove unphysical fluctuations in the CRS parameters. The automatic picking tool identifies the events in the CRS attribute sections mainly based on semblance criteria. Depending on a pre-defined threshold only the most reliable reflections are picked. After picking, a quality control of the picks followed in order to remove outliers from the data. This quality control was mainly based on stacking velocities computed from picked CRS attributes and followed the practical aspects discussed in Duveneck (2004c).
With the extracted and edited picks we performed NIP-wave tomography. We used an initial velocity model of $v(z) = 1500$ m/s$+0.4$ s^{-1}z. The initial B-spline spacing was set to 125 m vertically and 500 m laterally. This choice was possible due to the fact that NIP-wave tomography works in the poststack data domain, leading to less input data and a quite stable inversion process from the beginning. Nevertheless, the inversion had to be stabilized in the water column and the corresponding B-spline nodes were forced to water velocity by minimizing the misfit to this value. All input parameters were weighted equally during the inversion and after ten joint inversion iterations the cost function reached its minimum.

Figure 27(a) shows the result of NIP-wave tomography. The velocity distribution is displayed together with the locations of the modeled NIPs related to every input event. The position of the seafloor is clearly marked at a depth of 1700 m and a velocity increase to 3000 m/s represents the sedimentary overburden above the top of salt at 2200 m. The subsequent high velocity body, incorporating zones ranging up to 4500 m/s, corresponds to the evaporites. The velocity inversion at a depth of about 3500 m describes the salt-sediment transition. The velocity distribution indicates the geologic structures in the depth migrated image, but the data coverage was not satisfactory in the vicinity of the fault structure (122 km). In this area Figure 26(a) illustrates, weak reflections are present in the CRS stacked section, but they could not be identified by the automated picking algorithm. Since picking could also be performed manually, these reflections could have been selected manually.
The resulting prestack depth migrated image and the corresponding Common Image gathers (CIGs) are displayed in Figures 27(b) and 28(a), respectively. A maximum offset of 3500 m was used for the migration. The quality of the depth migrated image is good, all sediments are imaged well over their entire thickness of 500 m. The M-reflection is imaged at a depth of 2200 m. The salt body shows all internal features and the N-reflection is reasonably flat. The fault structure shows some significant velocity pull-up effects and has to be considered as unreliable, due to the poor illumination by input picks.

Figure 28(a) shows selected CIGs equally spaced over the whole section. All reflections are reasonably flattened. Some residual move-out can be observed in the transitional zone between the sediments and the salt body, were the smooth velocity description could not handle the strong velocity contrast. Nevertheless, NIP-wave tomography produced a velocity model consistent with the input to the inversion. The model thus explains the kinematic information extracted from the seismic data.

Application of prestack stereotomography In order to perform prestack stereotomography some additional preprocessing had to precede the actual tomographic inversion. In the frame of this section the preprocessing consisted again in multiple suppression via *f-k* filtering, but also in a t^3-gain control to ensure the amplification of later events, and in applying a so-called stereotomographic mute to focus the automatic input data selection on the most relevant traces (see Lambaré et al. (2004) for more details).

After preprocessing, semblance was estimated every 50 m using 8 traces for local slant stack calculation. The initial thresholds for a pick to be accepted were set to a minimum semblance of 0.6 in each common-shot and common-receiver gather, respectively, and events with an energy less than -40 dB from the highest energy observed for the current central trace were skipped.
After application of the automatic picking algorithm (Billette et al., 2003), we applied a first quality control sequence for the input picks consisting of an interactive selection of picks. Due to strong differences of energy in the data (i.e. differing reflection amplitudes from the sediments and the salt) the input data was split into three parts. The subdivision of picks depended on different traveltimes and energy thresholds. The first subset mainly consisted of picks from the sediments, the second one of picks from the sediments and the upper parts of the MU body, and the third one mainly of picks from the MU. To further remove outliers in the data, each data subset was inverted separately and a second quality control sequence based on global normalized misfit was carried out. During this step all picks with a global normalized misfit bigger than a certain threshold were rejected from the inversion after a reasonable number of iterations. The first two data subsets were inverted using a constant staring model of $v(z) = 1500$ m/s and the third one was inverted with a starting model of $v(z) = 1500$ m/s$+0.4$ s^{-1}z. For each input data set we performed 10 localization steps, where only the pairs of ray segments are optimized keeping the velocity model fixed to its initial value. Afterwards a different number of joint inversion steps followed. Due to the energy decrease in the data and increasing complexity different error thresholds and regularizations were used for this quality control.

After this quality control sequence, the remaining subsets of picks were merged and the inversion procedure was restarted with the resulting input data set. This time an initial velocity function of $v(z) = 1500$ m/s$+0.4$ s^{-1}z was used and an initial B-spline grid of 500 m x 500 m was chosen. To additionally stabilize the inversion artificial picks in the water column were added to the input data. After

10 localization steps, we performed 10 joint inversion steps with a strong regularization after which a significant decrease of the cost function could already be observed. In order to increase the vertical resolution of the model we reduced the node spacing to 125 m in depth. A subsequent step consisting in 20 joint inversions and a loose regularization followed. However, velocity model estimation was stopped after 17 iterations since no further decrease of the cost function was noted, so in total 27 joint inversion iterations were performed.
Figure 29(a) shows the result of prestack stereotomography. The depth converted input picks for the inversion are overlaid with the velocity distribution in form of short bars indicating the local geological dip. The high velocity area refers to the MU (starting at a depth of 2250 m). The strong gradient from 1550 m/s to 3000 m/s on top of the MU represents the post-messinian sediments. In general a good data coverage could be achieved, especially next to the fault structure (around 122 km), with its complicated reflection pattern and low coherency values. Note that no events were picked from the pre-Messinian sediments at the base and underneath the MU and therefore velocities referring to that depth could not be properly estimated and most likely reflect the starting model.

In Figure 29(b) the corresponding prestack depth migrated section is shown. The image quality is very similar to the one obtained in the case of NIP-wave tomography. The upper sequence of sediments is clearly imaged and the top of the evaporites is well-defined. The salt layer itself is about 1400 m thick and the intra-evaporitic sequences can be traced easily since they are continuous over the section. Beneath the fault structure (at 122 km), the base of the evaporites is interrupted and downbended. Although there are picks available this area is not reliably imaged. It seems that not enough input information is present to describe the lower boundary of the salt properly. The derived velocities correlate quite well with the reflection characteristics of the particular Messinian sequences. The seismically transparent sequences ME-I, II, IV and VI reveal the highest velocities of up to 4.4 km/s which corresponds to their interpretation as halite (Hübscher and Netzeband, 2007b; Kearey and Brooks, 1991). The sequences ME-III and V which reveal a sub-parallel reflections pattern are characterized by lower velocities which suggest the presence of, e.g., intercalated clastics or evaporitic facies with lower velocities.
Figure 30(a) presents selected Common-Image gathers (CIGs) which are equally spaced over the whole section. A maximum offset of 3500 m is shown. The good quality of the image is reflected in mainly flat gathers throughout the whole section. However, at a depth of about 2100 m some negative residual moveout remains. Here, the strong increase in velocity related to the sediment-salt transition cannot be described correctly by the underlying assumption of a smooth velocity model. Nevertheless, the events at the base of the evaporites are flattened reasonably. We conclude that the estimation of a data consistent velocity model leading to flat image gathers was possible by prestack stereotomography.

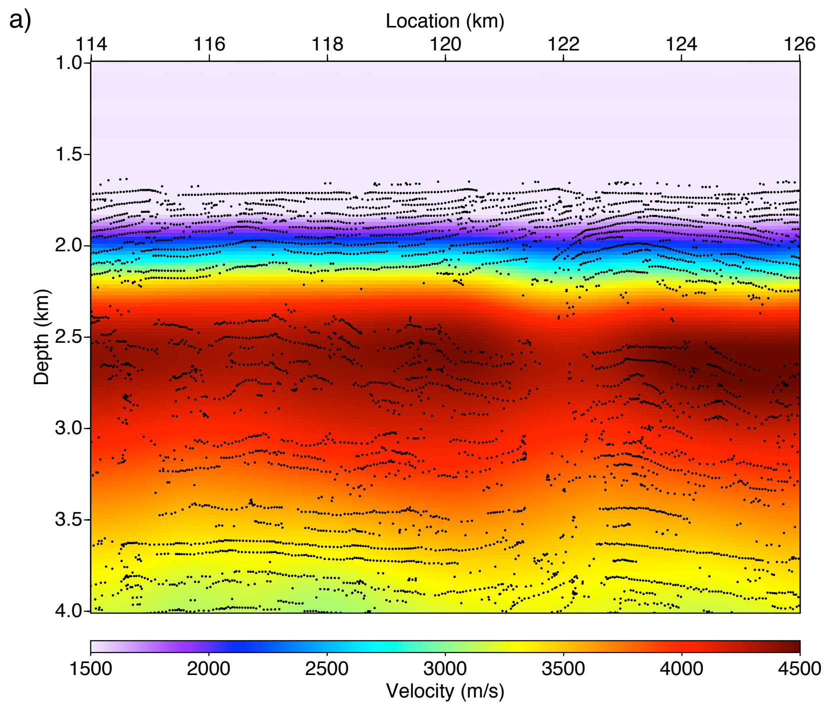

(a)

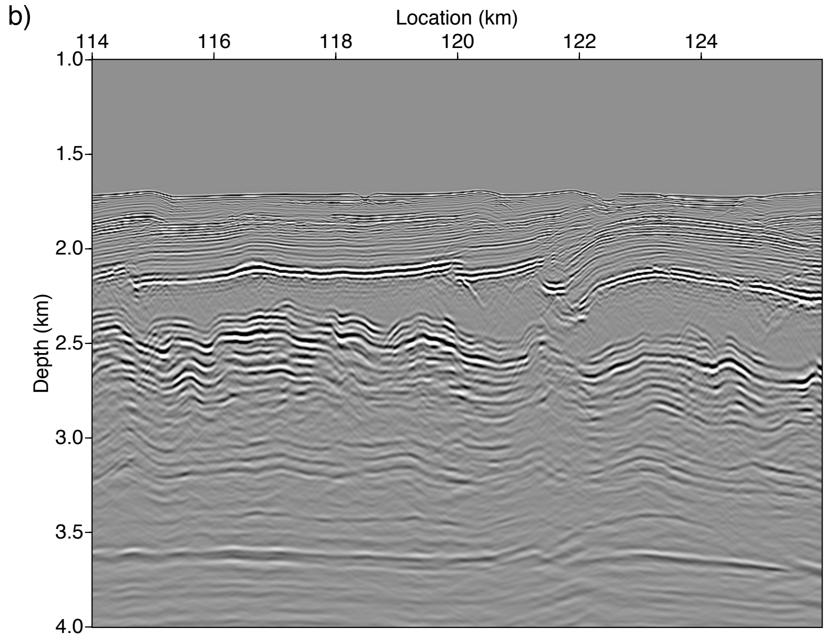

(b)

Figure 27: The result of NIP-wave tomography. The depth converted input picks associated with the corresponding NIPs are overlaid on the velocity distribution (a). Figure (b) shows the corresponding prestack depth migration result.

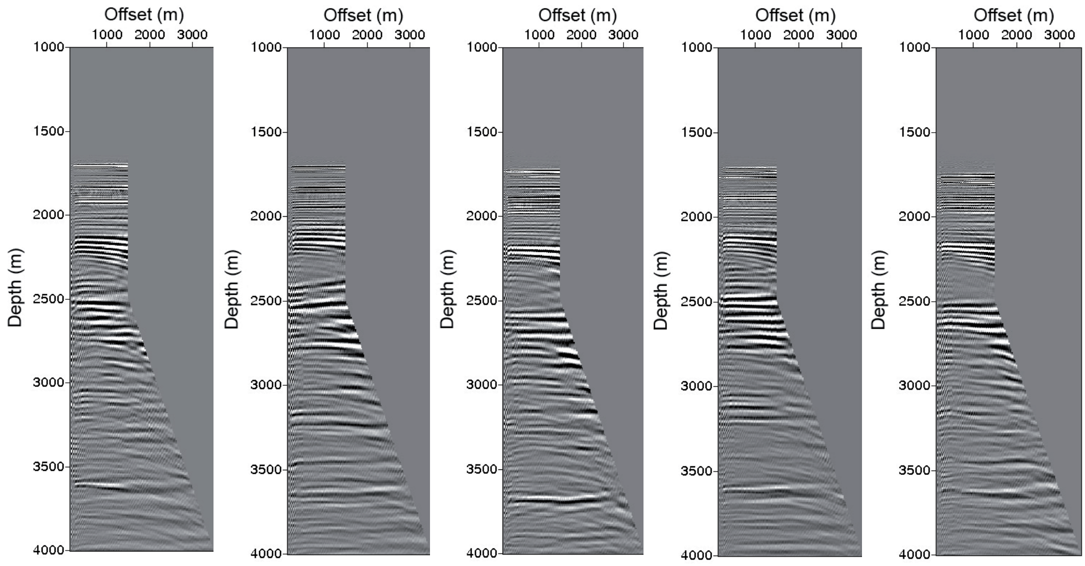

(a)

Figure 28: Selected Common Image gathers equally spaced over the whole section.

Comparison of the results As demonstrated by this field data example, both tomographic approaches provide a velocity model with a different vertical resolution, nevertheless leading to a clear image in depth based on flat common-image gathers. However, despite of the comparably high quality of the imaged sections, pronounced differences in the velocity distribution are present. Whereas the velocity model obtained by NIP-wave tomography shows a smoother lateral and vertical variation resulting in slight residual move-out in the vicinity of the fault structure, the stereotomographic velocity distribution is better constrained in this area and indicates a better lateral resolution. The velocities derived with stereotomography are more consistent with the geometry of the main reflections observed on the stack. These issues are directly linked to the approximation of the traveltime curves in the different approaches and the description via B-splines of different orders. In prestack stereotomography the traveltime is approximated by locally coherent events, i.e., stereotomography presents a local approach. In contrast to that, in NIP-wave tomography the traveltime curve is described by the second-order hyperbolic traveltime approximation, i.e., a more regional approach. Furthermore, prestack stereotomography uses a minor order of B-splines. These two facts explain the smoother velocity model obtained by NIP-wave tomography.
The data coverage in prestack stereotomography is in general higher than in NIP-wave tomography, especially near the fault system. This is due to the fact that different data domains are used for input data generation. The poststack data domain leads to a reduced data volume, but has disadvantages near fault systems, were the coherency values of the CRS stack decrease significantly. Despite of the data coverage picking in the prestack data domain is much more challenging than in the poststack data domain.
Generally higher average velocities are obtained by NIP-wave tomography over the whole profile part. This fact can be explained by the different regularizations of both methods. Whereas in NIP-wave tomography the smoothest solution is explicitly sought by employing a minimum curvature constraint directly to the velocity distribution itself, in prestack stereotomography the model vector is required to have a bound on its norm by a Tikhonov scheme. Depending on the regularisation weight, this may influence the velocity distributions in terms of average velocities.

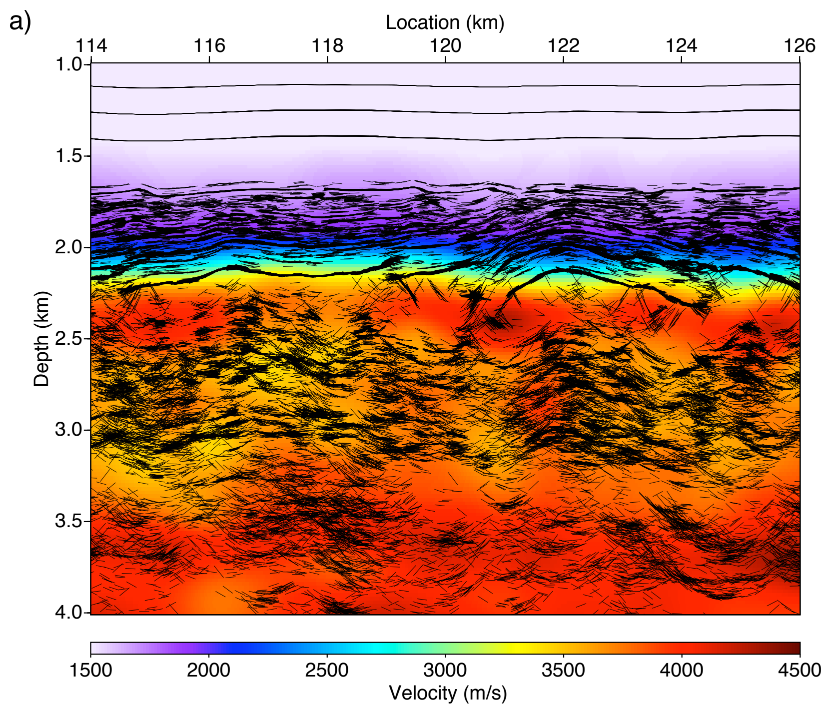

(a)

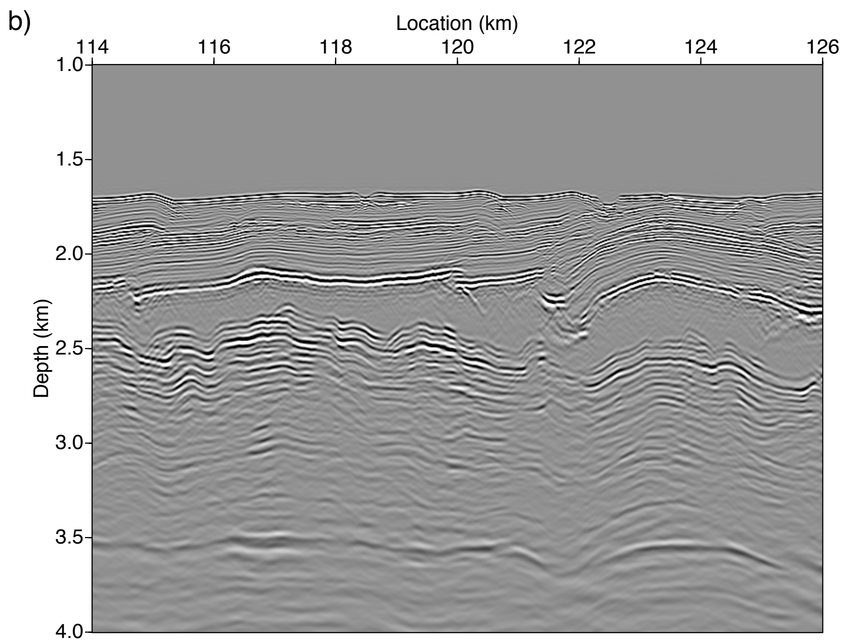

(b)

Figure 29: The result of prestack stereotomography. The velocity distribution is shown together with the depth converted input picks (a) and the corresponding prestack depth migration result (b).

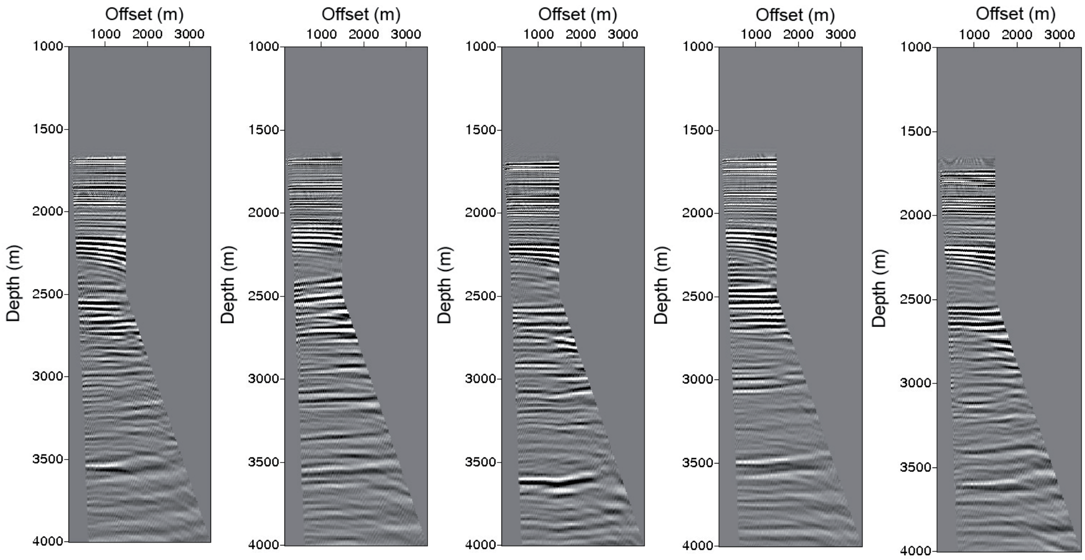

(a)

Figure 30: Selected Common Image gathers equally spaced over the whole section.

4.3.3 Proximal data example

Description of the section The second data example covers 1500 CMP locations. The associated CRS stack section is displayed in Figure 31(a). As the time section shows, the M-reflection can be identified at 2.7 s two-way traveltime in the left part of the section and at approximately 2.4 s in the right part. The subsequent layer of Messinian Evaporites covers only the seismically transparent sequences ME-I and III and can be observed only between position 145 km and 161 km. Salt roller structures can be found in form of triangular patterns. Again, below the N-reflection weaker reflections from pre-Messinian sediments can be recognized.

This data example is suitable to compare both methods in an area with strong lateral velocity variations, which occur in the salt roller area. In this complex geologic setting the lateral resolution of the velocity models obtained by both methods will be investigated and compared. Additionally, the quality of the resulting depth migrated images as well as the flatness of the associated CIGs will be evaluated.

Application of NIP-wave tomography In order to obtain the necessary input data for NIP-wave tomography, we applied again the CRS stack. The determination of the related apertures of the stacking operator had to be chosen carefully to ensure the most reliable attributes. Before stacking the data and picking of the attributes, the same preprocessing steps were performed as for the previous example. After application of the automated picking tool to extract the input picks for the inversion, a quality control sequence was applied. As before, the main criteria were stacking velocities and the position of picks.
To initialize the inversion we chose an initial B-spline node spacing of 500 m laterally and 125 m vertically and created an initial velocity model of $v(z) = 1500$ m/s$+0.5$ s^{-1}z. During the inversion the B-spline nodes in the water column were again forced to water velocity. The inversion algorithm performed a total of 10 joint inversions, before it reached the minimum of the cost function.
The resulting velocity distribution is shown in Figure 32(a).
Because of its smoothness, the velocity model is consistent with the seismic reflectors in a very gross sense only. In some areas, the pick coverage is quite coarse and in the region between 156 km and 164 km the N-reflection is not sufficiently described. The location of the seafloor is indicated by a smooth increase in velocity at depth ranging from 1100 m to 1300 m. A subsequent rise up to 1900 m/s corresponds to

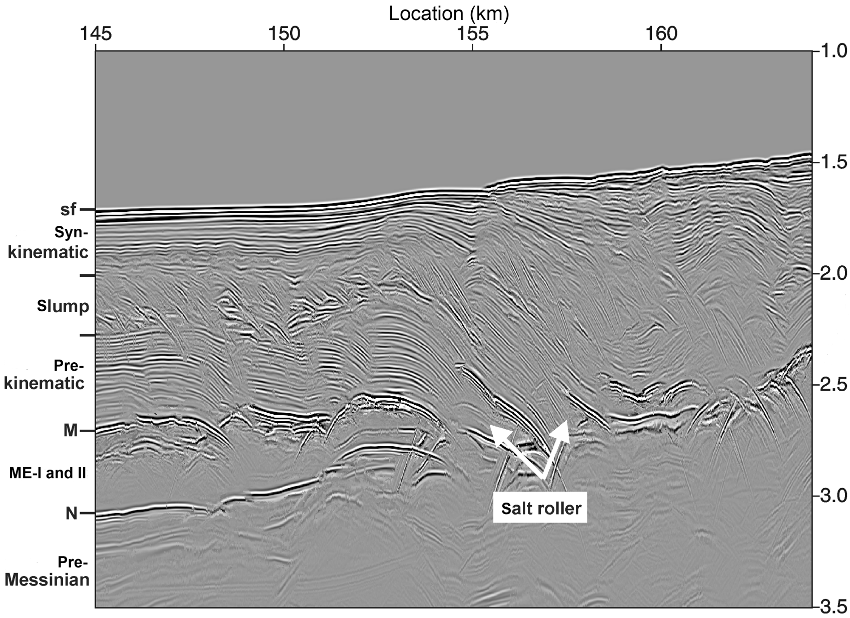

(a)

Figure 31: Proximal profile example. The MU pinch out to the right hand side of the section where salt rollers evolved. A slump subdivides the Pliocene-Quaternary overburden into a pre- and syn-kinematic succession (Netzeband et al., 2006b).

the layers above. Further in depth, the velocity increase continues quite evenly throughout the whole section and in the non-constraint regions it reflects given initial values. A large high-velocity zone between 145 km and 156 km comprising values up to 4000 m/s represents the evaporites with their base located slightly deeper than 3000 m.
To investigate the quality of the velocity model obtained by NIP-wave tomography, we carried out prestack depth migration, as in the first data example. The resulting depth image is presented in Figure 32(b). A good image quality was achieved. The overburden of sediments is clearly imaged and its thickness ranges from approximately 700 m to 1000 m. Extensional faults can be traced and some of them up to the sea-floor. Beneath the overburden, the top of the evaporites is well-defined and triangular patterns represent clearly the salt roller structures. The N reflection can be found at a maximum depth of 3000 m. In the right part of the section it is several times interrupted and shifted in depth. In the area around 148 km to 150 km the N reflection seems to be continuous. Generally the image demonstrates smooth variations and continuos reflectors, while the main geologic structures in this section are still clearly visible.

In Figure 33(a) selected CIGs which are equally spaced over the whole section are displayed. The overburden and the M-reflection are reasonably flattened. Some down-bended residual move-out can be observed at the M-reflection due to the smooth velocity description. An up-bending of the N-reflection can also be noted, indicating a too low average migration velocity. In the last three CIGs almost all reflections deeper than 2000 m in depth show some residual move-out, due to the fact that the inversion is not constrained by input data picks in that area. Thus the initial model remains in that profile part, causing residual moveout. Nevertheless, NIP-wave tomography led to an improved velocity model for further model refinements.

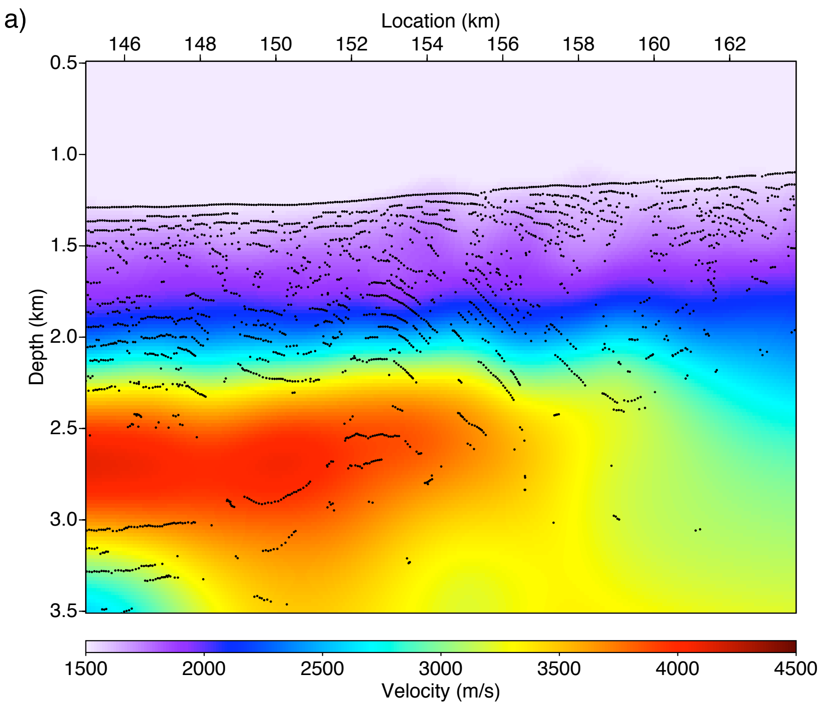

(a)

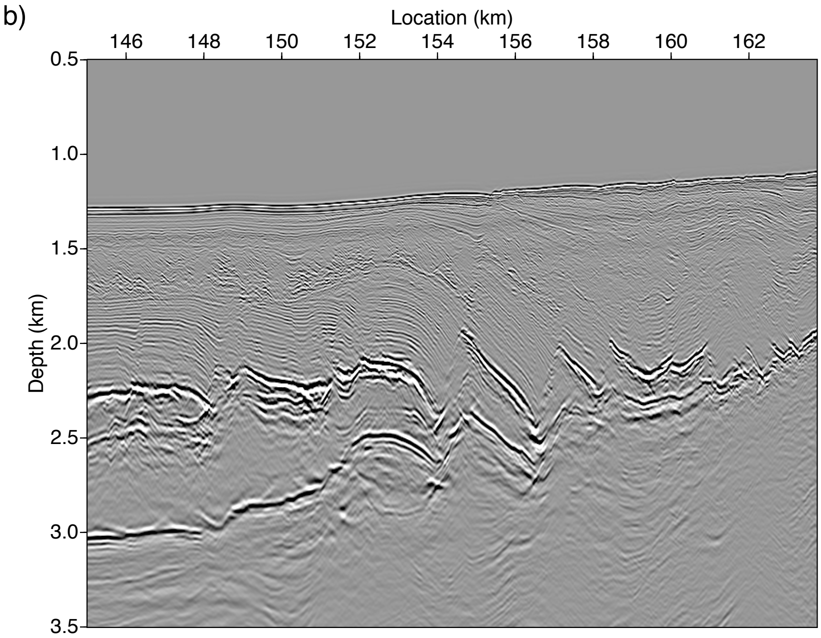

(b)

Figure 32: The result of NIP-wave tomography. Overlaid over the velocity distribution the depth converted input picks are imaged (a) and the corresponding prestack depth migration result (b).

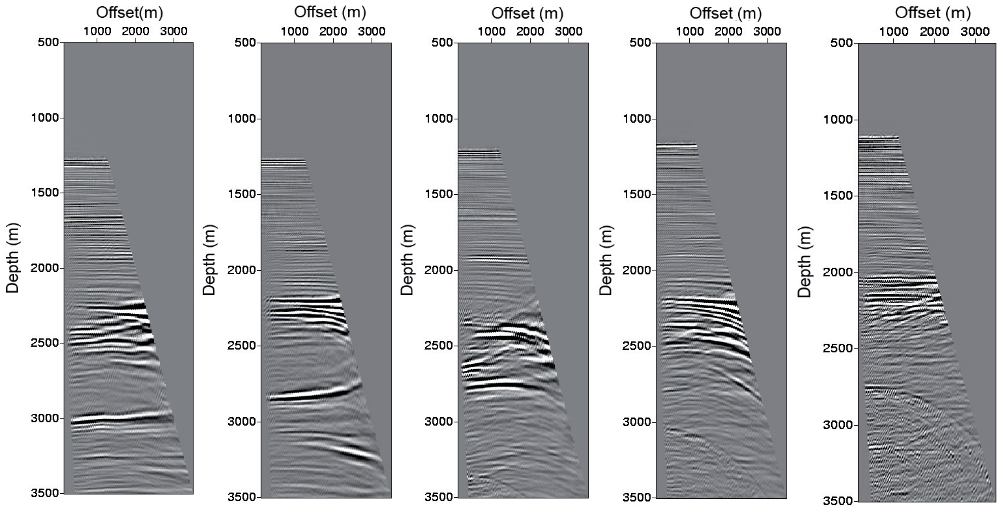

(a)

Figure 33: Selected Common Image gathers from the prestack depth migrated NIP-wave tomographic result, equally spaced over the whole profile part.

Application of prestack stereotomography As in the first data example, the determination of the required input picks had to proceed the velocity model building by prestack stereotomography. The same preprocessing steps were performed. After the automatic picking procedure a first interactive quality control sequence followed. Since the same strong differences in energy of the picks were observed in this data example, the data were split into three parts again. However, in contrast to the previous data case, the extracted input data already showed a good quality. Nevertheless, we repeated the same outlier removal sequence based on global normalized misfit. After this step the total input picks were introduced to the inversion scheme, starting with an initial model of $v(z) = 1500$ m/s+0.5 s^{-1}z and a B-spline grid spacing of 500 m laterally and 500 m vertically. Again we added artificial picks in the water column to stabilize the inversion. To start the inversion 10 localization steps preceded 20 joint inversion steps with a strong regularisation where an important decrease of the cost function occurred. The B-spline grid was then densified to 125 m vertically and further 11 iterations with a loose regularization led to the best result. In a total 31 joint inversion iterations were performed.

Figure 34(a) presents the result obtained by prestack stereo-tomography. Again, the depth converted input picks are overlaid on the velocity model. The velocity distribution coincides with the geological structures present in the stack section. The shallow part of the model is characterized by a smooth increase in velocity and in the subsequent part, a velocity increase up to 2600 m/s matches the structures of the sedimentary overburden. Distinctive triangular patterns related to the salt rollers can be identified in the velocity distribution. Between an inline distance of 145 km and 156 km, velocities ranging up to 3700 m/s represent the evaporites. A decrease in velocity indicates their pinch-out in the right part of the section. The input data coverage over the whole section is quite satisfactory. Below the MU hardly any picks were present, again.

Figure 34(b) represents the corresponding prestack depth migrated image. As before a good image quality was achieved and all assumed geological features are visible. On the left-hand side of the section the overburden and the top of salt reflection are located at almost the same positions as in the case of NIP-wave tomography. On the right-hand side some differences in the depth position of the top of salt reflection occur. The base of the evaporites is clearly mapped and reaches a maximum depth of about 3000 m. However, distinctive interruptions and rough variations in depth can be observed, especially in the region of the salt rollers. Generally the image seems rougher and the structures are less continuous than in the image based on the result of NIP-wave tomography.

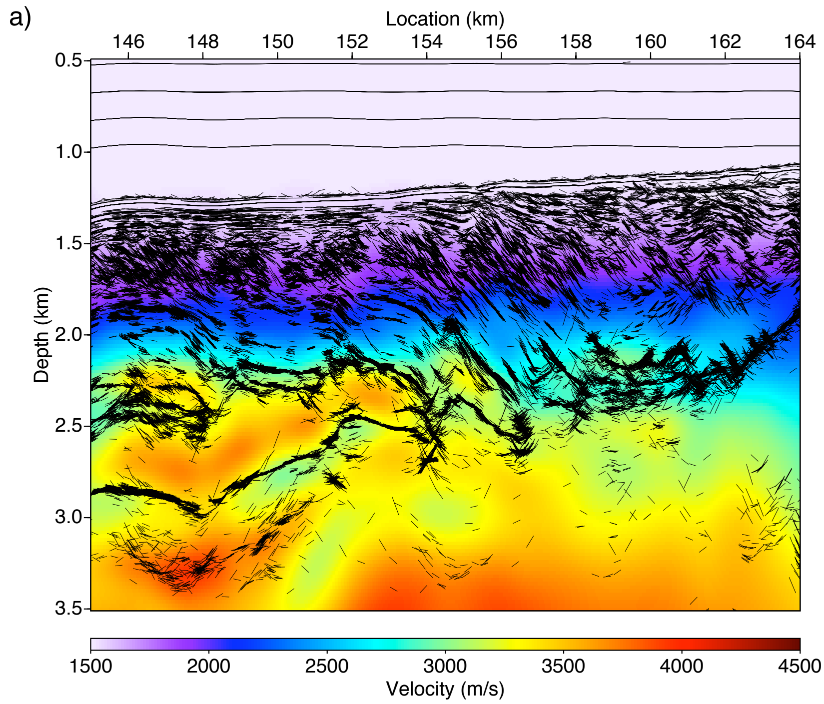

(a)

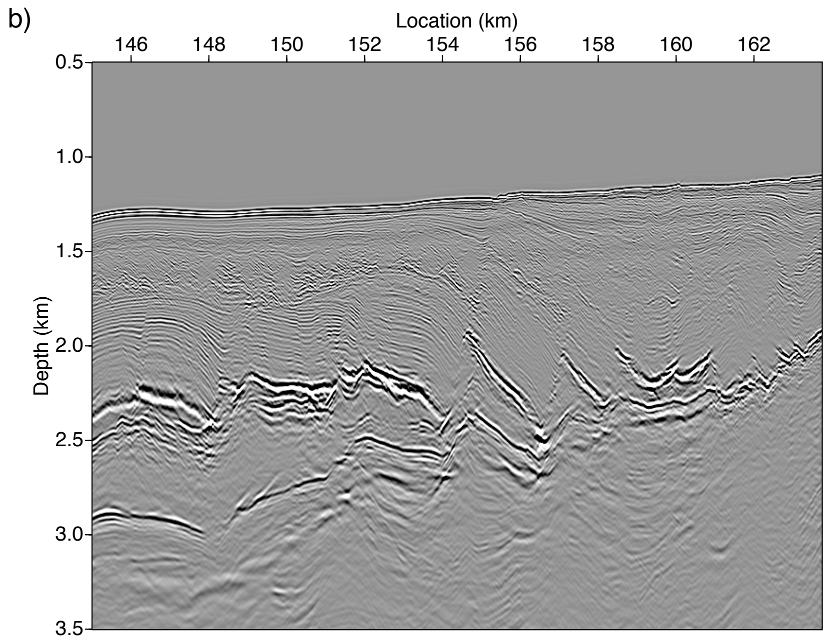

(b)

Figure 34: The result of prestack stereotomography. The depth converted input picks are plotted overlaid on the velocity model (a) and the corresponding prestack depth migration result (b).

The corresponding CIGs are shown in Figure 35(a). They reflect the good image quality. The reflections from the overburden are well flattened. The top of salt reflection shows some negative residual move-out for the same reason as in the first data example. Again, the strong velocity contrast could not be described properly by the smooth model. The first two gathers in the region of the salt body, show some positive residual move-out, indicating a too low migration velocity. As a consequence, the depth of the N-reflection is not reliably determined. In the last three CIGs some slight down-bending for the strong reflections at 2000 m depth is observed, indicating a too high migration velocity. However, the CIGs indicate a good result in general. Nevertheless, it has to be noted that the model obtained by prestack stereotomography does not lead a superior depth section in spite of a good lateral resolution. It represents however a high quality initial model for a further refinement by velocity model updating techniques.

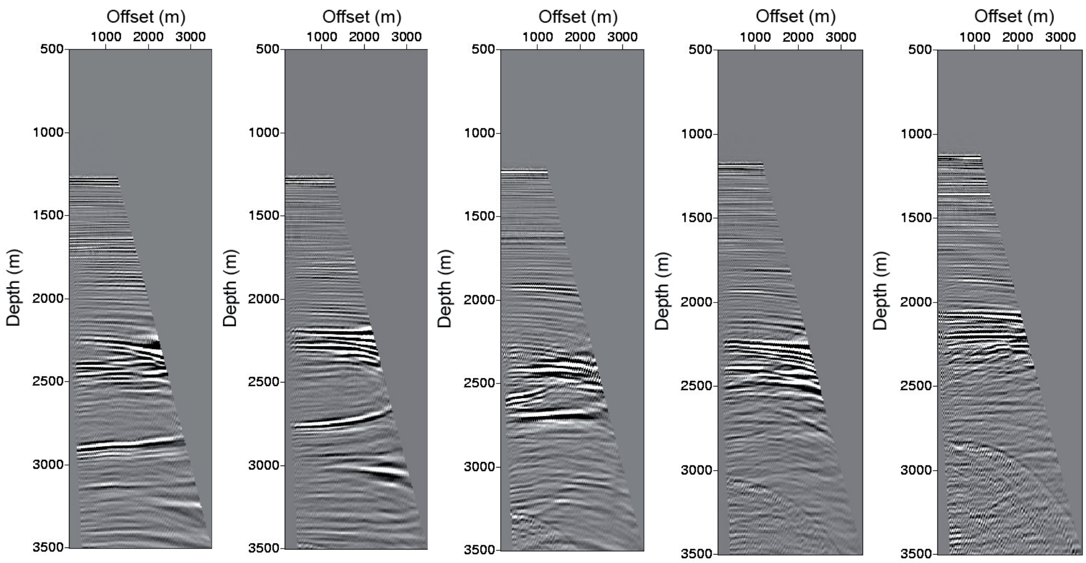

(a)

Figure 35: Selected Common Image gathers equally spaced over the whole profile part.

Comparison of the results As shown by this field data example, both tomographic methods provide velocity models indicating major differences in the presence of strong lateral velocity contrasts. Whereas the velocity distribution found by prestack stereo-tomography (Figure 34(a)) resolves all important lateral velocity contrasts, the NIP-wave tomographic model (Figure 32(a)) features only smooth velocity variations and the distribution is more smeared over the section. This is again linked to the three major theoretical differences of both methods: the approximation of traveltime curves, the different order of B-splines employed, and the different regularizations of the inverse problem.

As in the previous data example the data coverage was better in prestack stereotomography than in NIP-wave tomography. More picks could be obtained and consequently complicated geological regions are better constrained. However, the quality control and the preprocessing was much more challenging than in the case of NIP-wave tomography. Owing to the picking of the data in the prestack data domain with its relatively low signal-to-noise ratio a lot of outliers are selected. By contrast, NIP-wave tomography has some disadvantages in the data coverage, but generally produces sufficient data to describe the most important features.

The image quality of both prestack depth migration results is comparable, but some differences in the depth location of the reflectors and structural details occur. NIP-wave tomography produces smoother, horizontally more aligned events, while prestack stereotomography produces a rougher image. This is a direct consequence of the corresponding velocity distributions.

Despite the good quality of the related imaged sections, some residual move-out remains in the area of the salt body in both cases. The determination of a data consistent velocity model in terms of flat image gathers was not completely satisfactory in that region.

5 SUMMARY AND CONCLUSION OF THE METHODICAL CONSIDERATIONS

In this section the three previous methodical chapters will be summarized and discussed in detail. Each chapter will be discussed individually, conclusions and outlooks will be given.

5.1 Geological constrained CRS parameter search

In the first study, we reviewed the CRS stack formulation and indicated potential ways to constrain the parameter determination in a geological reasonable way.

The CRS stack formula can be derived from a Taylor expansion in source and receiver coordinates of the squared traveltime. The corresponding stacking parameters, the angle of emergence, the radius of the Normal-wave, and the radius of the Normal-Incidence-Point-wave can be linked to first and second order derivatives of the traveltime with respect to the source and receiver coordinates. They can also be linked to conventional processing parameters, e.g., the stacking velocity. Due to the fact, that the expansion is performed in two coordinates the stacking operator is capable to stack more traces into one CMP position compared to the conventional CMP stacking process. This results in a high quality stacked section in terms of signal to noise ratio.

The CRS attributes or stacking parameters serve as input for a lot of subsequent applications (Duveneck, 2004b; Baykulov and Gajewski, 2009a). Thus, they have to be estimated as reliable as possible. To achieve this, we introduced geological constrains in the parameter determination.

For the determination of the stacking velocity, which can be expressed as a combination of two CRS attributes, we introduced a dynamic stacking velocity interval restriction. This avoids the determination of stacking velocities with geological unreasonably low values. This restriction is mainly based on the assumption that the stacking velocity increases or stays constant with time, which is often fulfilled in real geological models. The results obtained on the data set from the Eastern Mediterranean show that the approach is suitable to determine well constrained velocity models in an automated way, without any previous knowledge of the stacking velocity model. Thus, the geological constrained automated CMP stacking process is suitable as a 'on-site' processing tool, for a quick and automated glance at the subsurface structures, generated parallel to data acquisition.

For the determination of the angle of emergence and the radius of the Normal-wave, we applied dip-filtering on the CMP stacked section, which serves as input for the ZO parameter determinations. Afterwards, the parameter searches are better constrained, due to the fact that we removed unwanted events of the data, like diffractions, coherent noise, etc. The applicability of this approach depends on the geological situation. For example, if reflection events and diffraction hyperbolas have locally the same dip, the approach is not applicable. Nevertheless, if the geological situation allows to process the CMP stack in such a way, the parameter search will benefit from this and produce less outliers/fluctuations in the parameter sections. A windowed application of this approach is practicable, if the parameter search can be constrained only in certain areas. The results from the Eastern Mediterranean show that the angle of emergence determination benefits a lot from such a search strategy. Far less parameter fluctuations and outliers were found compared to the interval constrained approach. However, this approach has not such a big impact in the determination of the radius of curvature of the Normal-wave, due to the locally flat reflections in the data. Nevertheless, if the quality of the CMP stack can be enhanced the parameter estimation will also benefit from this.

In general, it can be said, that the parameter determination benefits a lot from introducing geological parameter constrains. The dynamic stacking velocity restriction as well as the dip filtering of the CMP stacked section can produce better constrained parameter sections without previous knowledge of the subsurface.

5.2 Multiple attenuation with CRS attributes

In the second study, we developed two approaches for multiple attenuation that could be directly incorporated into the existing CRS workflow. Both approaches rely on the quality of the CRS attributes. The first algorithm is based on predicting the multiples in the poststack data domain and subtracting them in the prestack data domain. The predicted multiples are transformed back to the prestack data domain by the CRS attributes.
The second approach can be considered as a data conditioning tool for a subsequent SRME process with the help of partial CRS stacks. These data are then perfectly suitable for the subsequent SRME process. Additionally, we also show a simplified version of the SRME method, neglecting the wavelet knowledge. Instead of this, we correct the prestack multiple prediction with a image matching process.

The first approach was implemented on the basis of a poststack SRME multiple prediction process (Kelamis and Verschuur, 1996). Afterwards a correction term is introduced based on a 2D cross correlation, which accounts for the inherent prediction errors of the poststack SRME process. The correction term is not valid for each multiple independently, but can produce sufficient results to address the main prediction errors. Alternatively, a global shift or a windowed application of the correction term is possible. Then, the CRS attributes of the multiples are identified and prestack seismograms are generated within the hyperbolic assumption. These predicted multiples are subtracted from the data in a least square sense.
The results from the Maldives data set and from the Eastern Mediterranean illustrate the potential and the limits of this method quite well. For the first data set, a lot of multiple energy was removed and primary energy was recovered, whereas on the second one a lot of residuals remained. On this data set the behaviour of the multiples is quite complex due to the complicated structure of the multiple generating horizons. Consequently, the results suffer from the complicated determination of the CRS attributes. The obtained results, however, are still comparable to the results obtained by Radon filtering.
It should be mentioned that the applied correction term in this approach is only accounting roughly for the prediction errors. The obtained result is not as accurate as a 2D SRME prediction. However, as can be seen on the data examples, it can still produce reasonable results. Another limiting factor of the algorithm is its restriction to the hyperbolic assumption. In complex geologic situations this assumption may be violated and the algorithm then produces an insufficient multiple only data set.
On the other hand, the main advantage of this approach is its simplicity and speed. The algorithm is independent of data regularization and can handle sparse data without any complications. Therefore, the approach is best suited as a supplemental tool in the CRS workflow. As long as reliable CRS attributes are determined and the prediction is sufficiently accurate surface related multiples can be attenuated quite well. The application of partial CRS stacks to the data additionally removed filtering artefacts and helped to reconstruct affected primaries.

The second approach dropped some limitations of the first approach and better described the wavefield propagation in the subsurface. The results show an improvement of the multiple prediction in general, since the 1D approximation was avoided. However, the better wavefield description is computationally more demanding.
The original SRME process (Verschuur et al., 1992) requires regular data in terms of shot and receiver spacing, as well as the knowledge of the source wavelet. These conditions are normally quite challenging to obtain during the seismic data processing chain. Here, we tried to overcome these limitation with tools already introduced in this thesis. The first drawback was addressed using partial CRS stacks (Baykulov and Gajewski, 2009b) which closed the initial offset data gaps, interpolated the data in case of missing traces, and regularised the shot and receiver spacing in case of non equal source and receiver spacing. These abilities make the application of the SRME prediction feasible. The partial CRS stacks can also be used to generate traces at negative offsets. This would then as well benefit the multiple prediction (Verschuur, 2006). Consequently, we could generate perfectly regularised data for the SRME prediction process based on CRS attributes.
The second drawback is addressed with the help of an image matching process, i.e., a 2D cross correlation process. Thus, we do not require the knowledge of the source wavelet and thus avoid non-linear optimisations. By assuming the change of wavelet is small with offset, i.e., not considering overcritical reflections,

we can correct the prestack multiple prediction with a global shift determined by a 2D cross correlation.
The results for the second data set from the Eastern Mediterranean show the potential of combining partial CRS stacks and the SRME prediction. More multiple energy was removed compared to first approach. The prediction of the multiples is more accurate leading to an improved attenuation. However, to get a more accurate prediction the determination of the source wavelet is still mandatory. Therefore, it can be also thought of using partial CRS stacks as input for the original SRME process. The proposed approach has a big potential for land data, since partial CRS stacks enhance the quality and the regularity of prestack data (Baykulov and Gajewski, 2009b). The original SRME could be applied to land data sets, without the usually mandatory SRME pre-conditioning.

A straight forward extension to both presented methods is to include CRS gathers into the adaptive subtraction process. According to Verschuur (2006) this may lead to a balancing of the prediction errors in the subtraction process, since in a CRS gather many CMP gathers are included and small timing errors could be balanced.
Further extension can be achieved by incorporating more sophisticated adaptive subtraction methods. Currently, techniques are evaluated for multiple attenuation like curve-lets (Herrmann and Verschuur, 2004), complex curvelets (Neelamani et al., 2008), or a combination of pattern / dip based methods (Donno et al., 2008). The first two approaches would not be well suited to incorporate them into a CRS based multiple attenuation approach, since the demands on the accuracy of the predictions are quite high. But in the latter approach, we see a lot of potential for the CRS stacking technology, since the traveltime curve of a reflection event is specified by its CRS attributes (i.e., the angle of emergence and two radii of curvatures). This could be used to focus the adaptive subtraction process to the relevant positions in the data and add some more kinematic information of the considered events into the subtraction process, especially for conflicting dip situations.

The described CRS based techniques are easily extendable to the 3D case. For the poststack SRME process, this would lead to correction terms applied for every inline or crossline direction in the data cube. This process can be directly extended and all its benefits would remain. The correction term can also be extended to the 3D case by using a 3D cross correlation algorithm.
For the second approach, the partial CRS stacking technology has to be extended to the 3D case and could then be directly used to regularise the data in such a way, that a complete 3D SRME multiple prediction can be performed. Since the partial CRS stacks rely on kinematic wavefield attributes, they are much less sensitive to sampling issues than wave equation based methods for data regularisation. Partial stacks can be applied to sparse data as typically acquired in 3D marine acquisitions.

When the data is regularised with the partial CRS stack technology, it is also well prepared for the so-called virtual real source technology (Behura, 2007), which can estimate the source wavelet from seismic interferrometry. Here, basically two receiver gather are cross correlated to determine the source signal from the resulting correlation function. The special needs in terms of source and receiver locations can be fulfilled with the help of partial CRS stacks. Afterwards, the determined source wavelet could be used in the multiples prediction process.

5.3 Comparison of prestack stereotomography and NIP-wave tomography for velocity model building

In the third methodical chapter, we have shown a comparison between two grid-based tomographic approaches for velocity model determination under equal initial conditions, i.e., the same preprocessing, the same B-spline grid spacing, and the same starting model for the inversion. The resulting models produce data consistent results in most areas but produce different velocity distributions. The flatness of the Common Image gathers was the main criteria to asses the obtained results. The most striking differences are the resolution of the velocity models, the description of the model near fault zones, and the average velocities within a salt body. These three points are directly linked to differences of the methods compared in this paper.
Additionally individual evaporite sequences have been characterized by seismic velocities for the very first

time. The derived sequence of velocities of the distal evaporites foster previously published interpretations of a vertical succession of altering evaporite facies or intercalated clastics.

The different resolution of the velocity distribution is directly linked to the differences of both methods. Especially the different lateral resolution may be explained by the differing approximation of the traveltime curves. Prestack stereotomography represents the traveltime curves by slopes of locally coherent events. Only a part of the traveltime curve is described by its tangent (local approach) and therefore complex shaped traveltime curves may be accounted for. In NIP-wave tomography, over a large offset range, the traveltime curve is approximated hyperbolically, hence it is a regional approach. Seismic events are assumed to be hyperbolic, otherwise they are not inverted correctly. This reduces the applicability of the method to moderate laterally inhomogeneous media. The lateral and the vertical resolution of the models are also influenced by the second major difference, which is the order of B-splines employed. In contrast to prestack stereotomography, NIP-wave tomography uses B-splines of a higher order. This results in a velocity distribution which is smoother in the vertical and the lateral direction.
The differences in the description of the model near fault zones are mainly related to two points. First, the input data for both tomographic approaches are determined in two different data domains. In prestack stereotomography the input data is obtained in the prestack data domain by an automated picking tool, based on local slant stack panels. In contrast, in NIP-wave tomography the input data is automatically picked in the poststack data domain using the results of the CRS stack. Although the input data determination in the prestack data domain and the quality control is more challenging, especially in regions with complex geological features yielding a decrease in coherency, the determination in the prestack data domain leads to a better data coverage. In NIP-wave tomography, the input data determination is simplified due to the high signal to noise ratio in the poststack data domain. However, in areas referring to fault systems, it is challenging to determine reliable attributes, due to the fact that the spatial CRS stacking operator is not well suited for the description of fault zones. The second reason for the differences occurring near fault systems is again the different representations of the traveltime curves mentioned above, which is directly linked to the first reason.
The third major difference is the average velocity in the salt body. NIP-wave tomography produces higher average velocities than prestack stereotomography. On the one hand, this may be related to the common work flow (same preprocessing, same B-spline node spacing, same starting model) used for the comparison of both methods, leading to models that are not necessarily the best models that could be achieved with both approaches. On the other hand, the different average velocities may be related to the different regularizations of the approaches. Whereas in NIP-wave tomography the smoothest solution is explicitly sought by employing a minimum curvature constraint directly on the velocity information, in prestack stereotomography the model vector is required to have a bound on its norm by a Tikhonov scheme. Depending on the regularisation weight, this may influence the velocity distributions also in terms of average velocities.

As seen before the major differences in the inversion results are directly linked to the formulation / implementation of both methods. The tomographic problems can be summarized as follows: in prestack stereotomography local slopes, their corresponding two-way traveltimes and spatial positions are used as input. In NIP-wave tomography the zero-offset traveltime, the spatial position, the horizontal slowness component, and the second-order spatial derivatives of the traveltime are used. In both methods, the input data is fitted in a least square sense to modeled data calculated by dynamic ray-tracing using a conjugate gradient like inversion scheme and a smooth velocity model is obtained that serves as a good starting model for further residual moveout analysis.

6 INTERPRETATION EXAMPLE OF AN EXPANDED CRS WORKFLOW PROCESSED DATA SET: STRATIGRAPHY, DISTRIBUTION AND PLATE TECTONIC OVERPRINT OF THE MESSINIAN EVAPORITES IN THE LEVANTINE BASIN

This chapter presents an example for a resulting geologic interpretation of a data set that was processed with the expanded CRS workflow, we presented before.

6.1 Introduction

The structural evolution of the Levantine Basin in terms of plate and salt tectonics, stratigraphy and fluid dynamics has been intensely discussed among the scientific community during the last three decades. Since the beginning of this century, the understanding of the geological evolution of this easternmost and semi-enclosed Mediterranean Basin has been significantly increased when new academic studies were carried out (e.g., Gradmann et al. (2005); Netzeband et al. (2006b,a); Schattner et al. (2006); Hübscher and Netzeband (2007b) and industrial 3D-seismic data were released (Bertoni and Cartwright, 2006, 2007; Frey-Martinez et al., 2005). However, controversy continues as whether there is any active plate tectonic driven deformation in the Levantine Basin. However, most authors agree that the transition between the deformed area onland and the mainly undeformed Levantine Basin occurs along the base of the continental slope (e.g., Gradmann et al. (2005); Netzeband et al. (2006b); Schattner et al. (2006)). The difficulty in proving any aseismic or "silent" plate tectonics results mainly from the presence of up to 2 km thick Messinian evaporites within the basin. These tabular and ductile salt giant decouples mechanically the sub-salt domain from the overburden (Warren, 2006). Hence, deep rooted folds and faults can often not be traced across the salt layer.
The identification of tectonic faults in the sub-salt domain is difficult, since thickness undulations of the high-velocity salt layer might cause wrong velocity estimations and the structures beneath the salt are imaged in a wrong position. This distortion may pretend the presence of folds or faults even if the real horizons are undisturbed.
The academic interest in the Levantine Basin is motivated by the understanding that the early structural deformation of a tabular salt giant, like the Messinian Evaporites, can be studied best in this basin, since the geometry of the mobile basinal unit is still close to its original state. Gradmann et al. (2005) discussed the rheology of individual evaporite sequences for the first time, this issue attracted a lot of attention later on (Bertoni and Cartwright (2006); Netzeband et al. (2006b); Cartwright and Jackson (2008); Hübscher et al. (2009)). However, the direct relationship between the deformation of individual salt sequences and its overburden on one side and plate tectonics on the other side remains unclear. Among others, one reason is that the basin wide stratigraphy of the individual salt sequences has not been mapped yet and, consequently, the spatial relationship between plate tectonic lineaments and deformation pattern in the salt and its overburden could not be investigated.
In this study, we address the stratigraphy and plate tectonic overprint of Levantine Basin fill deposits with special emphasis on the Messinian evaporites. Prestack depth migrated seismic data illustrates the thickness of individual sequences and the evaporites are characterised by interval velocities. Basin wide maps of the residual topography, residual Bouguer gravity and basement depth represent a data set, which is independent from the seismic data. Since these data sets are independently derived, the joint interpretation of all available data helps to distinguish between apparent or plate tectonic deformation of Levantine basin fill deposits.

6.2 Regional setting

It is generally assumed that the Eastern Mediterranean, and the Levantine basin therein, formed during the tectonic breakup of the Pangea Supercontinent in an initial rifting phase during Mid-Permian to Middle Jurassic times (Robertson and Comas, 1998; Roberts and Peace, 2007). The Levantine basin, which is the central working area in this paper, is considered as a relic of the Mesozoic Neo-Tethys ocean (Stampfli and Borel (2002); Garfunkel (2004)). The basin is confined to the east and south by the Levantine and Egyptian coasts, to the north by Cyprus and to the west by the Eratosthenes Seamount and the Herodotus basin (Figure 36(a)). Currently, the main tectonic movement direction in this area is driven by the northward movement of the African plate (Figure 36(a)).

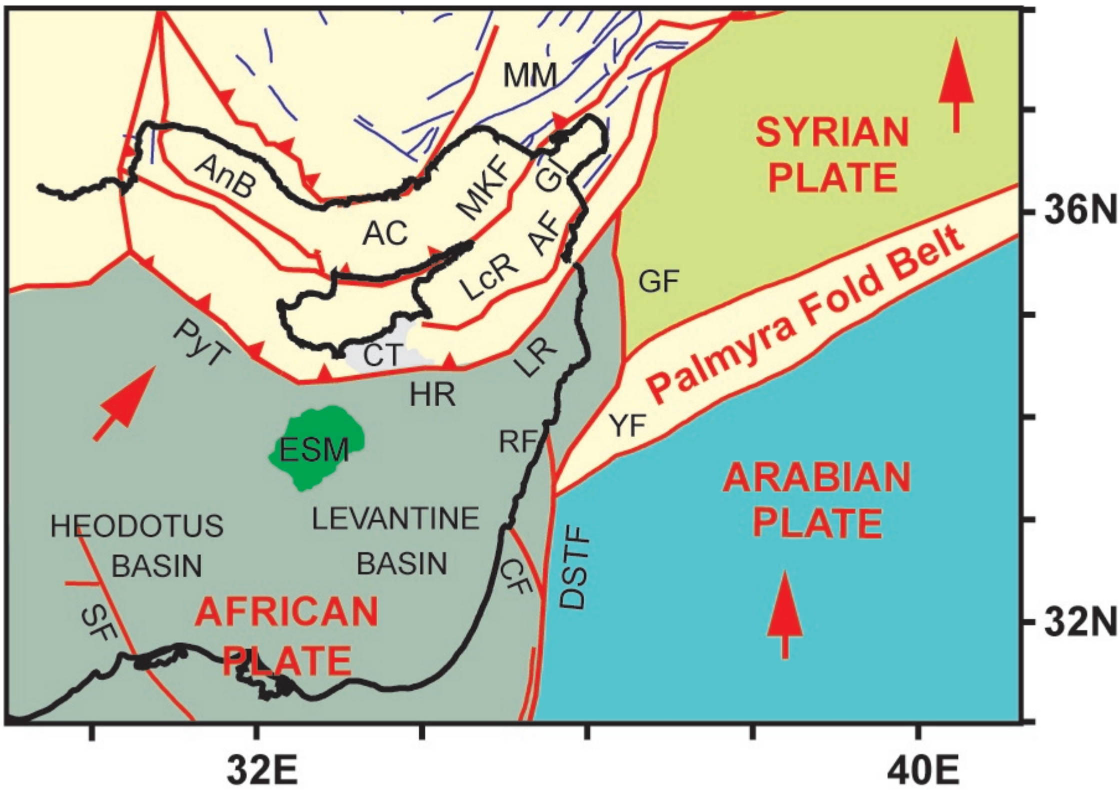

(a)

Figure 36: Geological map of the Eastern Mediterranean, including the main geological features (AC=Adana-Cilicia Basin; CF=Carmel Fault; CT=Cyprus Trench; DSTF=Dead Sea Transform Fault; ESM=Eratosthenes Seamount; GI=Gulf of Iskenderun; GF= Ghab Fault; HR=Hecateus Ridge; LR=Latakia Ridge; LcR=Larnaca Ridge; MKF=MisisKyrenia Fault Zone; MM=Misis Mountains; PyT=Pytheus Trench; SF=Sinai Fault; YF= Yamouneh Fault) modified after Aksu et al. (2005).

The Levantine basin has undergone subsidence for more than 100Ma (Mart and Bengai (1982); Tibor et al. (1992); Almagor (1993); Vidal et al. (2000)) and is still subsiding, while the Levantine hinterland is doming up. The formation of the Levantine basin starts in Mesozoic times. During this time, the regional tectonic regime in the Levantine basin can be characterised as an initial rifting/extension phase, mainly dominated by the breakup of Gondwana (e.g., Garfunkel (2004)). In Cretaceous times, the development of the basin leads to a passive margin configuration when the initial rifting movement ended (Farris and Griffiths, 2003).

A fold belt, which extends from the northern part of Egypt into NNE direction and runs parallel to the Levantine coastline has been termed Syrian Arc fold belt (Walley, 1998). This fold belt is the recent expression of the so-called Syrian Arc inversion during the development of the Levantine basin. The northward movement of the African plate initially drove the Syrian Arc inversion, when the tectonic regime in the basin turned from a passive margin to a compression and wrench setting (Farris and Griffiths, 2003). After the Syrian Arc inversion, the subduction of the African plate south of Cyprus started. Therefore, the current tectonic regime in the Eastern Mediterranean is considered as compression and wrench.

In the Levantine Basin, deep-rooted fault lineaments, i.e., the Pelusium line, the Damietta-Latakia line, and the Baltim-Hecateus line, mainly trending NNE-SSW parallel to the Syrian Arc fold belt, have been observed onshore by Mart and Bengai (1982) and offshore by e.g., Neev (1975), Abdel Aal et al. (2000), and Farris and Griffiths (2003). Further to the east the Dead Sea Transform fault (DSTF) forms a crucial part of the plate boundary network in the Eastern Mediterranean area (e.g. Kempler and Garfunkel (1994) and the references therein; Figure 36(a)). It has accommodated the differential opening between the Red Sea and Gulf of Suez (Girdler and Southren, 1987), showing about $105 - 110$km of left-lateral displacement. The transform fault system consists of three fundamental portions (e.g., Butler et al. (1997)). In the south, it is weakly transtensional and offsets are readily determined by the displacement of steep, pre-existing structures (Garfunkel, 1981). The northern segment, the Ghab fault, apparently joins with the continental collision zone at the left-lateral East Anatolian Fault of SE Turkey (Zak and Freund, 1981). Linking these two portions is the middle / Lebanese segment, i.e., the Yamouneh fault, of the transform (Figure 36(a)). Two branches of the DSTF trend towards the Eastern Mediterranean, the NW trending Carmel fault north of Haifa (Schattner et al., 2006) and further north the NNW trending Roum fault (Schattner et al., 2006), whereas the exact prolongation of the Carmel fault is still a matter of debate. In the slope areas of the southern Levantine coast, submarine canyons developed since the Oligocene. They are named the Afiq / Beer-Sheva, El Arish, and Ashdod canyon (Druckman et al., 1995; Buchbinder and Zilberman, 1997).

A modified tectonostratigraphic framework after Farris and Griffiths (2003) can be seen in Figure 37(a). It illustrates the evolution of the Levantine basin from Triassic to recent times and summarizes the above mentioned. Additionally, two stratigraphy models are also included into the illustration, one model after Gardosh and Druckman (2005) (SA) and one after Farris and Griffiths (2003) (SB), which will be the base of our stratigraphic interpretation in the following.

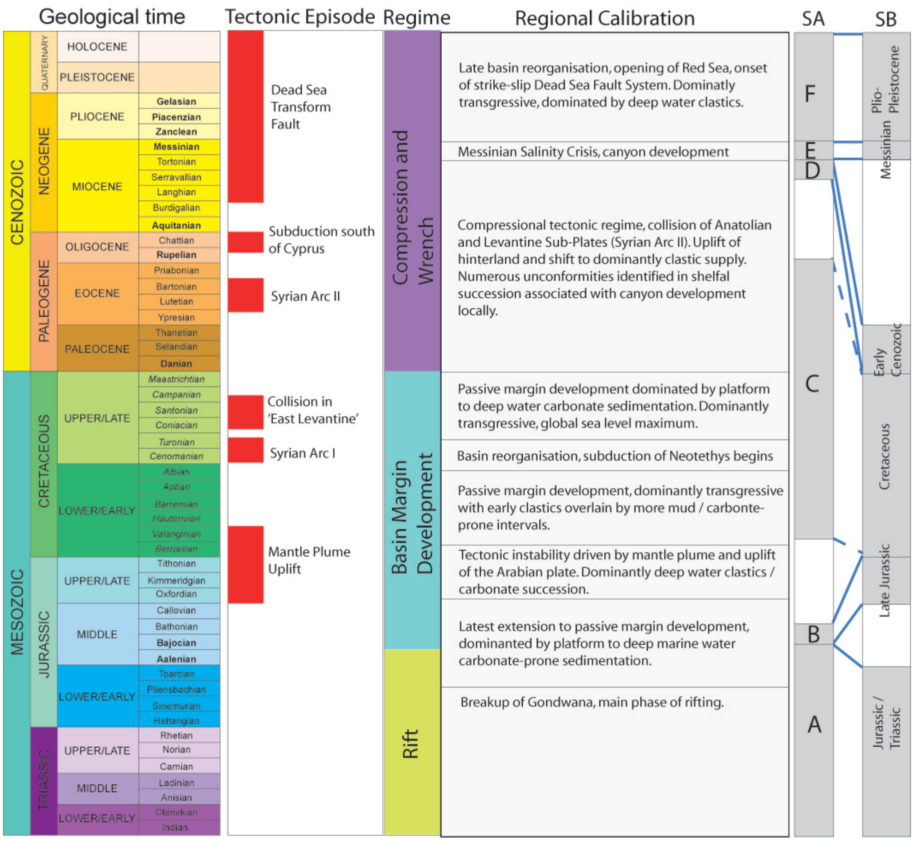

(a)

Figure 37: Tectonostratigraphic framework for the Eastern Mediterranean / Levantine basin modified after Farris and Griffiths (2003). SA indicate the stratigraphic model after Gardosh and Druckman (2005) and SB indicate the startigraphic model after Farris and Griffiths (2003).

Several authors postulated up to 14km of sediments for the Levantine basin (Farris and Griffiths, 2003; Gardosh and Druckman, 2005; Netzeband et al., 2006a) mainly consisting of Triassic to recent sediments. The basin fill is composed of a carbonate layer of Cretaceous to Jurassic/Triassic age, Paleogene to Neogene pelagic sediments, a layer of Messinian evaporites, and Plio-Pleistocene sediments at the top (Farris and Griffiths, 2003). It was shown from marginal well information that the Plio-Pleistocene mainly consists of claystone and siltstone. Recently, isolated coarser-grained sand bodies were also detected inside this formation (Gardosh and Druckman, 2005). Tibor et al. (1992) identified sedimentation rates of 162m/Ma for borehole Echo-1 in water depth greater than 50m and 111m/Ma in borehole Delta-1 in approximately 120m dep-ths for the Levantine basin.

At the end of the Miocene, the onset of the Messinian Salinity Crisis (MSC) caused extensive erosion and evaporite deposition in the Levantine basin (Hsü et al., 1980; Druckman et al., 1995). The reconstruction of the MSC, especially the linking between the western and the eastern Mediterranean is mainly done on the basis of marginal exposures and wells (e.g., Rouchy and Caruso (2006)) and the references therein), but the deep basin reconstructions still has to rely completely on seismic interpretation. Bertoni and Cartwright (2006) described the top and the base of the basinal Messi-nian evaporites as a high amplitude reflection. Additionally, several authors identified six intra evaporitic sequences (e.g., M20-M60 in Bertoni and Cartwright (2006) and ME-I-ME-VI in Hübscher and Netzeband (2007b)). Mainly three explanations have been given, which are interbedded shales, different evaporites from several depositional cycles. According to Bertoni and Cartwright (2006) and others all internal sequences are faulted and folded independently.

In Netzeband et al. (2006b) it was proposed that the Messinian evaporites generally move / flow into NNE direction, parallel to the main geological structures in the area and mainly governed by the Nile Deep Sea Fan (NDSF) sediment onload. The tectonic movement of the Messinian evaporites in terms of lateral displacements can be divided into two phases; one prior to the deposition of Nile derived sediments (Netzeband et al., 2006b; Bertoni and Cartwright, 2007) mainly governed by basin subsidence and a second one after the deposition of a pre-kinematic sequence of Plio-Pleistocene deposits (Hübscher and Netzeband, 2007b) and mass waste deposits (Frey-Martinez et al., 2005). Due to the assumed plastic behavior of young evaporite sediments, the basinal Messinian evaporite layer is also called the Mobile Unit (MU) (Hübscher and Netzeband, 2007b). Therefore, we stick to this terminology in the following.

It were Gradmann et al. (2005) who realized that the typical thin-skinned salt tectonic model of Letourzey et al. (1995), which consists of an extensional part at the shelf, a translational part in an intermediate area, and a compressional part in the basin, can be well linked to the case of the Messinian evaporites in the Levantine basin. In the shelf areas complex salt tectonic features, e.g., salt rollers occur. Cartwright and Jackson (2008) formulated schematic models to explain these complicated features in the slope area offshore Israel. They assume an undisturbed base of salt for their models and assume a gravitational disequilibrium as the main reasons for salt roller occurrence.

6.3 Materials and methods

In this paper, we use data sets from different sources. First, the University of Hamburg collected two marine seismic data sets for this study during the RV Meteor cruise M52/2 (GEMME-project) in 2002 and during the RV Pelagia cruise PE228 (SAGA-project) in 2004 (Gradmann et al., 2005; Netzeband et al., 2006b). These data was acquired using a 24-channel streamer of 600m active length, with a group interval of 25m and a shot spacing of 25m. This results in a CMP spacing of 12.5m. Data was recorded up to 5s. All profile locations are displayed in Figure 38(a) on a bathymetric map for the Eastern Mediterranean.

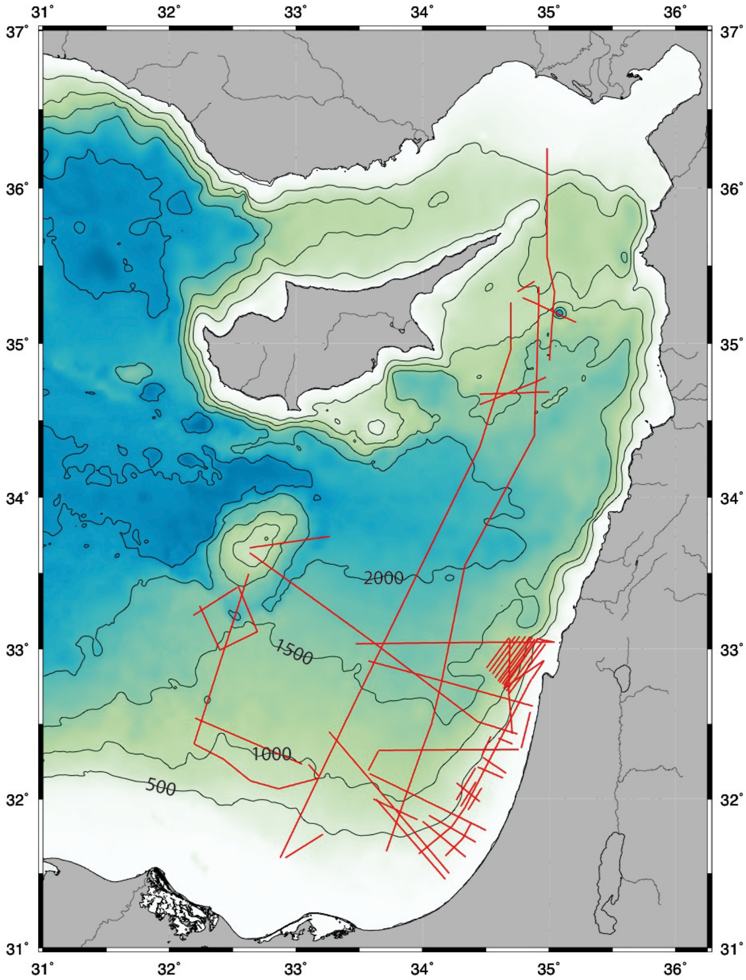

(a)

Figure 38: Working area in the Eastern Mediterranean / Levantine basin. In red the profile lines acquired by the University of Hamburg during the GEMME and SAGA cruises are displayed.

Second, we kindly obtained pre-stack field data of three mainly W-E striking seismic industry data lines. These profiles strike almost perpendicular to the bathymetric contour between 31N and 33N. The data was acquired with a 576-channel, 7175m long streamer, with an initial offset gap of 150m. The shot spacing was 25m and the receiver group interval was 12.5m. This results in 12.5m CMP spacing and a maximum CMP fold of 288 channels. The data is recorded up to 9s. The time isochore maps of the Messinian and Plio-Pleistocene sequences are further based on eight other time-migrated industry seismic data lines.

Besides the seismic data sets, we also had access to satellite gravity data measurements and open domain bathy-metry data sets. Based on these, we generated a basement surface map for the Eastern Mediterranean from 3D gravity inversion modelling, a residual Bouguer anomaly map, and a residual bathymetry map.

6.3.1 Seismic processing The seismic processing work for this study mainly focussed on the processing of the long streamer industry data set. After pre-processing and denoising of the prestack data, different demultiple strategies were applied on the data. This mainly consisted of F-K analysis/filtering, Radon transforms (see for example Ryo (1982)), and an alternative multiple attenuation approach by Dümmong and Gajewski (2008). Following multiple removals, velocity model building was carried out.

Velocity model building in salt bearing basins is a challenging task. Due to the high interval velocity of the salt (> 4 km/s) compared to those of the sediments above and beneath, even relatively small thickness variations of the salt cause velocity pull-downs or pull-ups in the sub-salt domain on the corresponding time sections. Therefore, we had to investigate different migration velocity inversions schemes to obtain the best compromise between efficiency and accuracy (Dümmong et al., 2008). Completing this investigation, we decided to use a special form of traveltime tomography, i.e., Normal Incidence Point (NIP)-wave tomography (Duveneck, 2004c), which additionally to the traveltime also inverts for the first and second order derivatives of the traveltime. This results in a fast and reliable generation of a velocity model. The model is afterwards represented in a smooth way, i.e., by B-spline interpolation, but it can still produce physically correct migration results. Additionally to NIP-wave tomography, a detailed case study with a model based tomography scheme was carried out. Here, a layer stripping approach was followed, where the individual layers inside Messinian evaporites could be resolved in terms of distinct interval velocities.
After velocity model building, prestack Kirchhoff depth migration and a subsequent residual moveout correction followed. Here, the remaining moveout of the depth migrated gathers (Common Image Gathers (CIG)), especially at the top and bottom of the salt reflections, was removed to achieve maximum stacking amplitudes in the corresponding migration result. It is important to note, that the velocity model was not updated simultaneously, only the migration result was enhanced. F-K filtering, muting, denoising, and scaling followed and the final migration results were obtained.

6.3.2 3D gravity inversion In order to derive the basement surface map from the satellite gravity data set, we have used a 3D forward and inversion modelling technique that combines the methodologies of Parker (1972) and Oldenburg (1974). The algorithm implemented in ARKFIELD3D allows the modification of either the physical property (density and/or magnetic susceptibility) or structure of a horizon. The user has full control over the spatial wavelengths inverted for; thereby allowing specific geology to be targeted. It uses an iterative method to calculate layer depths in such a way that the computed potential field response of the final geologic model matches the observed data. The 3D inversion procedure involved two principal stages: (1) construction of an input earth model, including a 3D inversion for deep crustal surfaces, and (2) 3D inversion for the structure of the basement to minimise the difference grid, defined as the difference between the calculated and the observed gravity response. In this case the model was a very simple three layer approach comprised of a body of sea water, a body of sediments and basement. The top basement horizon is the ÒseedÓ horizon, which is modified during the inversion. For this project a flat surface was used as seed basement horizon.

The construction of a 3D model for such a large, geologically complex area as the Eastern Mediterranean would normally be a difficult task, but the lack of constraints from additional data sets and the use of satellite derived gravity data meant that the model had to be a simple one. Of course we did have some control points such as the basement outcrop on Cyprus (where the ophiolite complex generates one of the largest positive gravity anomalies in the entire Mediterranean), but generally this is a poorly constrained model.

Mechanical considerations apply to the behaviour of the 3D inversion. The ARKFIELD3D software uses a layer-cake construction, with physical properties ascribed to the layers defined by input horizons. This is a reasonably sensible approach to modelling in a sedimentary basin environment, but problems can occur where layers intersect, densities are highly variable, or geological horizons have a high fractal dimension. Possible problems result in spiking or aliasing of the horizon or density values, or non-convergence of solutions.

The approach used in the construction of the 3D model was to use the public domain bathymetry data to define the base of the sea water body and below that a flat "seed" horizon was inserted at a depth of approximately 5km. The density assigned to the rocks above this seed horizon was $2.45g/cm^3$ and below the horizon the density assigned was $2.8g/cm^3$. Top basement depths were computed by 3D inversion of the Free Air Gravity for structure at the basement interface. The predicted basement relief was computed by perturbing the surface until the updated forward response of the model closely matched the observed gravity data. The inversion algorithm was used to adjust this surface until the observed and computed responses matched within acceptable limits. The wavelengths are controlled during the inversion, allowing the longer wavelengths (deeper structure) to be targeted first and gradually reducing the wavelengths to target the shallower structures. This is an iterative process with results examined at each stage.

It was understood that the lack of constraints for this model, and the simplicity of the model, meant that the final basement surface derived is certain to contain errors. These errors are likely to be in respect of the absolute depths to the basement surface; however, the relative variations between the "highs" and "lows" on this surface are likely to be more accurate. One of the key results from the final basement surface is the disposition, shape and likely depth of sedimentary basins within the Eastern Mediterranean.

6.3.3 Residual field generation To obtain the residual anomalies maps, additional processing steps have to taken. The observed gravity field include effects from the whole Earth and extra-terrestrial sources. Processing procedures compensate for "whole Earth" effects by removing the standard reference field (1967 International Gravity Formula (Woollard, 1979)). These ambient signals are then subtracted (with other effects) to produce the anomaly fields that form the basis of interpretation. However, these anomaly fields still include contributions from the whole crust and the upper mantle, which together generate a wide range of spatial wavelengths. Although the gravitational or magnetic response of a body is dependent on several factors (including its physical properties, size, shape and depth), we can still suppress contributions from deeper sources by simple high pass filtering. This technique is one of several methods that are used to perform "regional-residual separation", where regional anomalies are taken to be long wavelength contributions from deeper sources that mask shorter wavelength residual contributions from shallower sources (Telford et al., 1982). The terms regional and residual are used in their relative sense only, and must be considered in terms of the scale of the survey.

For this project the residual gravity was generated using a 150km wavelength cut-off filter. The same filtering technique was applied to topography and bathymetry data, and although it removes any elevation value from the data it does provide an excellent "plan view" fabric mapping tool. The residual topography was created using a 50km cut-off filter.

6.4 Results

After processing of the data, the main geological sequences were interpreted on the basis of the three depth migrated industry seismic sections following the sequence stratigraphic framework of Farris and Griffiths (2003) (Figure 37(a)). Sequence ages up to the Jurassic/Triassic have been identified and traced throughout the basin. The detailed structural interpretation is mainly based on the three east west striking prestack depth migrated profiles, each of more than 120km length (Figures 39(a), 40(a), and 41(a)). For the spatial distribution of the sequences, thickness maps of Plio-Pleistocene to Messinian have been generated from all available data. Additionally, the basement and the residual Bouguer bathymetry maps from the satellite gravity data are used to describe the structure of the acoustic basement. In the following, the basin fill stratigraphy based on seismic interpretation will be presented in terms of geological sequences. Secondly, the derived basement morphostructure and plate tectonic implications based on the gravity inversion results will be described.

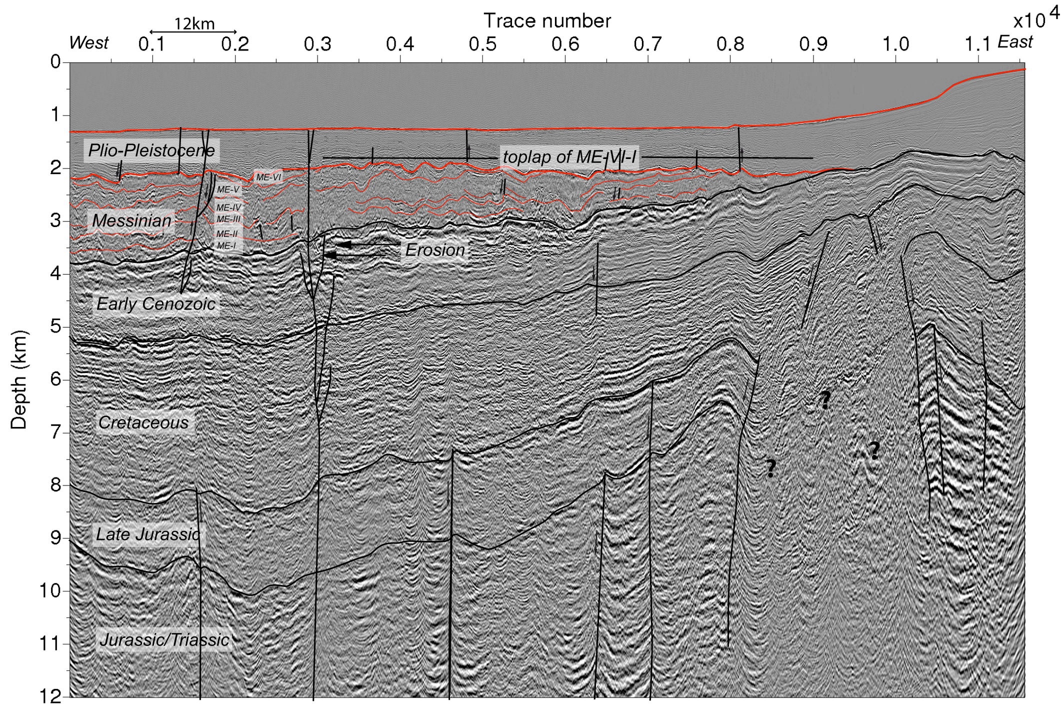

(a)

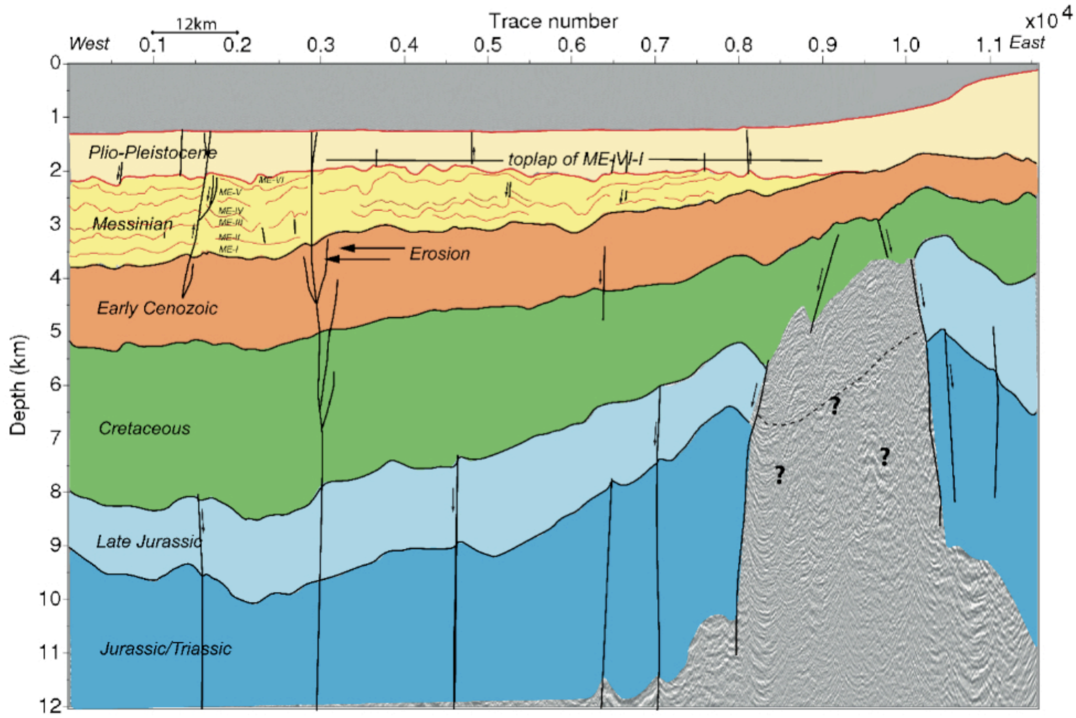

(b)

Figure 39: Depth migrated section (a) and the corresponding linedrawing (b) of profile A ($VE \approx 12$). Structures up to 12km depth could be imaged and interpreted.

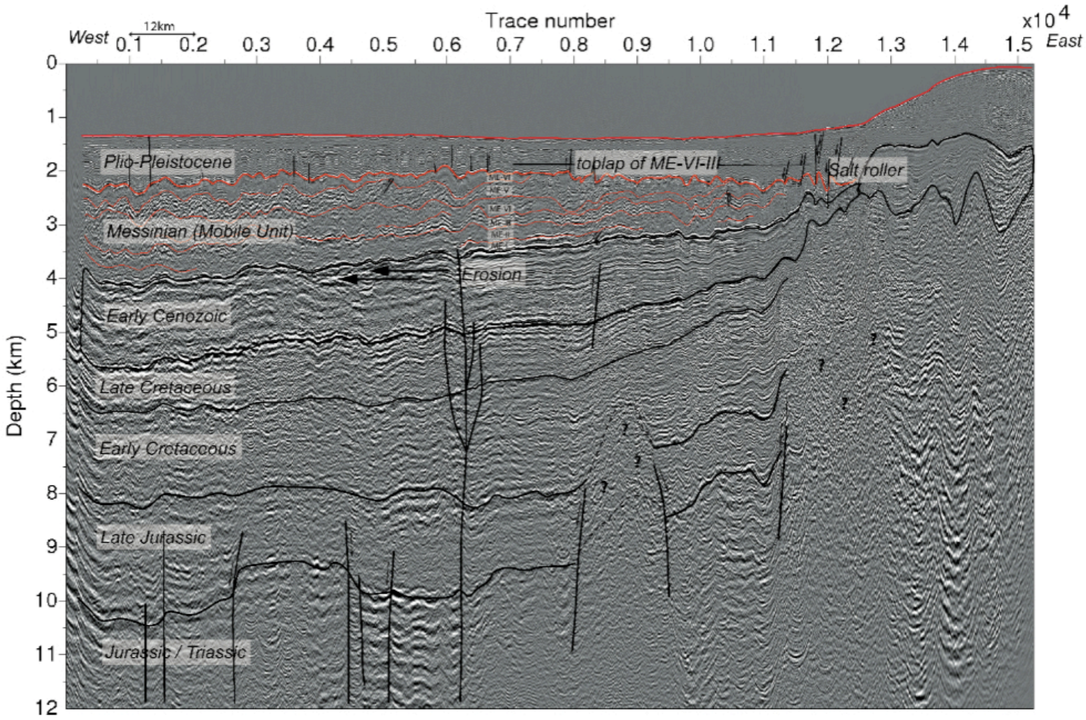

(a)

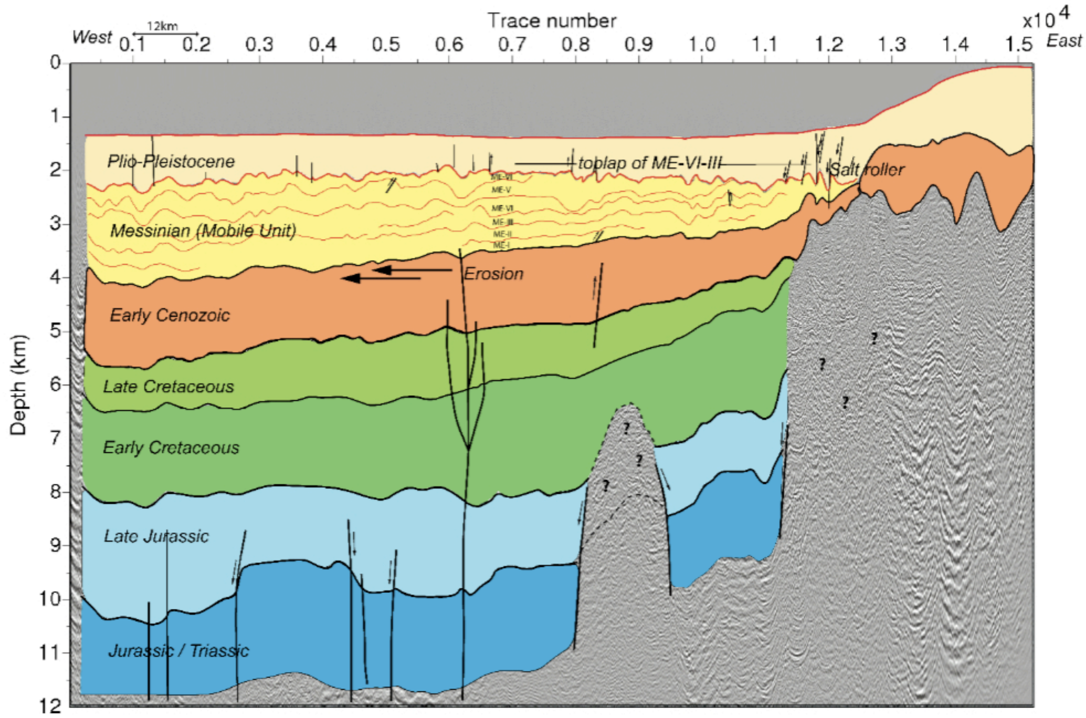

(b)

Figure 40: Depth migrated section (a) and the corresponding linedrawing (b) of profile A ($VE \approx 12$). The youngest sediments visible are assumingly of Jurassic to Triassic age.

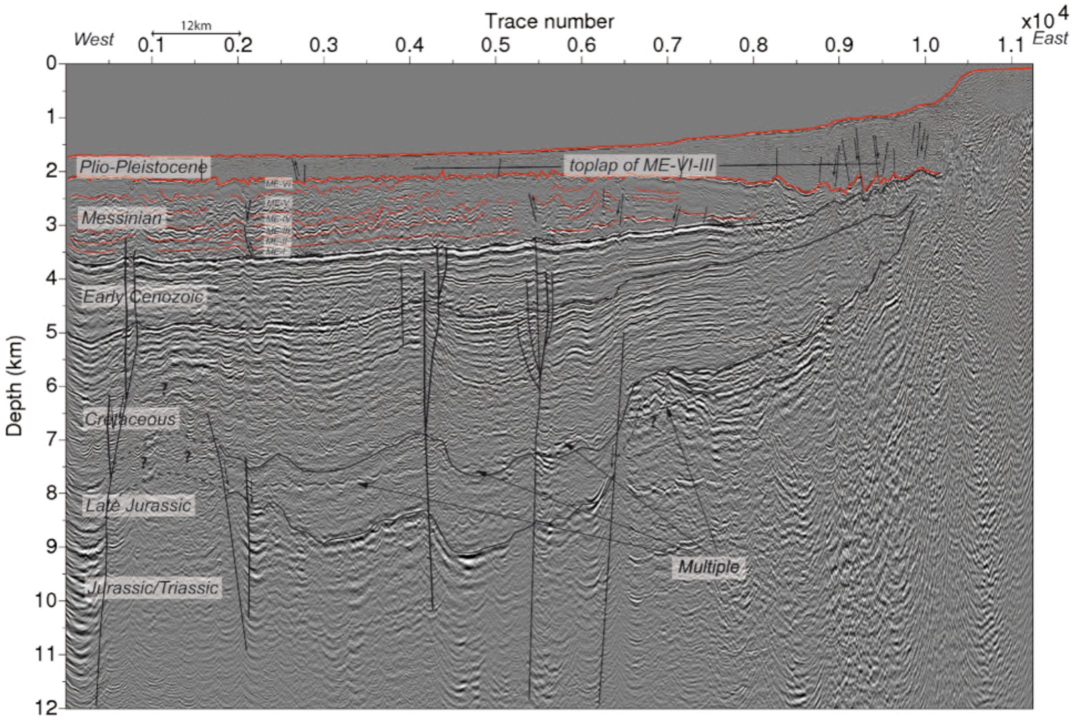

(a)

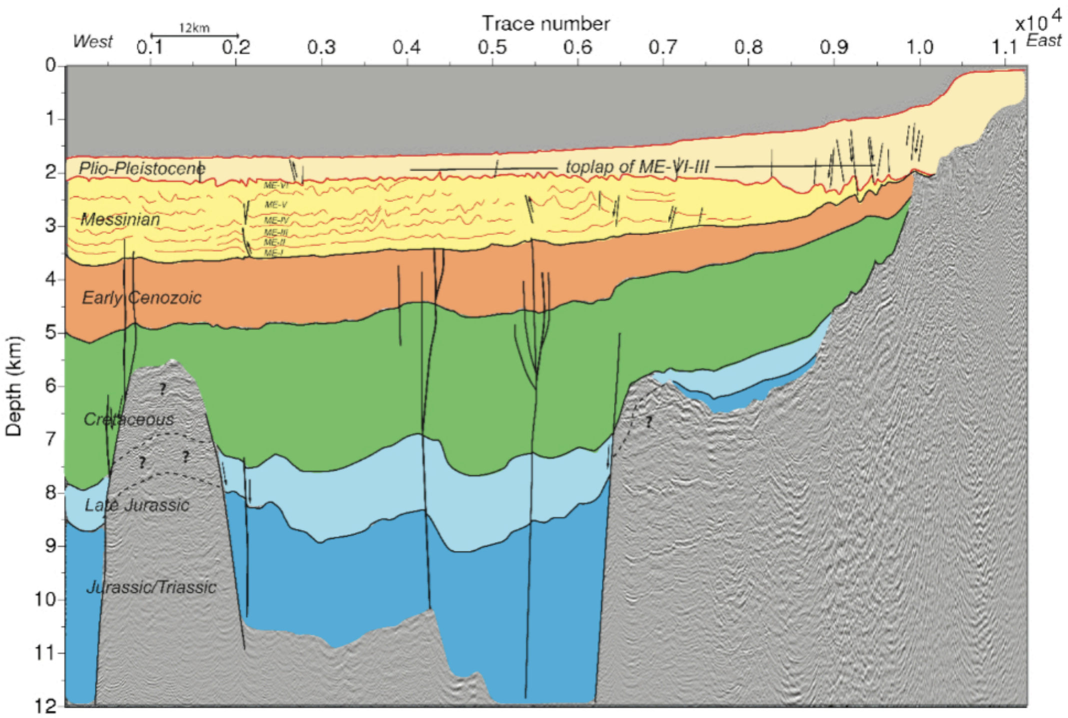

(b)

Figure 41: Depth migrated section (a) and the corresponding linedrawing (b) of profile A ($VE \approx 12$). This profile is located at the northern border of the Levantine basin.

6.4.1 Basin fill stratigraphy and fault pattern

Jurassic/Triassic The deepest visible sequence on the prestack depth migrated profiles is of Jurassic to Triassic age. Only the upper sequence boundary can be identified clearly on all sections (Figures 39(a), 40(a), and 41(a) locations from south to north). The upper sequence boundary descents basinwards from 6-7 km depth beneath the lower slope to more than 10 km depth in the basin (Figure 39(a)). As far as the lower limit of the sequence is visible, the entire succession shows an average thickness of 2 - 3 km. The sequence is laterally disrupted by the up doming Syrian Arc structures (eastern parts of the sections in Figures 39(a), 40(a), and 41(a) between CMP numbers 8000-11000, 11000-14000, and 9000-11000, respectively) and Horst and Graben structures offshore the Levantine coast (middle to western parts in the Figures 39(a), 40(a), and 41(a) between CMP numbers 500-5000, 2500-10000, and 1000-7000, respectively). The Horst and Graben structures generally show a Graben in the middle to western parts of the sections (Figures 39(a), 40(a), and 41(a)) and one Horst next to the up-doming Syrian Arc structures on profiles B and C (Figures 40(a) and 41(a)). On profile C, we also see a Horst following the Graben in westward direction (Figure 41(a) around CMP number 1000 to 2000).
The reflectors of the sequence generally show a defined low frequency content. The average velocity determined for this sequence varies round 5000m/s.

Late Jurassic Late Jurassic sediments can be found on all depth migrated sections. The sequence can be traced from depth of 5.5km at the shelf and from 8.5km depth in the basin. The thickness is more or less constant over all sections and shows values of about 2km (see Figure 39(a), 40(a), and 41(a)). The layer is discontinuous, interrupted by the up doming Syrian Arc structures (eastern parts of the sections, under the continental shelf; Figures 39(a), 40(a), and 41(a)) resulting in normal faults. In addition to this, the Horst and Graben structures as well disturb the sequence (middle to western parts of the profiles; Figure 39(a), 40(a), and 41(a)). The sequence follows the predefined basement structures.
The reflectors also show reduced frequency content compared to the layers above and are also often affected by processing artifacts. Nevertheless, the reflector pattern seems to be more or less parallel. Velocities determined for this layer show maximum values of about 4500m/s to 5000m/s.

Cretaceous The Cretaceous sediments can be found on all three depth migrated sections (Figures 39(a), 40(a), and 41(a)). Thicknesses are ranging from 2.5km in the basin to about 1km at the shelf area on profile A (Figure 39(a)). The sequence appears in a depth of 3.5km to 5.5km. In general, the thickness of the layer reduces towards the shelf. On profiles B and C, the sequence cannot be traced over the whole section, because of disturbances of the up-doming Syrian Arc fold belt or the Horst and Graben basement structures (Figures 40(a) and 41(a)). On profile A, the Cretaceous can be differentiated in the late and early Cretaceous (Figure 39(a)). The Late Cretaceous is considerably smaller in thickness (about 1km smaller) than the Early one. However, due to the weak velocity contrast between these two layers and the bad amplitude behavior on the two northern profiles, it is hard to discriminate between the Early and Late Cretaceous. Thus, we will stick in the following to the Cretaceous as one sequence. The base of the sequence follows the predefined basement structures, in contrast to that the top does not. The influence of the Syrian Arc as wells as the Horst and Graben structures is reduced. The velocities obtained from the NIP-wave tomography measurements range from 3500m/s up 4000m/s.

Early Cenozoic The Early Cenozoic sediments form a more or less constant thick sequence (Figures 39(a), 40(a), and 41(a)). It can be found in depth from 4km to 4.5km and shows a thickness of about 2km. On profile B the Early Cenozoic cannot be traced over the whole section (Figure 41(a), between CMP number 10000-11000), whereas on profiles A and B the sequence is forming a more or less constant layer over the whole section (Figures 39(a) and 40(a)). The layer consist of a parallel to sub-parallel reflector pattern. The amplitudes are decreasing within the layer due to artifacts of the multiple attenuation algorithms. The base of the Early Cenozoic is formed by an unconformity with the Cretaceous. The top of the sequence is represented by a partly erosional unconformity with the base of the evaporites (Bertoni and Cartwright (2006); see Figure 42(a) between CMP number 3000-6000), which can be found on the profiles A and B. In contrast to that we observe on profile C a conformity of the pre-Messinian and the evaporites. The sequence follows the structure of the Cretaceous sequence beneath, slightly lifted from the Syrian Arc structures near the shelf. The determined velocity of the Early Cenozoic unit is considerably less (about 700m/s) than the velocity of the MU above, which demonstrates the challenges of imaging subsalt structures. Mainly velocities of 3200 m/s to 3700 m/s could be determined.

Messinian (MU) The MU can be clearly identified on all three depth migrated seismic profiles (Figures 39(a), 40(a), and 41(a)). It can be found in a depth of 2km up to a maximum depth of about 4km. On all profiles the Messinian sequence is gaining thickness towards the basin and getting thinner towards the basin margins. At the continental shelf the unit terminates; on profile A around CMP number 9000, on profile B around CMP number 12500, and on profile C around CMP number 9500. In the basin the top of the MU is quite rough and several times disturbed, whereas the base of the evaporites is quite smooth, only small undulations occur.
The spatial thickness distribution of the Messinian Evaporites can be observed from the interpretation of the available seismic data and is displayed in Figure 43(a). We observe that the MU gains significantly thickness towards the NE (33.5-34.5E and 33-34N). We also observe, that minimum thickness of the evaporites quite accurate follows the coastal line of the Levantine, maximum thickness of the salt body occurs in the central part of the basin and minimum thickness occurs in the marginal parts of the basin. In comparison with Figure 45(a), we can also observe that minimum thicknesses of the evaporites correspond to maximum thickness of the Plio-Pleistocene sequence above.
Towards the east under the continental shelf, the top and the base of the evaporite body converge. Here, the uplifted Syrian-Arc fold belt defines the limit of the spatial distribution towards the east (Bertoni and Cartwright, 2006). The base and top of the MU converge and a direct conformity between the Plio-Pleistocene and the Early Cenozoic is formed. On profiles B and C triangular structures formed in the shelf regions, where the top and bottom reflector of the MU converge. These structures are called salt rollers and are recently discussed in the works of Gradmann et al. (2005); Netzeband et al. (2006b); Cartwright and Jackson (2008). We cannot observe salt rollers on the southern most profile A. In Figure 44(a), we display an exemplary part of profile B, where the base and the top of the salt form the so-called salt rollers. We see that a lot of extensional faults occur on top of the MU. Most of them originate at the top or within the MU, but some faults are also affecting the base of the MU. Additionally to the depth migrated section, we plotted an unmigrated stacked section in the image. Here, we see distinct diffraction events originating at the base of the salt, which supports the previous observation.
The overall velocity distribution from NIP-wave tomography ranges from values of 3900m/s to values of 4200m/s.

Plio-Pleistocene The Plio-Pleistocene is the uppermost sequence on all profiles. It can be found in depth ranging from several hundred meters at the shelf to about 1.5km depth in the basin. The thickness varies from about 1km in the basin to about 2km at the eastern shelf and to about 3km at the southern shelf (Figures 39(a), 40(a), and 41(a)). The upper sequence boundary is the ocean floor. The lower sequence boundary is partly unconformity surface, which in the basin is overlying the Messinian evaporites and on the shelf overlies the Early Cenozoic (Almagor, 1984). The layer mainly consists of parallel and sub-parallel reflectors, which are disturbed several times (e.g., Figure 41(a)). The reflectors are generally following the shape of the top of the MU. High amplitude areas are changing with low amplitude areas.
The spatial distribution of the thickness of the Plio-Pleistocene sequence, derived from our data for the whole Levantine Basin, can be seen in Figure 45(a). It can be clearly observed how the sequence gains considerable thickness towards the eastern shelf, as well as to the southern shelf, where the NDSF is formed by the high sedimentation rate from the Nile river (e.g., Mart and Bengai (1982)). In westward direction sediment thicknesses are rising again in the area of the Eratosthenes seamount. In general the sequence gains thickness towards the shelf (see Figure 45(a)).

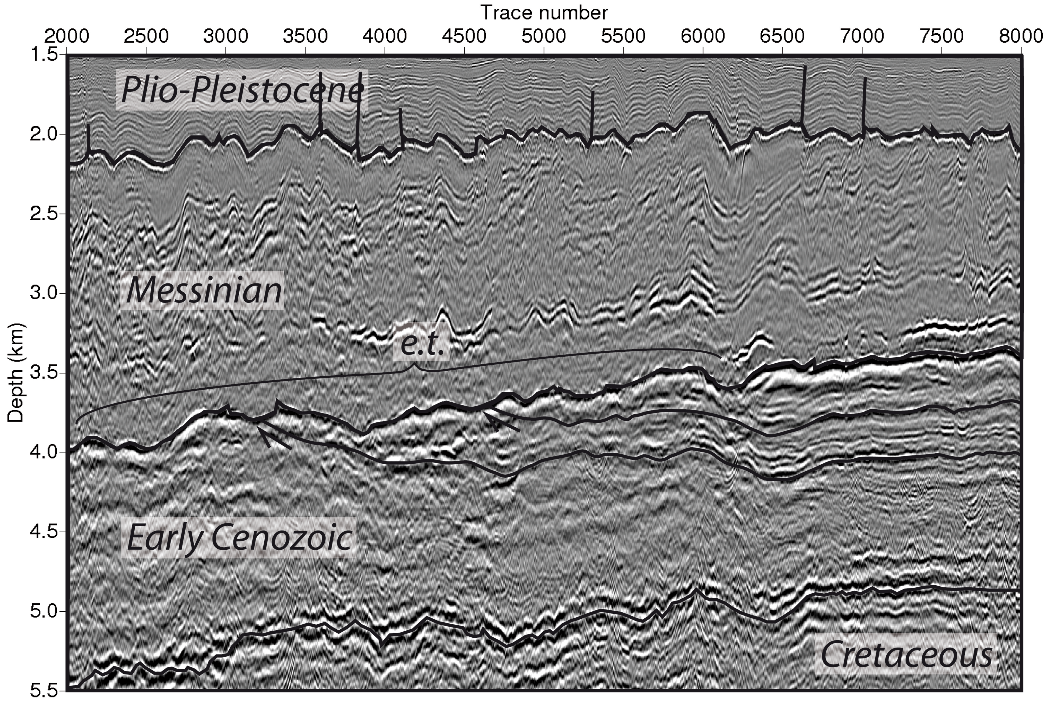

(a)

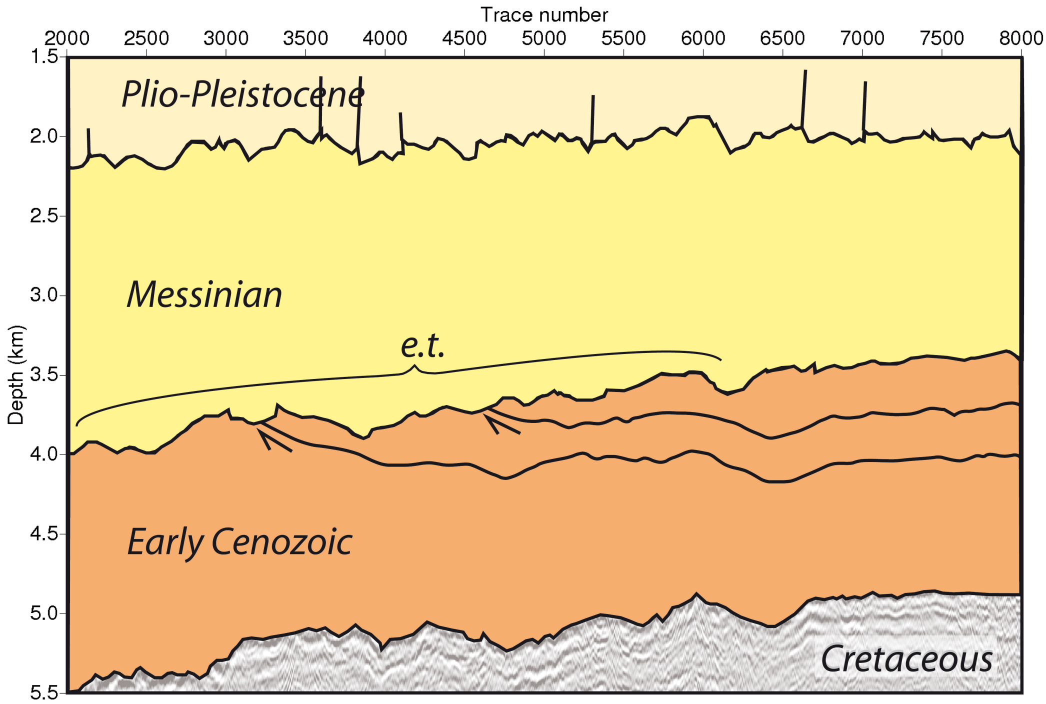

(b)

Figure 42: On profile B the Early Cenozoic forms an erosional unconformity (e.t.=erosional truncation) with the Messinian sequence above ($VE \approx 18$). This feature is not consistent throughout the basin.

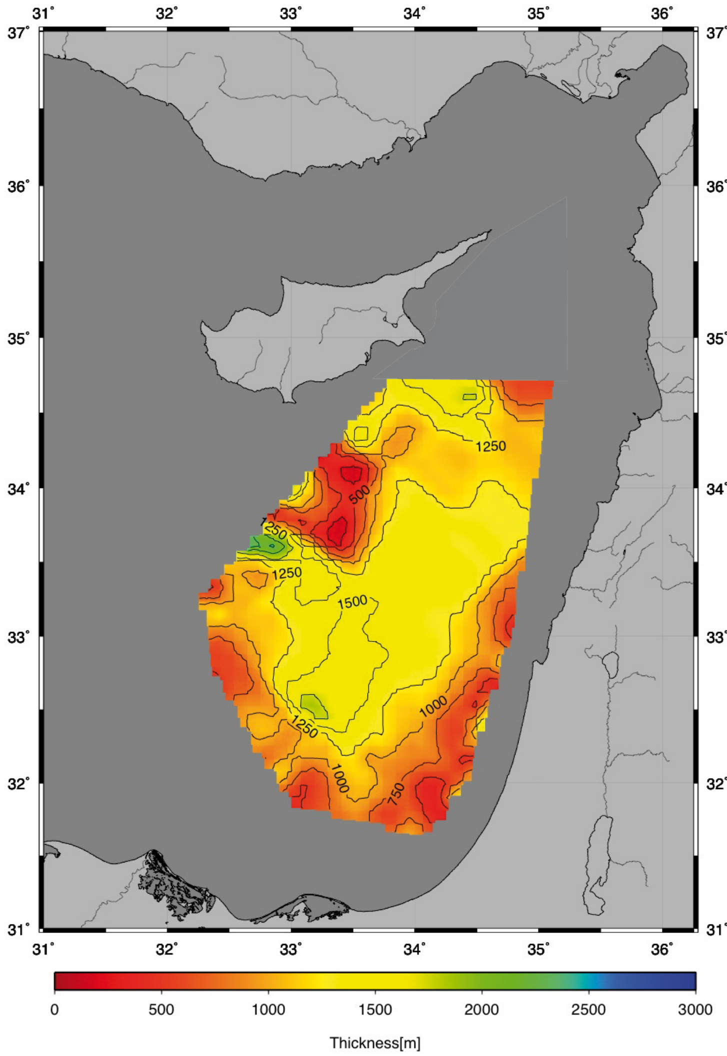

(a)

Figure 43: Spatial thickness distribution of the MU in the Levantine basin. Thickness maximums can be observed around 32.5 deg N and 33 deg E. The contour lines are elongated in NNE direction.

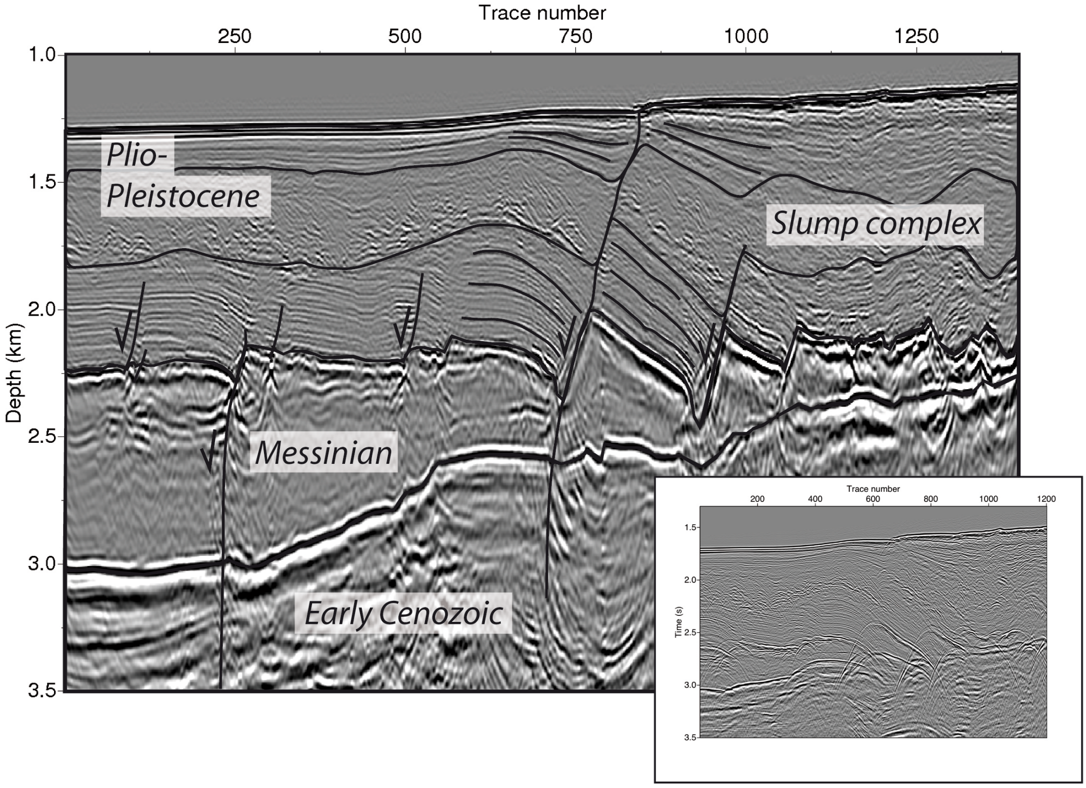

(a)

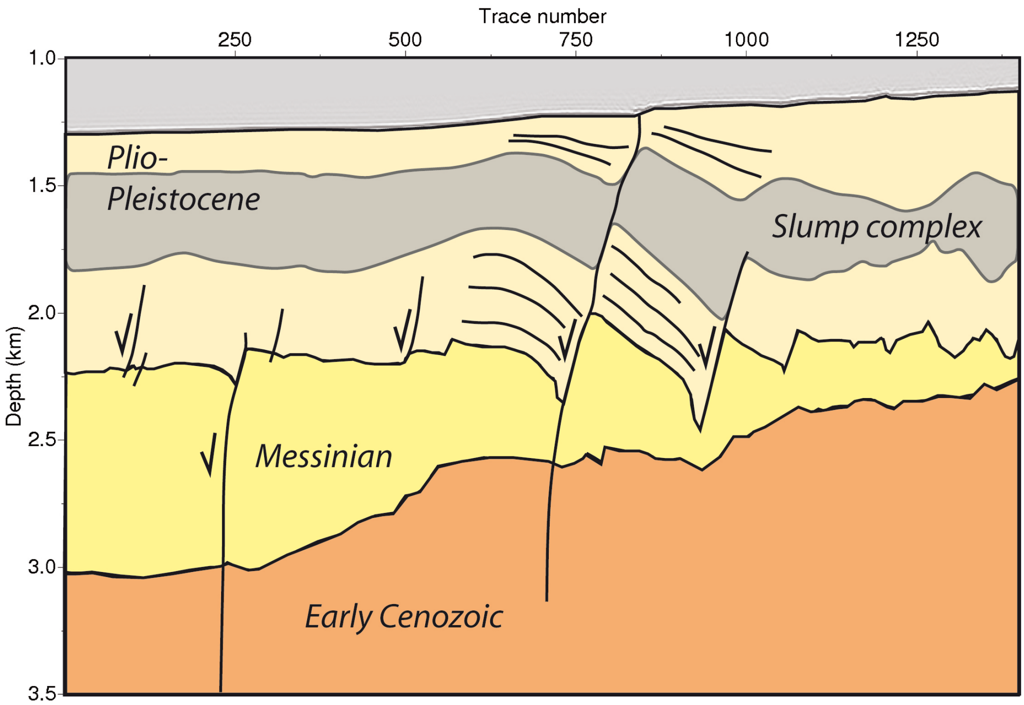

(b)

Figure 44: Salt roller structures on profile B ($VE \approx 7$). Depp rooted faults seem to affect the base of the MU, also clearly visible on the small unmigrated section, where diffraction hyperbolas can be observed at the base of the MU.

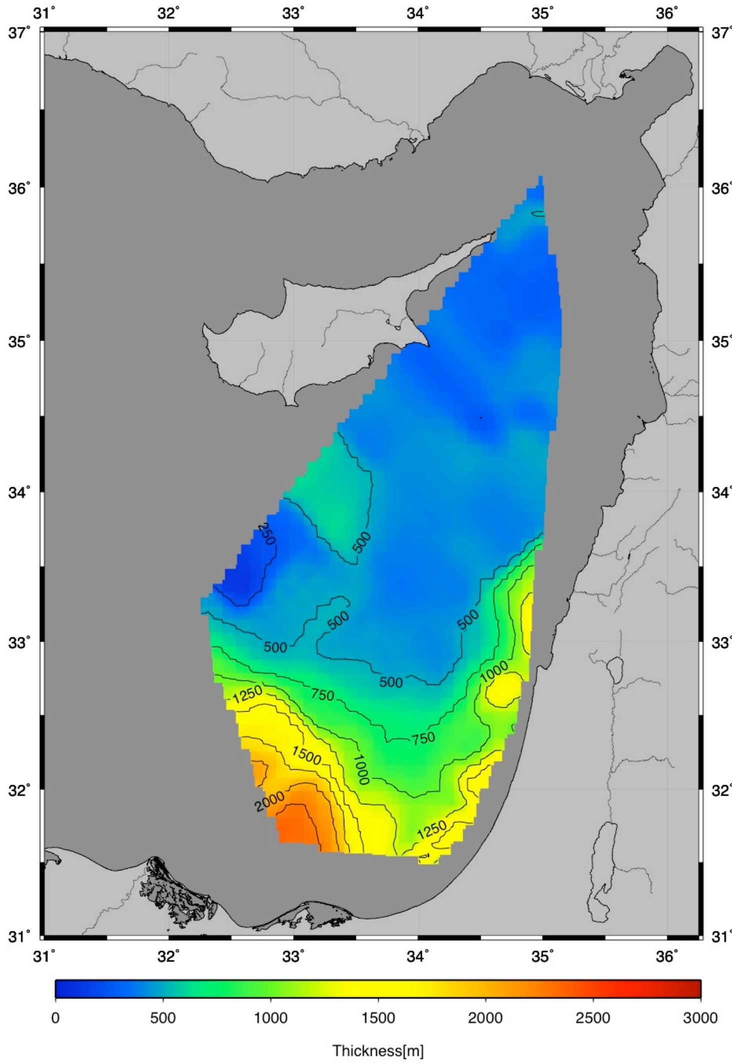

(a)

Figure 45: Spatial thickness distribution of the Plio-Pleistocene sequence in the working area. Maximum thicknesses occur in the south next to the NDSF.

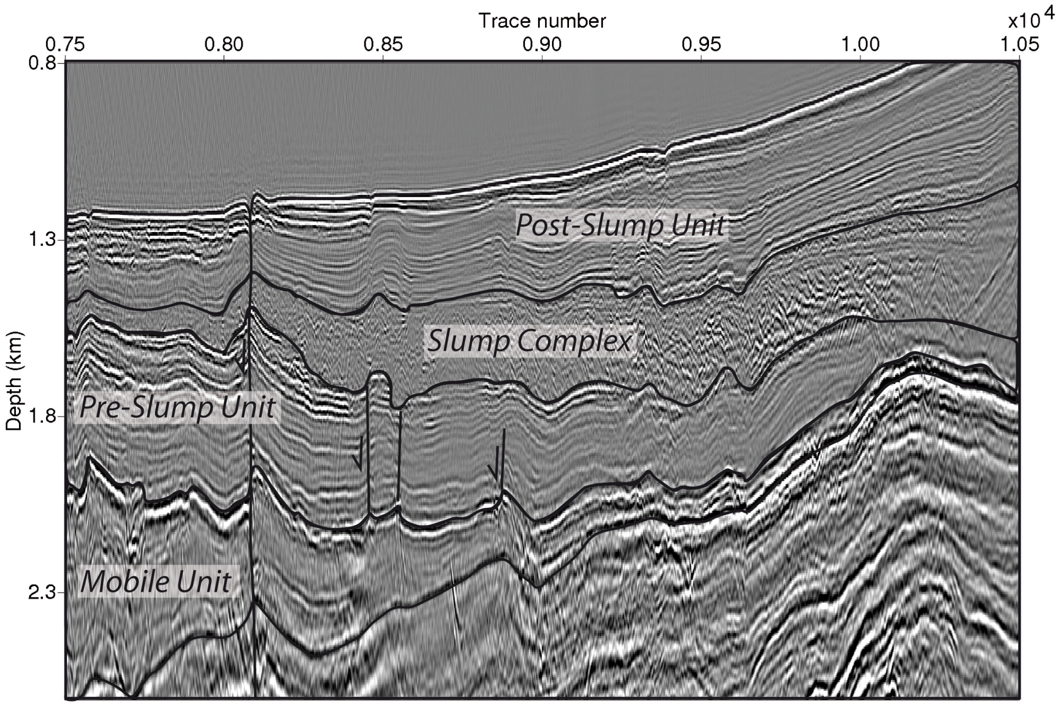

(a)

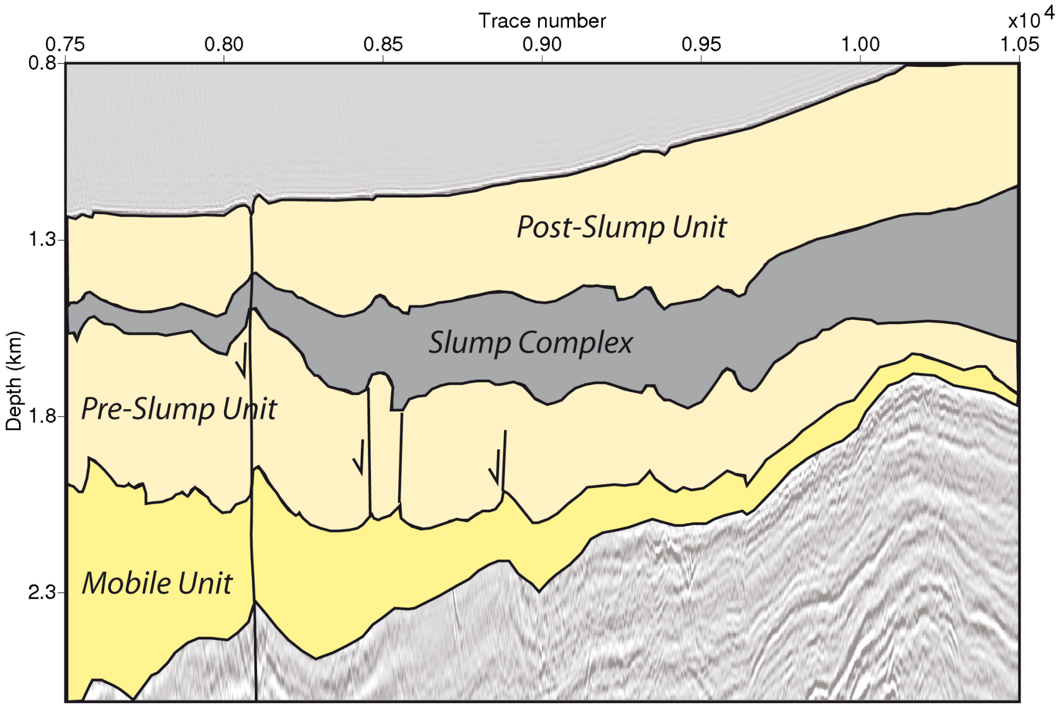

(b)

Figure 46: Slump complex in a marginal part of profile A ($VE \approx 5$). The section can be divided in a Pre- and Post-slump sequence. It can also be seen that the MU heavily influences the geometry of the overburden.

Next to the shelf, chaotic reflector patterns can be observed, which do overlay parallel layers (see Figure 46(a) in depth between 1.3km and 1.8km, for an example on profile A). This chaotic reflector pattern has a greater extend towards the west on the southern profiles. It also gains thickness towards to the south over all three prestack depth migrated profiles (compare Figure 39(a), 40(a), and 41(a)). This chaotic reflector complex reaches thicknesses of 250m at the shelf and thins out towards the basin. We can also observe an erosional surface at the base of this complex (Figure 46(a), between CMP number 9000-9700, in depth of 2.0km).
The obtained velocities for the Plio-Pleistocene sequence range from 1500 m/s for the uppermost deposits up to approximately 2500 m/s for the deposits at the base of the sequence.

Fault structures in the stratigraphic model In the deeper parts of the sections, we mainly see that the Jurassic / Triassic to Late Jurassic sequences are affected by normal faulting caused by the Horst and Graben structures and the Syrian Arc fold belt (Figures 39(a), 40(a), and 41(a) in depth greater than 7-9km). Many faults originating in the acoustic basement seem to affect the sediments up to Late Jurassic age on profiles A and B (Figures 39(a) and 40(a)). Only on profile C the Late Jurassic seems to be quite undisturbed by these faults (Figure 41(a)).
In addition to these faults, we also observe large deep rooted faults also originating in the acoustic basement, but propagating up to the MU or to the overburden sediments (e.g., Figure 40(a) around CMP number 6000). Many of these faults are broken in branches, and form so-called flower structures. One of these fault structures in the western part of profile A affects all units above the Jurassic / Triassic and propagates to the ocean floor (Figure 39(a) around CMP 3000). This fault system can be correlated with other deep rooted fault systems on the northern profiles (Figures 40(a) and 41(a), CMP numbers 6000 and 5500). However, on these two profiles the fault seems not to propagate through the Messinian evaporites. In Figure 47(a), an exemplary flower structure from this fault system on profile B can is displayed. On the northern profiles, this fault structure does not propagate through the whole MU, only the lower part is affected. The entire fault system follows quite accurate an anomaly on the residual bathymetry map in Figure 54(a).

Additional to the deep rooted fault structures, we also observe thin skinned tectonic features, that are originating in the MU or just on top of the MU. In the basin the top of the Messinian evaporites is quite rough and deformed by tectonic processes. Several thrust faults are visible, which heavily affect the overburden sediments. Steep dipping thrust angles can be observed at the top of the MU (Figure 48(a), CMP number 2600-2700). Most of the Plio-Pleistocene sequence is faulted and folded according to the shape of the top of the Messinian (see Figures 39(a), 40(a), and 41(a)). On most of the profiles the uppermost part of the Plio-Pleistocene is undisturbed. Only in some location the whole sequence is affected.
At the shelf, we mainly observe normal and listric faults (Figures 40(a) and 41(a)), which originate on top or within the MU and disturb the Plio-Pleistocene. However, some faults also originate from structures below the Messinian, but cannot be traced to the acoustic basement. Most of these faults occur where the underlying Messinian thins out and decreases to a thickness of less than 1km. Most of the normal faults terminate at the ocean floor and have to be considered as active.

6.4.2 Stratigraphy of the Messinian evaporites Throughout the basin, internal MU sequences (ME-I - ME-VI) can be identified (see Figure 39(a), 40(a), and 41(a) and for a detailed view Figure 48(a)). The internal reflectors are varying in the seismic facies from low reflective (ME-I, ME-II, ME-IV, and ME-VI) to high reflective (ME-III and ME-VI). In the western parts of all sections, the internal reflectors form sequences of more or less constant thickness; all internal sequences are present (see Figure 48(a)). Over the whole basin they are folded and faulted independently, whereas the high reflective layers are folded heavier, than the low reflective layers (Figure 48(a)). We hardly see any faults in the MU affecting only single sequences on the northern profiles. In contrast to that, we see faults disturbing single MU sequences on the southern profile A. However, mainly folds are dominating inside the salt body.

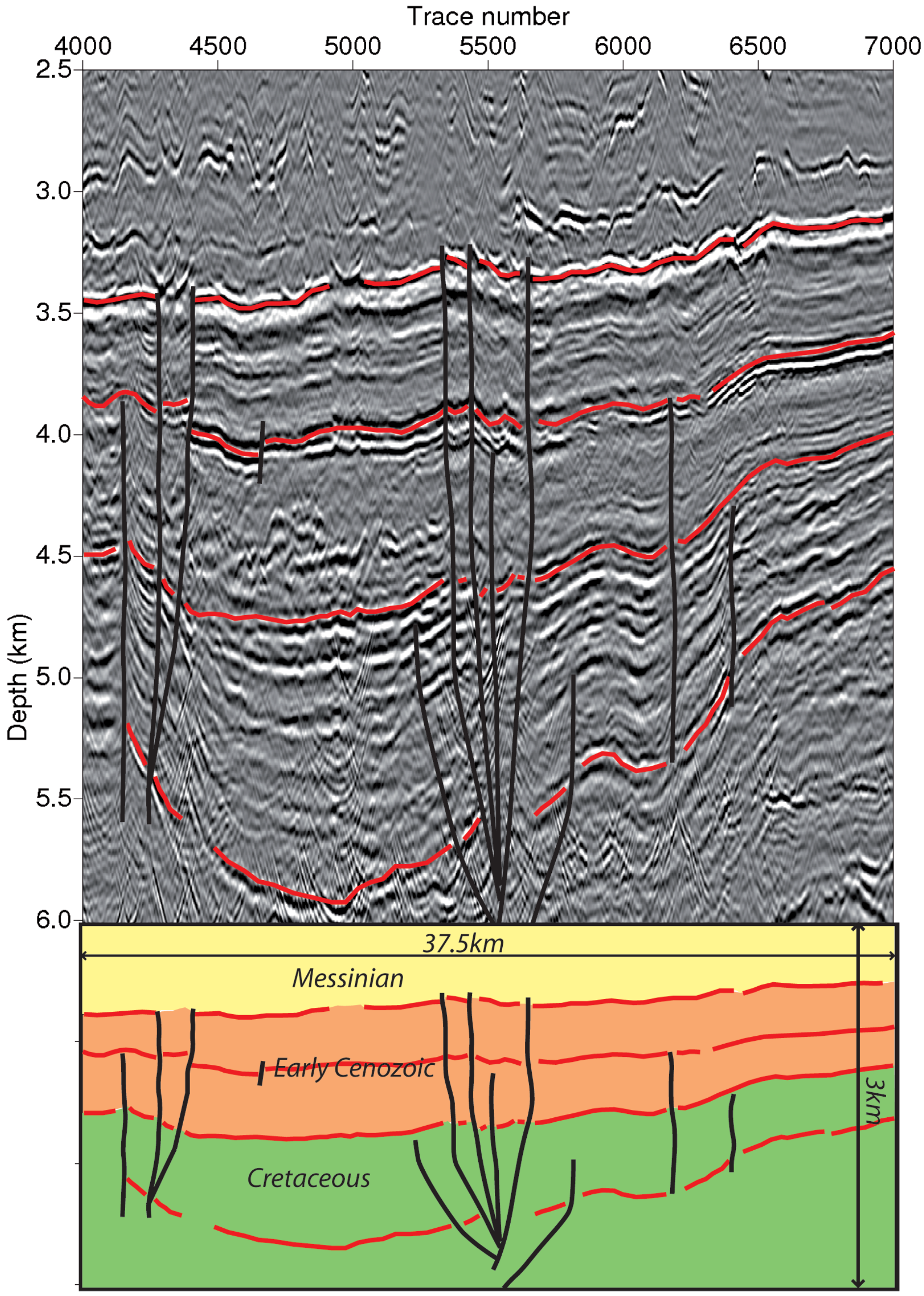

(a)

Figure 47: On profile C a large flower structure can be observed, which spatially well correlates with the Damietta-Latakia line ($VE \approx 12.5$). Here, only the first layers of the MU are affected by faulting processes.

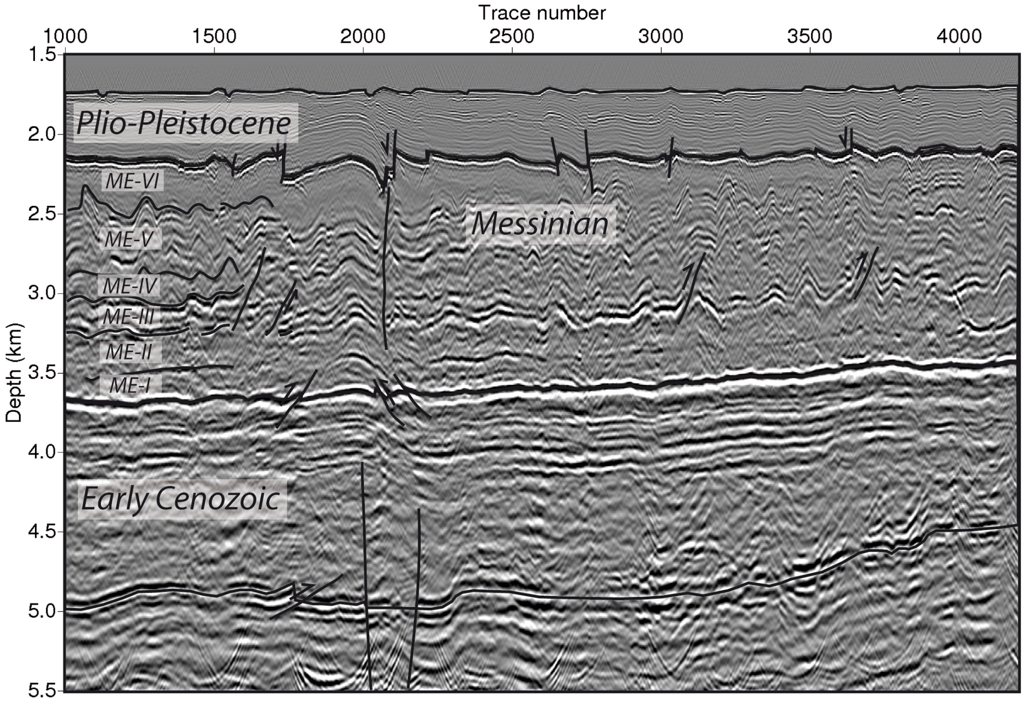

(a)

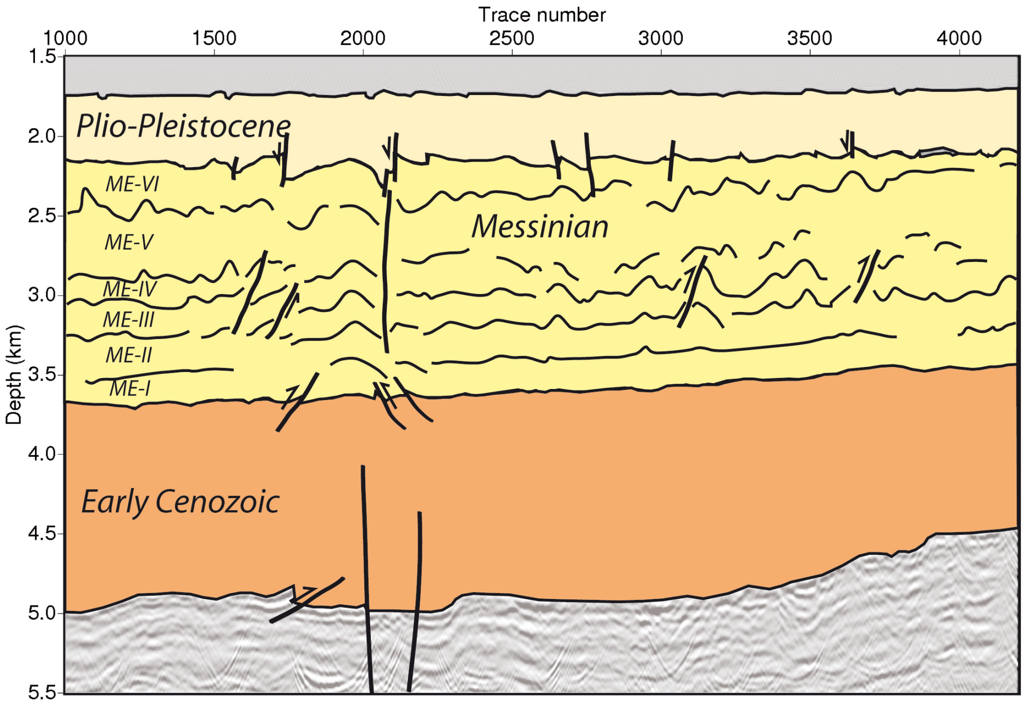

(b)

Figure 48: Exemplary part of the deep basin structure of the MU located on profile C ($VE \approx 3$). In the basin all six internal MU sequences are present.

In Figure 49(a), we displayed that ME-VI-III terminate against the top of the evaporites in eastward direction. On the southern profile A all internal sequences toplap against the base of the supra-salt deposits, whereas on the northern profile C sequences ME-VI to ME-III are forming a toplap. We also observe in Figure 49(a) that the deformation pattern at the top of the salt body varies according to the layer at the top of the MU. The high reflective layers form a rough surface, whereas the low reflective layers form a smoother top.
The thickness of the individual sequences varies across the Levantine basin. In general the thickness decreases towards the shelf, corresponding to the toplap configurations. In Figure 50(a), we illustrate the spatial thickness distribution of the internal sequences. We see that ME-VI and ME-V are only present south of 33 deg N, i.e., in the basin centre, whereas the other units are represented in the whole basin. All sequences terminate parallel to the Levantine coastline, due to the toplap termination of the individual sequences. Consequently, ME-VI and ME-V are decreasing in thickness towards the East and show maximum thickness values of about 400 to 600m in the central parts of the Levantine basin. ME-IV shows some defined local thickness maximums of 350m (33 deg N, 34 deg E), but in general a thickness of about 150m. ME-III quite well corresponds to a syncline structure in ME-II, with a thickness maximum of 400m. In the other parts of the sequence the layer has a thickness of 200m and increases towards the coast. ME-II forms a layer of more or less 300m, but has a defined thickness reduction in the central part of the basin (33.5 deg N, 34 deg E), where the sequence reduces to 100m. ME-I forms a more or less constant layer of approximately 200m in the basin. The described thickness undulations for ME-III and ME-II mainly occur in a NW prolongation of the Carmel fault.

To obtain a more detailed velocity description for the Messinian evaporites, especially for every identified internal reflector, we performed a detailed study on a reprehensive part in a central part of the Levantine Basin, where all six intra-evaporitic sequences (ME-I to ME-VI) are present (Figure 51(a)). We investigated the interval velocities for the individual salt layers with the help of a layer stripping tomographic approach (Beitz, 2008). The individual layers of the MU and the overburden where picked and the velocities of the sequences, where inverted from top to bottom. It could be observed that velocities are changing according to the stratigraphy inside the MU, i.e., ME-I to ME-VI. The velocities distribution is 4210m/s to 4270m/s for ME-VI, 3800m/s to 3830m/s for ME-V, 4190m/s to 4250 for ME-IV and ME-III, and about 3900m/s to 4010m/s for ME-II and ME-I. The high reflective sequences show in general lower velocities than the low reflective transparent sequences.

6.4.3 Basement morphostructure and plate tectonics The residual Bouguer gravity map for the Easter Mediterranean reveals maximum anomalies of 10 to 15mgal, where-as the minimum values are in the range of -20mgal (Figure 52(a)). We mainly observe NNE-SSW striking features, but also some clear evidences for NW-SE striking positive anomalies. The latter ones are mainly occurring in two places, one south of 32 deg N running parallel to the coastline of Egypt, which can be correlated to the Bardawil line, and the second running from south of the Cyprus trench to the Carmel fault. This positive anomaly will be called the Cyprus Carmel fault (CCF) in the following.

The NNE-SSW striking anomalies show as well positive characters, but also clear negative values. We see a large positive anomaly following quite accurate the coastline of the Levantine, which can be linked with the Syrian Arc fold belt. Following this positive anomaly in eastern direction, we see a distinct change between positive and negative anomalies until the postulated position of the Baltim-Hecateus line and the following Eratosthenes seamount. North of the CCF, the orientation of the NNE-SSW striking anomalies slightly changes in N-S striking direction, whereas it changes again north of 34 deg N to the original trend of mainly NNE-SSW.

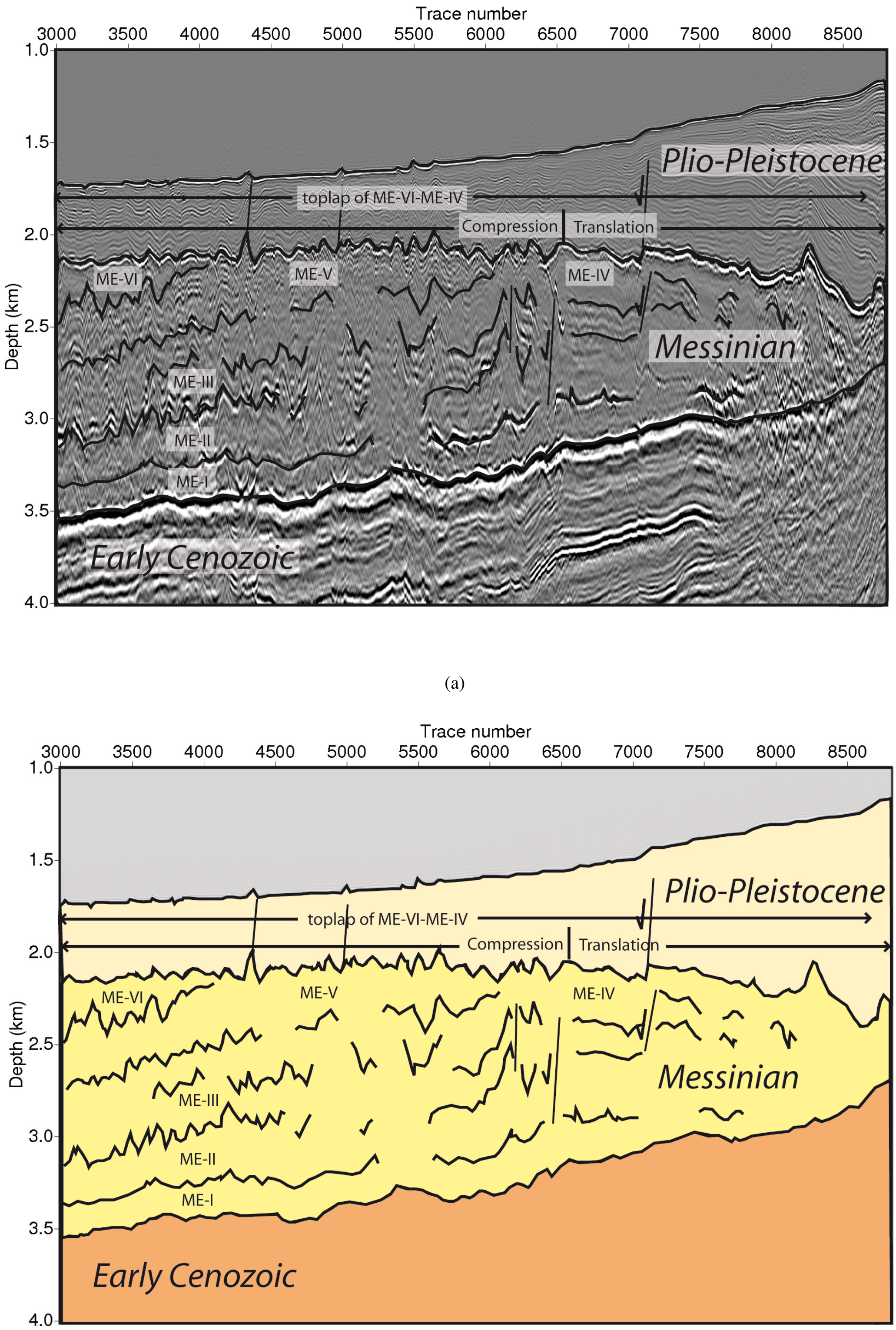

(a)

(b)

Figure 49: Toplap of the internal MU sequences on profile C ($VE \approx 6$). Prograding to the shelf ME-VI to ME-IV are forming a toplap against the top of MU. The section can be divided in a compressional regime in the basin and a translation regime next to the shelf (after Vendeville, 1999). Additionally, the corresponding MU sequence at the top forms depending on its reflectivity a rougher or a smoother surface.

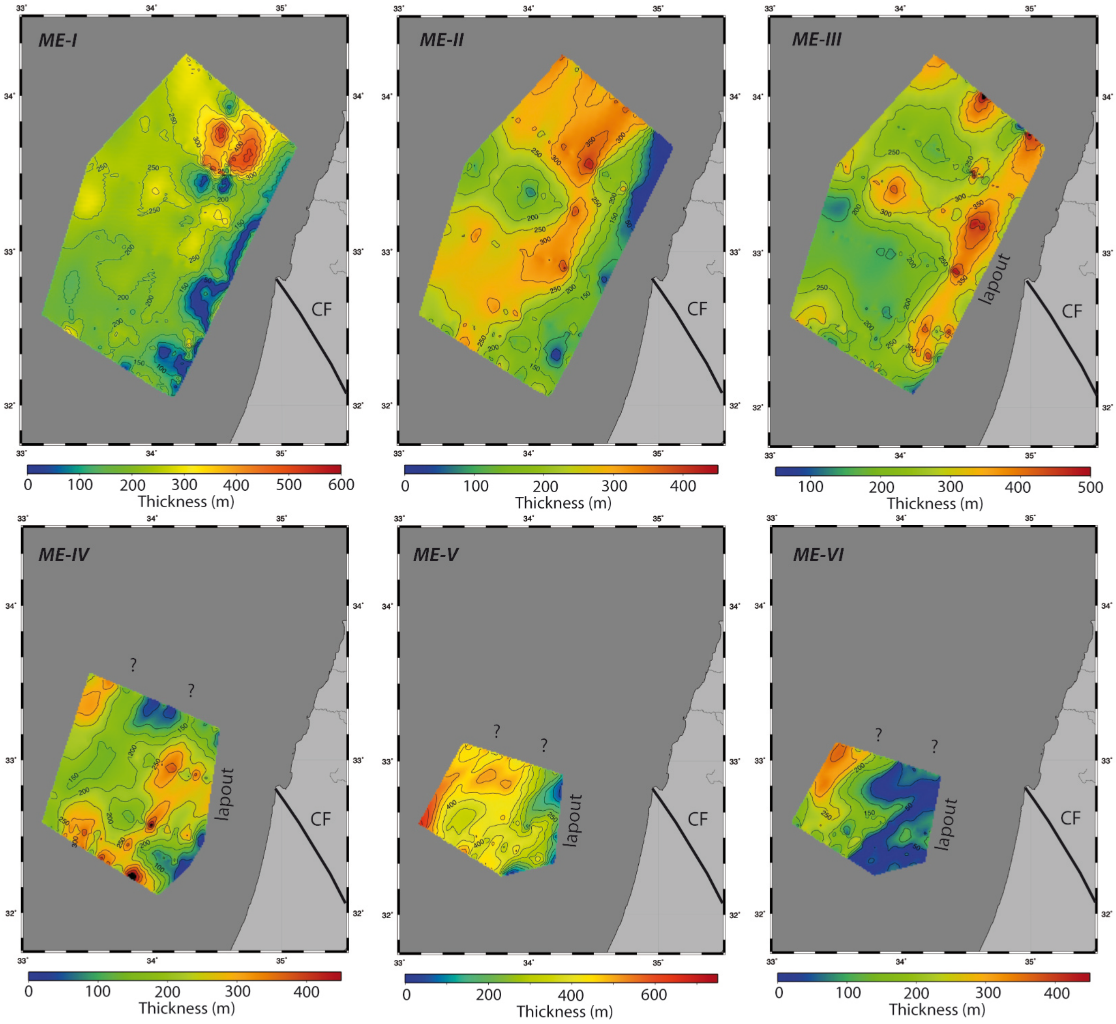

(a)

Figure 50: Spatial thickness distribution of all internal MU sequences (ME-I to ME-VI). Sequences ME-IV to ME-VI cannot be traces throughout the basin (indicated by ?). The sequences form a toplap against the top of the MU in eastward direction. Additionally, we see thickness undulations in the direction prolongation of the Carmel fault, vertically correlating with the CCF.

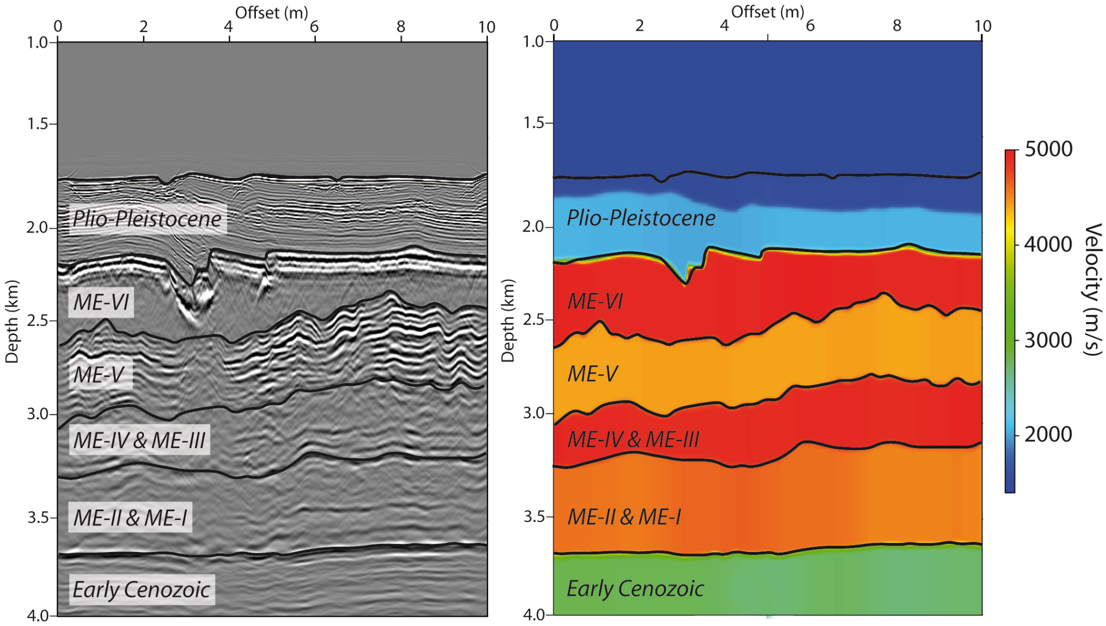

(a)

Figure 51: Detailed velocity distribution in the central part of the basin, where hardly tectonic overprint is present. Transparent sequences show general higher velocities (ME-VI, ME-IV, and ME-III) than high reflective sequences (ME-V, ME-II, and ME-I).

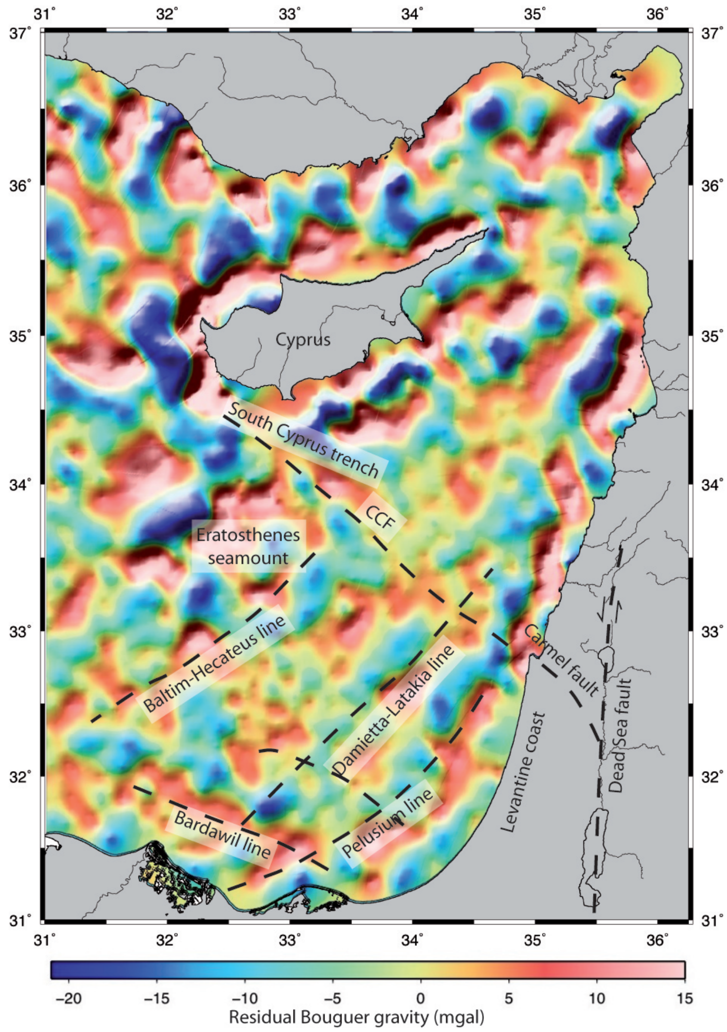

(a)

Figure 52: Residual Bouguer anomaly map for the Eastern Mediterranean. Offshore the Levantine coast mainly Horst and Graben structures are indicated by the gravity anomalies. Almost all strctures in the Levantine basin follow a general NNE trend.

The dominating trend in the calculated basement morphostructure map is also mainly NNE-SSW (Figure 53(a)), but the two major NW-SE striking elements are also visible. We observe maximum depth of approximately 15km in the Cyprus trench and at the northern and southern margins of the Eastern Mediterranean. Minimum basement depths of a few km can be found around Cyprus, at the Eratosthenes seamount, as well as in the Herodotus basin. Southwest of the Eratosthenes seamount, we observe a direct structural link between the Herodotus basin and the Eratosthenes seamount.

The main two NW-SE running features, the CCF and the Bardawil line, are clearly visible as basement highs. South of the CCF running parallel to the Levantine coastline in mainly NNE-SSW direction, we see a basement high, which corresponds to the Syrian Arc structures. Further to the west, we see the distinct change from basement highs and lows. North of the CCF, the striking direction of the Horst and Graben structures changes (Figure 53(a)). South of it, the striking direction is mainly NE-SE and therewith parallel to the Cretaceous to Eocene Syrian Arc structures but angular to the Neogene Dead Sea Transform. Directly north of the CCF, the striking direction changes to NNE-SSW, which is parallel to the Yamouneh fault. At 34 deg north the striking is almost N-S and therewith parallel to the Ghab fault and Roum fault, respectively. Further north the striking direction again changes back to the original NNE-SSW trend.

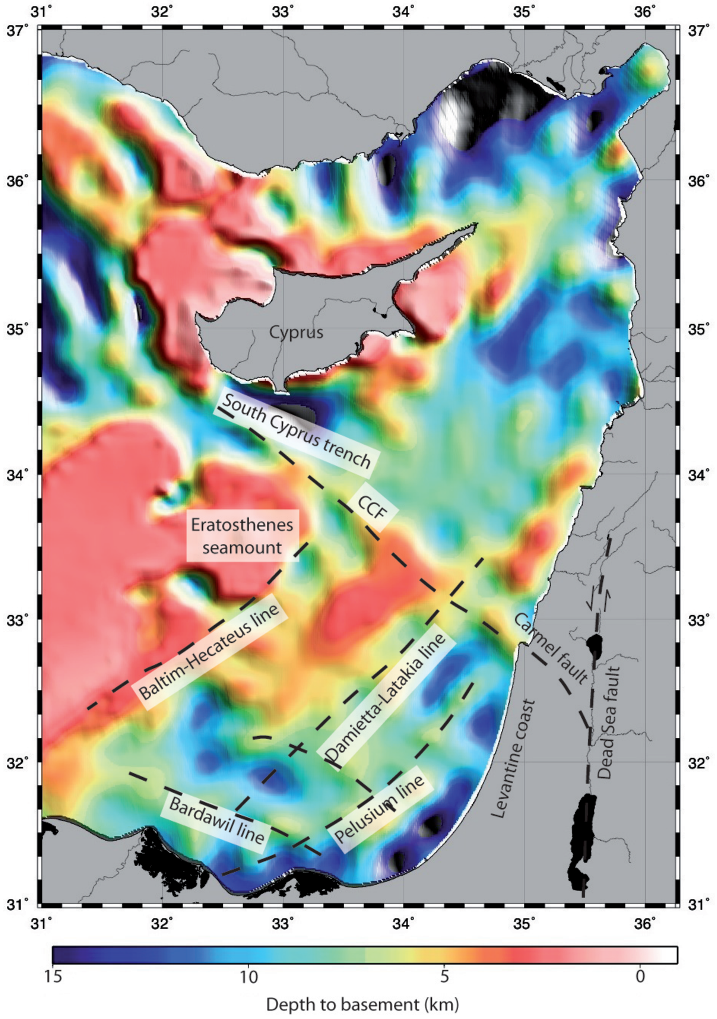

(a)

Figure 53: Depth to basement map, derived from gravity inversion. The absolute depth values may incorporate errors, but the general trend between basement highs should be well constrained. Horst and Graben structures can be observed offshore the Levantine. Generally, the structure are aligned in NNE trend.

Additional to these two maps, we have derived a residual bathymetry map (Figure 54(a)), where especially regional scale structures, i.e., with wavelength of less than 150km, are displayed that have a recent expression at the surface. This means for example changing slopes angles or recent deep rooted tectonic structures are mapped as anomalies. Therefore, the map gives evidences for large scale Neotectonic features. However, the absence of an anomaly is not a criterion to rule out the presence of a structure, due to the fact that the structure must have a recent expression at the surface which is not always given.
In Figure 54(a), we mainly observe the general trend of the maps in Figures 52(a) and 53(a). Most anomalies are striking in NNE-SSW direction. We can clearly identify large positive anomalies next to the coastlines and the Eratosthenes seamount in the map, which corresponds to the change of the slope angle at the corresponding continental slope. In addition to this, we mainly observe positive anomalies in the Levantine basin, where one these can be correlated to the position of the Damietta-Latakia line (see Figure 54(a)). In contrast to that, we hardly see evidences of the NW-SE striking elements as indicated before.

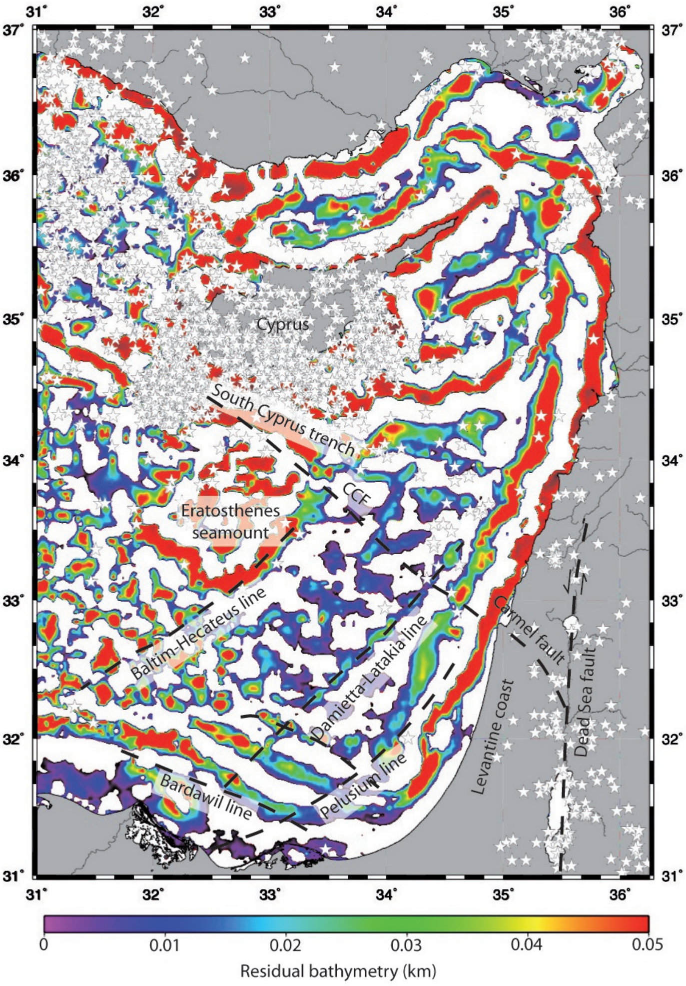

(a)

Figure 54: Residual bathymetry map, derived by a filtering process of bathymetry data. Structures with wavelength of less than 150km that have a recent expression at the surface are displayed. The expressions of the Diametta-Latakia line can be well observed as a residual lineament on the map. White stars indicate earthquake locations in the area.

6.5 Interpretation and discussion

Throughout the southern Levantine basin, we identified up to 12km thick sediment sequences in the depth domain. This overall thickness is in good accordance to previous works of Ben-Avraham et al. (2002) and Netzeband et al. (2006a) who estimated up to 14km thick sediment bodies. According to Farris and Griffiths (2003), the sediments consist of sequences formed during Triassic/Jurassic to recent ages. The presented stratigraphic model shows a good similarity to the one derived by Gardosh and Druckman (2005), but also defined differences exist. The sequences from Plio-Pleistocene to Messinian correspond to the interpretation in Gardosh and Druckman (2005) (units F to E) which were calibrated with near coastal wells. The Early Cenozoic sequence can be correlated to sequence D in Gardosh and Druckman (2005), but they interpreted these deposits as Neogene and we as Paleogene. The Cretaceous sequence is in contrast to Gardosh and Druckman (2005). They interpreted Early Cretaceous to early Paleogene deposits. The older sequences (i.e., Jurassic to Triassic) are in good accordance to each other, although the exact age for the Late Jurassic sediments differs. For a detailed comparison of both models take a look at Figure 37(a).

6.5.1 Stratigraphy of the Messinian evaporites

Stratigraphy The Messinian sequence has a well defined internal structure (Figure 48(a)), which was indicated by other authors before (e.g., Gradmann et al. (2005); Bertoni and Cartwright (2006); Netzeband et al. (2006b)). The different nomenclature for these evaporite sequences has been homogenized by Hübscher and Netzeband (2007b), their stratigraphic model for the Messinian evporites consists of six sequences and assumes four seismically transparent layers (ME-I, ME-II, ME-IV, and ME-VI) and two high reflective layers (ME-III and ME-V). Based on the work of Mitchum et al. (1977) the absence of internal reflections in four low reflective sequences has been taken as an indicator for the presence of Halite. The internal reflections of sequences ME-III and ME-V has been discusses as originating from alternating successions of clastic sediments and / or different evaporitic facies. We could confirm these sequences by the depth migration results and trace the sequences throughout the southern Levantine basin with the help of seismic data (see Figures 43(a) and 50(a)). Therefore, the proposed stratigraphic model for the Messinian evaporites of Hübscher and Netzeband (2007b) could be spatially expanded in the southern Levantine basin. Furthermore, the assumption of intercalated clastics in the high reflective sequences (e.g., Garfunkel et al. (1979)) can be ruled out, due to the fact that the stratigraphic model holds true throughout the basin, whereas intercalated clastics would be a local feature.

Bertoni and Cartwright (2006) identified the structural highs and lows related to the Syrian Arc structures as the main controlling factor for the accommodation space of the MU. Netzeband et al. (2006b) proposed that the MU generally move / flow into NNE direction, parallel to these structural highs and lows. According to Netzeband et al. (2006b) the top of the evaporites declines beneath the Nile cone in the south and beneath the sediments in the east, due to the lateral displacement by salt flow and because of the differential load of the sediments next to the coastlines. Consequently, many authors identified the NDSF as the main generator of the stress causing the NNE movement (e.g., Loncke et al. (2006); Netzeband et al. (2006b)). The NDSF squeezes the salt from the Nile cone towards the north, due to the differential onload of the deposited sediments. Maximum thicknesses of the salt were observed where the NSDF begins to thin out. The thickness maps derived from our data also support this conclusion (Figures 43(a) and 45(a)). In Figure 43(a), we observe maximum thicknesses of the MU next to the NSDF and a decline of thickness away from this area. The thicknesses contour lines of the MU show a distinct elongation towards NNE, which is also parallel to the basement structures, e.g., Syrian Arc fold belt and the Horst and Graben structures observed in this study (e.g., Figure 53(a)).
We also observed extensional fault structures at the shelf, compression structures in the central basin, and at the end of the profiles occasionally normal faults in the opposite direction (see Figure 49(a)). This observation also supports the interpretation of a movement in NNE direction, since an overall NNE movement would lead to a movement vector component pointing towards the basin centre. The salt flow is bounded to the west by the Eratosthenes seamount (Netzeband et al., 2006b) and to the east by the Syrian Arc structures (Bertoni and Cartwright, 2006).

According to Bertoni and Cartwright (2006); Netzeband et al. (2006b) all internal sequences are faulted and folded independently. We also observe this feature in our depth migrated data. We also see a higher folding degree for the high reflective sequences than for the low reflective layers. Taking the several refilling phases during the MSC (Gargani and Rigollet, 2007) into account and therefore an discontinuous precipitation of the salt body, the individual MU sequences can quite well indicate an independent deformation behavior. Consequently, Netzeband et al. (2006b) suggested thin skinned salt tectonic during the depositional stage.
Additionally to this feature inside the MU, we also see a differential mechanical behaviour of the high reflective sequences and the low reflective sequences, when they are present at the top of the evaporites (Figure 49(a)). High reflective sequences form a rougher surface, whereas the low reflective sequences form a smoother surface. Two possibilities could explain this observation, the first one is differential erosion behavior of the corresponding sequences at the top of the MU and secondly by differential rock mechanical behavior. The first possibility assumes that the high reflective layers are partly easier to erode. Due to the high reflective characteristics, the sequence most likely consists of different components, in

which one component might be easier to erode. In this case the erosional surface represents a kind of cuesta type topography. The second possibility would consequently assume, that the high reflective layers are easier to deform than the low reflective sequences. Also a combination of both mechanisms is possible. The spatial distribution of this deformational behavior, i.e., the toplap of the individual sequences at the top of the MU, occurs in similar depths throughout the southern basin (Figure 50(a)). This indicates a simultaneous erosion of the marginal parts of the Messinian sequence and may be caused by subarial exposure or a reflooding at the end of the MSC.
By looking further in the basin, we see between CMP number 6500 and 8000 in Figure 49(a) that all internal salt structures are stretched, hardly any faulting occurs, which indicates a translational domain in this area. In contrast to that, we observe between CMP 3000 and 6500 in Figure 49(a), a high degree of deformation in terms of a high fold level, which correspond to a compression setting. Taking the extensional domain at the shelf into account, these salt tectonic considerations can be quite well linked with the typical thin-skinned salt tectonic model of Vendeville (1999), which consists of an extensional part at the shelf, a translational part in an intermediate area, and a compression part in the basin. In the case of the MU this model seems to be additionally affected by the corresponding internal salt sequence at the top of the salt layer, described before.
From the observations above, we conclude that the deformation of the MU is not only controlled by differential sediment load, (e.g., Gradmann et al. (2005), but also by the rheology of the corresponding uppermost MU sequence.

Deformation considerations can also be done for the Plio-Pleistocene sediments on top of the MU. We mainly observed extensional faulting at the shelf areas (Figure 40(a) and 41(a)). In Schattner et al. (2006) two types of faults are described for the shelf area. First, faults driven by halokinetic processes and second, deep rooted faults. It could be observed that most of the former features originate at the top or at the base of the MU. The origin of the latter ones cannot be clarified, due to resolution problems in the shelf area.
When we take a look at the sediments overlying the MU in the shelf area, we see on all three depth migration results, a parallel reflection pattern directly overlying the salt body which points to a pre kinematic sedimentation. On top of these sediments, we observe a chaotic reflection pattern (Figures 44(a) and 46(a)). Several authors interpret this complex as a late Pliocene slump complex (e.g., Frey-Martinez et al. (2005); Netzeband et al. (2006b)). It reaches volumes of ca. $1000km^3$, which where estimate with the help of 3D seismic in Frey-Martinez et al. (2005). Earthquake triggers were interpreted as the most important agent of downslope sediment transport. On top of the slump unit, we see a divergent reflection pattern, which points to a syn-kinematic sedimentation (see Figure 44(a) for an example on profile B). Therefore, the Plio-Pleistocene can be differentiated at the shelf in a pre- and a post-slump unit (Figure 46(a)), which probably governed parts the thin skinned salt tectonic by creating a gravitational disequilibrium top of the MU.

Looking at the base of the MU, we see a partly erosional unconformity between the Early Cenozoic sequence and the Messinian in the southern part of the Levantine basin (Figure 42(a)). Some authors consider this feature as a possible hydrocarbon play (e.g., Roberts and Peace (2007)) with the Messinian salt as the seal horizon. Maillard et al. (2006) describes a basal erosion surface (BES) for a marginal basin in the Western Mediterranean. In this study, we can observe an erosional unconformity on the two southern profiles A and B in a depth of approximately 4km. The reason for this pre-precipitation erosion still remains unclear, but may point to differential subareal exposed basin parts during the MSC. The depth levels for the erosional truncation at the base of the MU quite well correlate to the depth values of the base of the MU given in Netzeband et al. (2006b). Cartwright and Jackson (2008) estimated a drawdown of the sealevel of 800m during the MSC. In contrast to that Netzeband et al. (2006b) estimated a basin depth of about 2km after a backstripping analysis of the overlying sediments. Therefore, we have a difference of 1200m. If this difference can be linked to a large scale tectonic subsidence setting or other reasons, remains unclear.
There is a clear difference between the marginal basin, i.e., the southern profiles, and the northern profile C. Here, we do not see an erosional unconformity, although the internal sequences of the MU correspond to each other, in terms of thickness and facies. The observation that a basinal erosional

surface is present in the Eastern Mediterranean indicates that parts of the Western and parts of the Eastern Mediterranean probably underwent similar evolutionary phases at the onset of the MSC. However, the internal stratigraphy of the evaporites is significantly different.
Additionally to this, we see that a Marginal Erosion Surface (MES) as described by Maillard et al. (2006) for the Western Mediterranean is not present in our depth migrated results. At the shelf, the pre Messinain and the Plio-Pleistocene form an conformity. This points to a significantly different evolution of the MU in the marginal parts the Eastern and Western Mediterranean. A final conclusion about the link between the eastern and the western Mediterranean cannot be given here.

Finally, we can give some more insights on a precipitation model for the MU. Due to the spatial distribution of all internal MU sequences and the prograding lapout of ME-VI to ME-III, and to ME-I on the southern profiles, we conclude to a "Bull-Eye" structure of the MU. In a typical "Bull-eye" model, the evaporites with the highest concentration would precipitate last. However, due to refilling processes during the Messinian (Gargani and Rigollet, 2007) concluding from this circumstance to the evaporite facies would fail. Thus, we can only described the precipitation model as a ÒBull-EyeÓ structure, and assume the reoccurrence of certain evaporites in this "Bull-Eye" (high reflective layers) due to the refilling processes. However, the exact composition of the internal sequences remain unclear which heavily depends on the assumed MSC model (i.e., Clauzon et al. (1996) or Krijgsman et al. (1999)).

Interval velocities for the Mobile Unit In chapter 4.2, we presented a detailed interval velocity for the internal sequences of the MU (Figure 51(a)). We identified higher velocities (around 4200m/s) for the low reflective layers than for the high reflective layers (around 3800m/s), which due to the correlated internal stratigraphy of the MU might be true for the whole southern Levantine basin. Generally, the derived velocities have to be considered as good approximation of the real velocities, but residual velocity errors due to the complex wave propagation behavior in this area are present. The observed velocity values are partly significantly lower than velocity values from laboratory experiments for Paleo-Mesozoic evaporites, e.g., Zechstein salt (e.g., Kearey and Brooks, 1991). In Gardosh and Druckman (2005) a velocity of 3311m/s from onshore well information was considered as unreasonable and a velocity of 4200m/s was assumed for the whole salt body. Ezersky et al. (2005) determined velocities of 2900m/s to 4200m/s for the Dead Sea from well information. Maillard et al. (2006) estimated velocities of 4400m/s for the salt body and 3400m/s for the so-called upper evaporites, which might be an equivalent to the high reflective layers inside the MU. When revisiting all these velocities, we have to conclude that for this young, and probably wet (i.e., due to gypsum anhydrite conversion) evaporite body slower velocities than normal interval velocities for Paleo-Mesozoic evaporites have to be considered.
Dümmong and Hübscher (2009) measured velocities of refracted wave from the top of the MU on profile B. They saw that the high reflective layers generally show slower refraction velocities (about 4300m/s) than the low reflective layers (4500m/s). These refraction velocity values and the reflection velocities in this study indicate a significant dependency of the velocity on the wave propagation direction. It seems that horizontally propagating waves, i.e., refracted waves, have a higher velocity than mainly vertically travelling waves. Consequently, this observation points to layered sequence anisotropic behavior for the MU.
The derived velocity distribution in Figure 51(a) also indicates the complexity of the MU sequences in terms of processing challenges and may also point to changing evaporite facies inside the Messinian salt layer (e.g., Bertoni and Cartwright (2006); Hübscher and Netzeband (2007b)), and at least to independent mechanical behavior of the individual MU sequences, which was already indicated before.

When we link all the observations, namely the individual mechanical behaviour and the differential erosion behaviour at the top of the MU, the velocity distribution inside the MU, and reflectivity of the individual MU sequences, we can describe the MU sequences (ME-I to VI) in a much more complex way. However, the results also indicate that the complete evaporite behaviour still cannot be fully described on the base of seismic investigation, i.e., the exact composition is still unknown.

6.5.2 Plate tectonics

Basement morphostructure Recent studies (Vidal et al., 2000; Netzeband et al., 2006a) postulate thinned continental crust for the Levantine basin. According to Netzeband et al. (2006a) the crystalline basement consists of two layers with a P-wave velocity of 6.0km/s-6.4km/s for the upper crust and with 6.5km/s and 6.9km/s for the lower crust. This assumption matches the observation of the crust under the Levantine and Jordan in the east and in the north under the Mediterranean Sea near Greece. In Netzeband et al. (2006a) a β-factor of 2.3-3 for the crust was estimated, assuming a crystalline basement with a constant thickness. From our data (Figure 53(a)), we clearly see that the basement is highly structured showing some distinct highs and lows. Horst and Graben structures were not included into the model of Netzeband et al. (2006a), thus the β-factor was probably calculated too high. However, our observation is not contradicting Netzeband et al. (2006b) and the postulation of rifted continental crust still holds true.

We observed on basis of our data derived from gravity inversion mainly NNE-SSW striking Horst and Graben structures (Figure 52(a) and 53(a)), which correlate quite well with the interpreted acoustic basement on the depth migrated seismic data shown in Figures 39(a) - 41(a). In the main working area offshore the Levantine coast the Horst and Graben trends follow quite accurate the shoreline (Fig. 18). The near shelf highs can be linked to the so-called Syrian Arc structures (Gardosh and Druckman, 2005). According to the tectonostratigraphic scheme in Figure 37(a), the Syrian Arc structures were initially formed during Cretaceous ages in passive continental margin setting. They follow the general NNE-SSW trend in the Levantine basin. The up-doming processes of the Syrian Arc inversion are illustrated by normal faults affecting the deeper sediment structures (eastern parts of the sections in Figures 39(a), 40(a), and 41(a)). The sediments of early Cretaceous age are the youngest sequence clearly affected by the up-doming processes in terms of normal faults. The lower Cretaceous sequence is assumingly the last syn-rift sequence in the Levantine basin (Farris and Griffiths, 2003). Consequently the earlier sequences are post-rift structures. According to our seismic data, the up doming processes of the Syrian Arc inversion affected the syn-rift structures afterwards. This up doming process started according to the tectonostratigraphic scheme in Figure 37(a) in late Cretaceous times.
When we go from the Syrian Arc structures further to the east, we identified on all depth migrated profiles a defined basement low surrounded by Horst structures (Figures 39(a), 40(a), and 41(a)), which quite well corresponds to the Graben structure between 33.5 deg - 34 deg E and 32 deg - 33 deg N on the depth to basement map in Figure 53(a). In the western part on the northern most profile (Figure 41(a)) we find a defined basement high, which can also be correlated the western Horst on the basement map between 33 deg - 34 deg E and 32.5 deg - 33.5 deg N. The eastern Horst, identified on the depth migration results, is also displayed on the depth to basement map running parallel to the Syrian Arc structures with a small extension in east-west direction (Figure 53(a), between 33.5 deg - 34.5 deg E and 32 deg - 33 deg N). Thus, we see a defined Horst and Graben structure west of the Syrian Arc fold belt, which is in contrast to the observation by Breman (2006), who identified a structural high offshore the Levantine coastline (Western offshore High).

Generally, almost all basement structures align to the general NNE-SSW trend in the southern Levantine basin. Schattner et al. (2006) observed mainly NNE-SSW trending structures for the Levantine basin between 32 deg N and 34 deg N. When we look further north, we see a change from this behavior (Figures 52(a) and 53(a), north of 33.5 deg N). The basement structures seem to align in N-S direction parallel to the Ghab-fault line (see Figure 36(a)). According to Butler et al. (1997), the Yamouneh and Ghab fault have been inactive for the past 5 Ma. These authors considered the N-S striking Roum fault as the principally, perhaps exclusively active transcurrent fault. This suggests that the Horst and Graben structures north of the 33.5 deg N also reflect the rifting phase and not the Neogene tectonics. North of 35 deg N the basement structures align again to the NNE-SSW trend. It seems that the basement structures in the Eastern Mediterranean show a general N-S to NNE-SSW orientation, parallel to the different branches of the DSTF, i.e., the Yamouneh fault and the Ghab fault, and the deep rooted transform faults in the Levantine basin, e.g., the Damietta-Latakia line.

Besides the above-mentioned major NNE-SSW trend in the basin, we also observed the NW-SE striking CCF, which connects the southern margin of the Cyprus Basin with the Carmel fault on the Levantine coastline. The CCF is located in the direct extensional direction of the Carmel fault and is consequently considered as the related extension. The Carmel fault continuation was highly debated for years (e.g., Ginzburg et al. (1975); Garfunkel and Almagor (1984)). Schattner et al. (2006) postulated the continuation of the Carmel fault in NNE direction parallel to the main slope and basement structures in Figure 53(a), which requires a bending of the Carmel fault from NW to NNE. In this direction, we see a defined basement high between 33 deg N and 34 deg N parallel to the Levantine coastline (Figure 53(a)). Schattner et al. (2006) postulated the prolongation of the Carmel fault in the direction of a deformation belt, which probably can be correlated with our gravity and basement data observation and has to be considered as a possible continuation of the Syrain Arc fold belt. Abdel Aal et al. (2000) proposed a continuation in NNW direction and Hofstetter et al. (1996) postulated the prolongation of the Carmel fault in NW direction, which quite well matches our observation. The CCF prolongs into the south Cyprus trench (see Figures 53(a) and 52(a)). Due to the faulting direction of the Carmel fault, the CCF can be considered as a sinistral strike slip fault, but exact evidences are missing. Vertically above this lineament, we also described thickness anomalies in the Messinian evaporite sequences ME-I-III, which suggests tectonic activity of the CCF during late Miocene (Figure 50(a)). These anomalies do not result in active tectonic overprint of the Plio-Pleistocene sediments and we could not verify our observation with the help of earthquake locations or on the residual bathymetry map (Figure 54(a)). The latest activity is therefore present in the Messinian age. Thus, we consider the CCF as a passive structure.
Piromallo and Morelli (2003) observed mantle velocities for the eastern Mediterranean. They modified a reference velocity model and observed a prominent anomaly that can be spatially well correlated with the CCF, suggesting that the Cyprus-Carmel fault might represent a major geodynamic structure.
Another observation is that the striking direction of the CCF lineament directly leads from Haifa into a Pockmark field described by Sade et al. (2006), which suggests fluid escape along an active fault, originating assumingly in the evaporite body.

Mascle et al. (2000) postulated the Sinai Microplate. The Boundaries of the triangular Levantine-Sinai Microplate should be well delimited by Dead Sea transform to east and Cyprus active margin to north. Its western boundary includes the Suez rift system and its probably submerged extension into Mediterranean Sea (Figure 36(a)). From our data, we cannot confirm this observation, since we do not see any recent or past tectonic expression of the western boundary of the Sinai Microplate in our data (Figures 52(a), 53(a), and 54(a)). Furthermore, the plate boundary in the north of the Levantine basin, i.e., the subduction zone of the African plate, is also not resolved in our data.
The basement morphostructure further shows that the Eratosthenes Seamount and the Herodotus basin are structurally linked. The seamount is consequently part of the African Plate.

Active plate tectonics and salt tectonics We identified a NNE-SSW striking, thick skinned, deep rooted fault structure on all three prestack depth migrated profiles (in Figure 39(a) around CMP number 3000, in Figure 40(a) around CMP number 6000, and in Figure 41(a) around CMP 5500). This fault structure seems to be located on or next to the assumed position of the Damietta-Latakia fault line (Neev, 1975). It also has a recent expression on the residual bathymetry map (Figure 54(a)). Many authors (e.g., Farris and Griffiths (2003)) indicated seismically transpressive behavior of the Damietta-Latakia line. On the northern profiles, the lower internal salt sequences are affected by the Damietta-Latakia line, but the tectonic overprint cannot affect the whole salt layer (Figure 47(a)). The Plio-Pleistocene sediments are not disturbed on the northern profiles (profiles B and C). Only on the southern most profile, we see that the deep rooted fault clearly propagates trough the salt and affects the sediments in the overburden. We therefore conclude, that mostly the MU is able to decouple the deep-rooted tectonic movement from the overburden. Only in the southern part of the working area, a deep rooted fault seems to affect the MU, which points to the observation of a more brittle behaviour of the MU in the marginal parts of the basin. When we look at the northern profiles in more detail, we see that deep-rooted tectonic movements affect the ME-I and ME-II, but ME-III already decouples this movement. This is also in good accordance to the observation of a more mechanical rigid behaviour of the transparent Messinian sequences, when they

were not fold as heavily as the high reflective sequences. Additionally, the residual bathymetric anomaly along the Damietta-Latakia line can spatially well correlated with the St. Pauli mud volcano in Netzeband et al. (2006b) (i.e., approximately at 32N, 33.2E). Fluids propagating through the MU were assumed to feed the volcano with fluids from beneath or within the salt. Due to the spatially correspondence of the Damietta-Latakia line with the residual bathymetry and the mud volcano, it can be assumed, that the deep rooted fault system may open faults in the MU, where fluids can rise to the surface. If the Damietta-Latakia line disturbs the whole MU in this location or only the lower parts, cannot be clarified.
In Figures 52(a) and 53(a), the assumed position of the Pelusium and Baltim-Hecateus line are also displayed. Especially the Pelusium line cannot be clearly identified on the seismic sections, since the resolution of the seismic data is heavily reduced under the salt roller structures (e.g., see Figure 44(a)). Gradmann et al. (2005); Schattner et al. (2006) postulated recent deep rooted tectonic events in the shelf areas of the Levantine basin, associated with the Pelusium Line. Thus, deep rooted tectonic fault systems, i.e., the Damietta-Latakia and the Pelusium line seem to be active in the Levantine basin.

When we take a closer look at the thin skinned salt tectonic expressions at the shelf, we see the so-called salt roller structures. Salt roller structures occur on the northern profiles and non-rolling structures occur on the southern profile. According to Cartwright and Jackson (2008) this geometrical behaviour of the salt is caused by a change from low extensional domain in the south to a high extensional domain in the north offshore the Levantine coast, which is also visible in the fault systems in the overburden, i.e., on profile A hardly faults affect the Plio-Pleistocene sediments (Figure 38(a)), whereas on the northern profile many faults occur (Figure 39(a) and 40(a)).
In contrast to the models proposed in Cartwright and Jackson (2008), which all assume an undisturbed base of salt; we see fault structures crossing the base of the evaporites, although the origin of these faults is unclear (see Figures 44(a) and 46(a)). We will not contradict the models proposed, but add new features to the discussion. The models of Cartwright and Jackson (2008) heavily rely on the up doming processes in the Israel hinterland and the synchronic subsidence of the Levantine basin. This causes gravitational instability inside the salt, which forces the salt to flow, and additionally the differential sediment load creates stress in the overburden. Our observation does not contradict these mechanisms, but we also see distinct deep-rooted faults, which faulted the base of the MU. Therefore, the salt rollers are created by gravitational processes, but also influenced during or after their generation by tectonic mechanisms. Since only one internal salt layer is present in the salt rollers, our discussion is also supported by the observation that the transparent salt layers are mechanically more rigid than the high reflective layers, which makes the salt rollers less flexible to strain created by the gravitational processes. Therefore, our observation points to a combination between gravitational processes, intrinsic features and tectonic extension casued by sedimentary onload, as already indicated by Netzeband et al. (2006b). Final statements about this very complex area are complicated to state only by processing and interpreting seismic data.

Generally, we observed that the majority of the recent tectonic activity is caused by the deformation originated from salt body tectonic movement, and therefore has to be interpreted as thin skinned processes. Only along the deep rooted major fault structures, e.g., Diametta-Latakia line, or at the shelf, the salt is faulted by thick skinned processes, i.e., faults originating below the salt.

6.6 Summary and conclusion

The results presented in this study have two main objectives, one is the characterisation Messinian evaporate sequence, which was described in detail in the depth domain and the second objective is the investigation of Levantine basin basement structures. The results of both investigation objectives will be summarised in this chapter and conclusions will be drawn.

Messinian evaporites (MU) The internal MU sequences ME-I to ME-VI could be traces in the depth domain throughout the southern Levantine basin. We presented thickness maps of the individual sequences, which allowed a detailed spatial characterisation and interpretation of the individual MU sequences. Since the entire sequence has never been drilled before, the interpretation has to rely on seismic data; no well calibration is possible yet. ME-III and ME-V reveal a high reflectivity whereas ME-I, II, IV, and VI show low reflectivity. Therefore, we conclude that the proposed stratigraphic model for the Levantine basin from Hübscher and Netzeband (2007b), with changing evaporite facies is validated in this study. Additionally, the assumption of intercalated clastics as the generator of the high reflectivity in sequences ME-III and ME-V could be ruled out.

Furthermore, we showed a detailed velocity distribution from a representive part of the deep basin, where hardly any tectonic overprint in terms of faults or folds was visible. Generally higher velocities (4000 - 4200 m/s) were obtained for the low reflective layers, whereas lower velocities (3800m/s) were obtained for the high reflective layers, which indicate even more, the previously proposed independent mechanical characteristics of the individual MU sequences (e.g., Netzeband et al. (2006b)). From refracting waves velocity investigations on profile B in Dümmong and Hübscher (2009), a significant difference of the seismic velocities for mainly horizontally and mainly vertical travelling waves was recognized, which points to layered anisotropic behaviour inside this tabular salt body.
The independent mechanical behaviour is also represented by the differential behaviour of the individual sequences, when they form the lapout against the top of the MU. Here, the high reflective sequences form a smoother surface and the high reflective layers a rougher one. If this observation is related to mainly the mechanical behaviour or to differential erosion behaviour cannot be clarified. The situation even more complicates, since this behaviour coupled to the typical thin skinned salt tectonic model after Letourzey et al. (1995); Vendeville (1999).

Generally, we saw that the MU is able to decouple deep rooted tectonic events, e.g., the Damietta-Latakia line from the Plio-Pleistocene sedimentary overburden. We saw on profile A that the Damietta-Latakia line can affect the whole MU and the overburden, but further north in the Levantine basin only ME-I and ME-II are affected by the assumingly transpressive fault behaviour.
In the marginal parts of the basin, i.e. the shelf area, we observed that the base of the salt roller structures is not only governed by intrinsic, i.e., salt mechanical behaviour but also by faults that originate below. Nevertheless, the models for the salt roller development by Cartwright and Jackson (2008) still seem to hold true, but a disturbed base of salt has to be considered as an extra constrain for the generation.
Almost all thin skinned faults in the northern shelf areas propagate trough the Plio-Pleistocene and have be considered as recent, which indicates the high extensional domain in the northern part of the working area (Cartwright and Jackson, 2008). A low extensional behaviour in the southern part of the working area is characterised by the absence of salt rollers and less fault patterns in the overburden.

When we compare our results in the Eastern Mediterranean to the results of Maillard et al. (2006) in the western Mediterranean, we see differences but also some similarities. The MU general stratigraphy is generally different in both parts of the Mediterranean and we do not see the so-called marginal erosional unconformity between the pre Messinian and the Plio-Pleistocene. However, Maillard et al. (2006) described an erosional unconformity for the top and base of the MU, which we also partly could observe, depending on the location in the basin. Therefore, both large major Mediterranean basins probably have undergone different evolutionary stages, but similarities exist.

Plate tectonic Several NNE-SSW striking basement structures, e.g., Horst and Graben structures, Syrian Arc structures, where indentified which form the structural basement in the Eastern Mediterranean. These structures were probably formed during the early rifting stages in the development of the Levantine basin. The Offshore High assumed by Breman (2006) could be identified as a Graben structure included into the NNE striking basement structures in the Levantine basin.
We identified the so-called Carmel Cyprus fault (CCF) lineament on the basement maps and residual gravity maps derived from 3D gravity satellite data inversion. This lineament could be correlated as the extension of the Carmel fault, following an argumentation of Hofstetter et al. (1996). We see tectonic imprints of the CCF in the first internal sequences of the MU, but recent active tectonic activity cannot be seen on basis of our data.
North of the CCF the striking direction of the basement structures changes into a N-S direction, and north of 35 deg N it again changes back to NNE-SSW. Therefore, the striking direction of the main geological

features in the Eastern Mediterranean seems be parallel or almost perpendicular (e.g., CCF, Bardawil line) to the dominating tectonic features in this area, the DSTF and its northern prolongations, i.e., the Yamouneh fault and the Ghab fault. Thus, we conclude that the orientation of the main basement structures in the Eastern Mediterranean is either NNE-SSW or NW-SE, i.e., almost a checkerboard like design is formed by the basement structures. All the identified basement structures are illustrated in Figure 55(a). A geological map after Breman (2006) was modified with our observations and summarises the above mentioned.

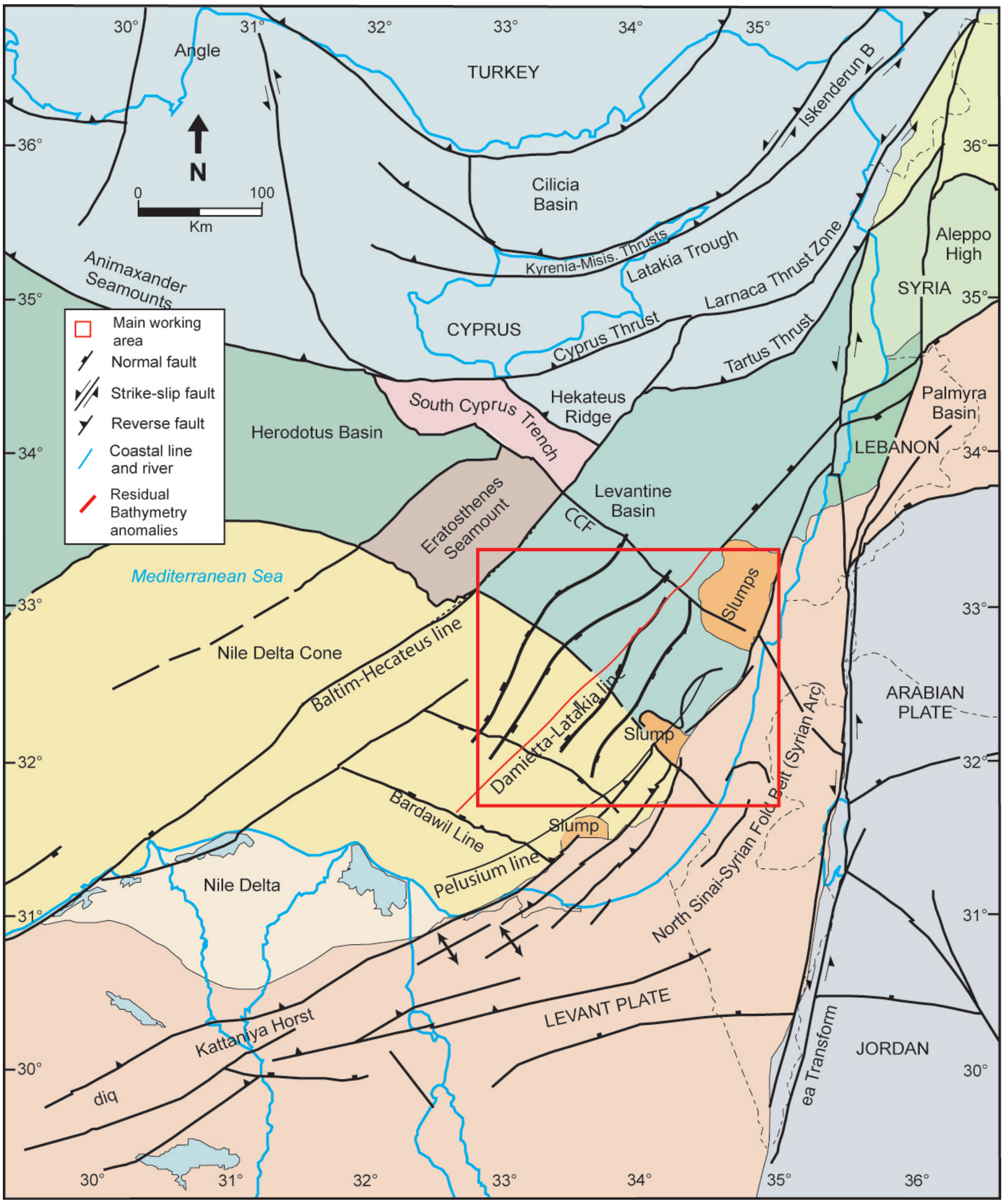

(a)

Figure 55: Geological map for the Eastern Mediterranean / Levantine bain modified after Breman (2006) including the results of this study. In contrast to Breman (2006), we identified a Horst and Graben structure in the Levantine basin.

7 CONCLUSIONS AND OUTLOOK

I have presented a successful application of the expanded CRS workflow to a marine industry data set from the Eastern Mediterranean / Levantine basin. I extended the workflow with a newly developed surface related multiple attenuation tool and showed how to incorporate the prestack data enhancement tool of Baykulov and Gajewski (2009b) into the workflow, especially in terms of multiple suppression. Although highly challenging tasks, like multiple attenuation and prestack data quality enhancement, are newly addressed in the CRS workflow, the main characteristics like robustness, simplicity, and speed are still preserved. Additionally, with the help of the prestack data enhancement tool, an interface to other non CRS related workflows is achieved.
In addition to the well established items, i.e., the CRS stack (Jäger et al., 2001) and the NIP-wave tomography (Duveneck, 2004b), the newly added items extend the application range of the CRS workflow. Pre-stack data enhancement by partial CRS stacks is very stable and robust, due to the fact that it interpolates data by stacking only. No data transformation or sophisticated interpolation tools are necessary, only reliable CRS attributes have to be determined. The same arguments hold for the development of one multiple attenuation tool with CRS attributes. Here, speed and simplicity are achieved by performing the multiple prediction in the poststack data domain, and afterwards transforming the data back to the prestack data domain. Additional robustness is achieved by independence on the data regularity, only a sufficient stacking result have to be present. The quality of the results heavily depend on the quality of the CRS attributes.
The second development for multiple attenuation illustrates a newly added characteristic of the expanded CRS workflow. It can be interfaced to other processing workflows with the help of the partial CRS stacking technology. Data for a lot of processing tasks can be regularised with the help of CRS related technology. The processed data could be regularised in a way which is perfectly suitable for the SRME process (Verschuur et al., 1992). Also unwanted filter effects could be removed. Therefore, certain items of the CRS workflow are no longer restricted to the whole processing chain within the CRS workflow. Data processed with the partial CRS stacks can be used in other frameworks as well.

Additionally to that, I could derive a geological interpretation of the data set from the Eastern Mediterranean on the basis of the results obtained with the expanded CRS workflow and additional data sources. Other authors, e.g., Baykulov et al. (2008), showed the successful interpretation of results obtained with the old version of the CRS workflow (i.e., CRS stack, NIP-wave tomography, and a subsequent depth migration), but here, for the first time, the expanded CRS workflow is applied on one data set only.

Due to the fact that I have already given detailed conclusions and outlooks of the individual items in the previous chapters of the thesis, I will focus here on the outlook with regards to the complete expanded CRS workflow.

Due to the fact that exploration targets of the hydrocarbon industry are getting more and more challenging. It would be desirable to incorporate tools into the CRS workflow, which do not rely on the second order hyperbolic approximation. One attempt to achieve this is illustrated in this work. We preconditioned the input data with the help of the partial CRS stacks for a subsequent SRME process. We can consider only the offset positions in the data, where regularisation work is necessary. This leads to a data set, where only the missing traces are interpolated in a hyperbolic way and the potentially non hyperbolic parts of the data would still be present. SRME could use this and consider the wave propagation in the subsurface correctly, without a restriction to second order. Another non hyperbolic method is also presented in this thesis, namely prestack stereotomography (Billette and Lambaré, 1998). In comparison with NIP-wave tomography, we observed that the restriction to second order hyperbolic approximation of NIP-wave tomography could not resolve the velocity model as clear as desired for some tasks. Klüver (2006) presented a way to overcome this restriction for the NIP-wave tomography, in terms of model based traveltimes and a residual moveout correction. Unfortunately, the method was so far only tested on synthetic data. This indicates the way to process more complex models correctly.
A further extension of the CRS workflow, is the incorporation of a multiple attenuation tool for internal

multiples, which are often present in land data sets with strong reflection horizons. The CRS stack has strengths in processing land data sets, because it can increase the often bad stacking fold significantly. Therefore, addressing internal multiples, mostly present in these data sets, is desireable. An intuitive way to include this would be to extend the poststack multiple prediction tool to internal multiples in the same way the original SRME method was extended to the Internal Multiple Elimination (IME) tool (Jabukowicz, 1998). The necessary extraction of a reference horizon could be easily achieved using the high quality CRS stack sections, most likely in an automated way based on semblance.
Another extension of the CRS workflow, that was already indicated in the frame of the multiple attenuation chapter, is the incorporation of seismic interferometry, e.g., Curtis et al. (2006). Similar to the methods described by Behura (2007), seismic interferometry can be directly included into the CRS workflow, with the help of the partial CRS stacks. Similar to the second approach of multiple attenuation in this thesis, the partial CRS stack would precondition the data for the seismic interferometry. Then the source wavelet could be extracted from the data without any major approximations. Many methods, e.g., multiple attenuation tools, would benefit from the exact knowledge of the wavelet.

More general considerations for expanding the CRS workflow are, to incorporate non seismic tools, e.g., gravity or electromagnetic measurements. This would consequently lead to so called joint inversion procedures, e.g., Heincke et al. (2006); Colombo and DeStefano (2007); Colombo et al. (2008). These procedures combine different geophysical data sets by an integrated inversion process, whereas the seismic velocity is mostly linked to the resistively and to the density of the considered medium. The combination of these methods provide the capability to widen the resolution of the individual method. NIP-wave tomography could play an important role in these kind of inversion schemes, due to its simplicity, robustness and additional constrains to the traveltime. It may be worth to incorporate NIP-wave tomography into a joint inversion scheme, where usually conventional traveltime tomography is used, which often uses first arrivals, i.e., direct waves.

As we can see form the previous considerations, most of the tools in the CRS workflow heavily rely on the quality of the CRS attributes. Therefore, improving the quality of these attributes should be a common goal for further developments. Several attempts have been made to improve the quality of the CRS parameters, e.g., Klüver and Mann (2005); Müller (2007). Geostatistical filtering, e.g., Coleou (2001); Hoeber et al. (2003), can also play an important role. Especially, in Coleou (2001) it is shown, how geostatistical filtering can improve the quality of stacking velocity fields. With the help of variogram decomposition and Factorial kriging (Matheron, 1982), spatial filters could be derived which are very efficient in removing organised noise, i.e., acquisition related noise, from the sections. These procedures could be as well applied to the CRS attribute sections and most likely will remove a lot of unwanted events from the attribute sections.

Additional to these considerations, the extension of all methods of the expanded CRS workflow to 3D and the further development of efficient implementations are mandatory to fulfill the demands of large scale data sets.

ACKNOWLEDGMENTS

- I am grateful to **Professor Dr. Dirk Gajewski** for his supervision of this work and for giving me a lot of freedom in choosing my research topics. His door was always open for me when questions about my current working topics occurred. He gave me the opportunity to produce this work and allowed me to participate in many geophysical conferences around the globe.

- I am also grateful to **Senior Lecturer Dr. Christian Hübscher** for the co-supervision of my thesis and also for allowing me to further develop my theoretical background, although the funding of my project was more practical oriented. He also made it possible for me to work out this thesis.

- I would also like to say thank you to **Dr. Tina Kaschwich from NORSAR Innovations AS** for giving me every time a useful advice and showing me that geophysics has not to be serious all the time. I also enjoyed the times together at the conferences very much.

- I am also grateful to **Dipl. Geophys. Kristina Meier** for her companionship throughout my whole studies at the University of Hamburg and for sharing an office most of my P.h.D. time in Hamburg. We always had a lot of fun together, whether it was on or off the topic. I am also grateful for proof reading my texts.

- I also like to thank **Dr. Thomas Hertweck from FUGRO Seismic Imaging** for giving me the opportunity for doing an internship in FUGRO's London office, where I could deepen my knowledge of seismics and gained some very useful experience about research and development in the industry.

- I also like to say thank you to **Dr. Ekkehart Tessmer** for managing most of my (demanding) computer requirements.

- I am as well grateful to **Dr. Mikhail Baykulov, Dipl. Geophys. Sergius Dell, Dipl. Geophys. Lutz Lüdenbach (a.k.a. le monsieur), Dr. Gesa Netzeband, Dipl. Geol. Janna Just, Dr. Claudia Vanelle, Prof. Dr. Boris Kashtan, and the applied seismic working group** for interesting discussions, good advices, and sometimes sharing the same hurdles.

- My special thanks also goes to **Christel Mynarik**, who always helped me with administration issues and always had an open ear for any kind of issues.

- I also like to thank **Professor Dr. Christian Betzler**, **Dr. Thomas Lüdmann**, and **Dr. Tina Kaschwich** for accepting my request for being part of the disputation council.

- I gratefully acknowledge the **German Research Council** and the **Wave Inversion Technology (WIT) consortium** for funding of my position and the conference attends. The Code provided by the consortium represents the basis for the work presented in this thesis.

- I like to thank **TGS-NOPEC** for providing the Eastern Mediterranean data set

- I like to thank as well **Dr. Gilles Lambaré** for the permission to use the prestack stereotomography code and the fruitful discussion

- I like to say special thank you to all **my girls and boys (you know who you are...)** for always helping my out, easing my mind, and always pulling me back on the ground. Going out, playing soccer, swimming, having a coffee together or basically doing anything is always a pleasure with friends like you.

- Obviously, I like to thank **my family** for supporting me throughout my P.h.D. and always having an open ear for me (...although you probably could not understand all the geophysical stuff I was talking about, but nevertheless you were still smiling at me).

- Last but not least, I like to thank my dear girlfriend **Dipl. Geol. Susan Wiggershaus** for her lovely patience and enormous support during my studies. You always encouraged me to push myself a bit further and could get myself out of black holes every time I was desperate by just smiling at me. You showed me what a good life-work balance means.

REFERENCES

Abdel Aal, A., El Barkooky, A., Gerrits, M., Meyer, H., Schwander, M., and Zaki, H. (2000). Tectonic evolution of the eastern Mediterranean basin and its significance for hydrocarbon prospectivity in the ultradeepwater of the Nile Delta. *The Leading edge*, pages 1086–1102.

Aksu, A., Hall, J., and Yaltirak, C. (2005). Miocene to Recent tectonic evolution of the eastern Mediterranean: New pieces of the old Mediterranean puzzle. *MARINE GEOLOGY*, 221(1-4):1–13.

Almagor, G. (1984). Salt-controlled slumping on the mediterranean slope of central israel. *MARINE GEOPHYSICAL RESEARCHES*, 6(3):227–243.

Almagor, G. (1993). Continental-slope processes off northern israel and southernmost lebanon and their relation to onshore tectonics. *MARINE GEOLOGY*, 112(1-4):151–169.

Baykulov, M., Brink, H., Gajewski, D., and Yoon, M. (2008). Revisiting the structural setting of the Gl§ckstadt Graben salt stock family, North German Basin. *Tectonophysics*.

Baykulov, M. and Gajewski, D. (2009a). Seismic data enhancement with partial Common Reflection Surface stack. *Geophysics*, 74:V49–V58.

Baykulov, M. and Gajewski, D. (2009b). Seismic data enhancement with partial Common Reflection Surface stack. *Geophysics*, 74:V49–V58.

Behura, J. (2007). Virtual Real Source. *SEG Technical Program Expanded Abstracts, San Antonio*, pages 2693–2697.

Ben-Avraham, Z., Ginzburg, A., Makris, J., and Eppelbaum, L. (2002). Crustal structure of the Levant Basin, eastern Mediterranean. *TECTONOPHYSICS*, 346(1-2):23–43. 9th Annual Workshop of the International Lithosphere Program Task Force, OLIANA, SPAIN, SEP, 1998.

Bergler, S. (2001). *The Common-Reflection-Surface Stack for Common Offset - Theory and Application*. Diploma thesis, University of Karlsruhe.

Bertoni, C. and Cartwright, J. (2006). Controls on the basinwide architecture of late Miocene (Messinian) Evaporites on the Levant margin (Eastern Mediterranean). *Sedimentary Geology*, 188-189:93–114.

Bertoni, C. and Cartwright, J. (2007). Major erosion a the end of the Messinian Salinity crisis: evidence from the Levant Basin/ Eastern Mediterrranean. *Basin Research*, 19:1–18.

Billette, F. and Lambaré, G. (1998). Velocity macro model estimation from seismic reflection data by stereotomography. *Geophysical Journal International*, 135:671–690.

Billette, F., Le Bégat, S., Podvin, P., and Lambaré, G. (2003). Practical aspects and applications of 2d stereotomography. *Geophysics*, 68(3):1008–1021.

Breman, E. (2006). Oil and gas plays in the eastern mediterranean. *5th PESGB/HGS African Conference, London*.

Buchbinder, B. and Zilberman, E. (1997). Sequence stratigraphy of Miocene-Pliocene carbonate-siliciclastic shelf deposits in the eastern Mediterranean margin (Israel): effects of eustasy and tectonics. *SEDIMENTARY GEOLOGY*, 112(1-2):7–32.

Butler, R., Spencer, S., and Griffiths, H. (1997). Transcurrent fault activity on the Dead Sea Transform in Lebanon and its implications for plate tectonics and seismic hazard. *JOURNAL OF THE GEOLOGICAL SOCIETY*, 154(Part 5):757–760.

Cartwright, J. and Jackson, M. (2008). Initiation of gravitational collapse of an evaporite basin margin: The messinian saline giant, levant basin, eastern mediterranean. *GSA Bulletin*, 120:399–413.

Carvalho, P. and Weglein, A. (1994). Wavelet estimation for surface multiple attenuation using a simulated annealing algorithm. *64th Annual International Meeting, SEG, Expanded Abstracts*, pages 1481–1484.

Chauris, H., Noble, M., Lambaré, G., and Podvin, P. (2002). Migration velocity analysis from locally coherent events in 2-d laterally heterogeneous media, Part I: theoretical aspects. *Geophysics*, 67(4):1202–1212.

Clauzon, G., Suc, J., Gautier, F., Berger, A., and Loutre, M. (1996). Alternate interpretation of the messinian salinity crisis: controversy resolved? *Geology*, 24(4):363–366.

Coleou, T. (2001). On the use of seismic velocities in model building for depth conversion. *EAGE 63rd Conference & Technical Exhibition, Amsterdam*.

Colombo, D. and DeStefano, M. (2007). Geophysical modeling via simultaneous joint inversion of seismic, gravity, and electromagnetic data: Application to prestack depth imaging. *The Leading Edge*, pages 326–331.

Colombo, D., Mantovani, M., Hallinan, S., and Virgilio, M. (2008). Sub-basalt depth imaging using simultaneous joint inversion of seismic and electromagnetic (MT) data: a CRB field study. *SEG annual meeting, Las Vegas, expanded abstracts*.

Curtis, A., Gerstoft, P., Sato, H., Snieder, R., and Wapenaar, K. (2006). Seismic interferometryÑturning noise into signal. *The Leading Edge*, (25).

Donno, D., Rocca, F., Costagliola, S., Mazzucchelli, P., and Loinger, E. (2008). Ls-dip: an adaptive dip-based subtraction of predicted multiples. *SEG Technical Program Expanded Abstracts*.

Druckman, Y., Buchbinder, B., Martinotti, G., Tov, R., and AHARON, P. (1995). The buried afiq canyon (eastern mediterranean, israel) - a case-study of a tertiary submarine-canyon exposed in late messinian times. *MARINE GEOLOGY*, 123(3-4):167–185.

Dümmong, S. (2006). *Alternative Implementation des Common Reflection Surface stacks*. Diploma thesis, University of Hamburg.

Dümmong, S. and Gajewski, D. (2008). A multiple suppression method via CRS attributes. *SEG Technical Program Expanded Abstracts*.

Dümmong, S. and Hübscher, C. (accepted 2009). Levant basin – central basin. *In: Lofi, J. (ed.) Messinian Salt Atlas. In: Lofi J., DeverchŔre J., Gorini C., Gaullier V., Gillet H., Guennoc P., Loncke L., Maillard A., Sage F. & Thinon I. (Eds.) Atlas of the Messinian seismic markers in the Mediterranean and Black Seas*.

Dümmong, S., Meier, K., Gajewski, D., and Huebscher, C. (2008). Comparison of prestack stereotomography and NIP wave tomography for velocity model building: Instances from the Messinian evaporites. *GEOPHYSICS*, 73(5, Suppl. S):291–302.

Duveneck, E. (2004a). *Tomographic determination of seismic velocity models with kinematic wavefield attributes*. Ph.D. thesis, University of Karlsruhe.

Duveneck, E. (2004b). Velocity model estimation with data-derived wavefront attributes. *Geophysics*, (65).

Duveneck, E. (2004c). Velocity model estimation with data-driven wavefront attributes. *Geophysics*, 69:265–274.

Farris, M. and Griffiths, M. (2003). Regional structural and stratigraphic framework for the eastern mediterranean Ð influence of early structure and stratigraphy on the development of the levantfrom middle jurassic to recent. *1st North Africa/Mediterranean Petroleum & Geoscience Conference & Exhibition Tunis*.

Frey-Martinez, J., Cartwright, J., and Hall, B. (2005). 3D seismic interpretation of slump complexes: example from the continental margin of israel. *Basin Research*, 17:83–108.

Gamboa, F., Filpo, E., and Tygel, M. (2003). Multiple attenuation using Common-Reflection-Surface attributes. *Wave Inversion Technology Annual report 2003*, pages 92–100.

Gardosh, M. and Druckman, Y. (2005). Stratigraphy and tectonic evolution of the Levantine basin, offshore Israel. *in A. Robertson (Ed), Tectonic Development of the Eastern Mediterranean region, Geological Society Special Publication*.

Garfunkel, Z. (1981). Internal structure of the dead-sea leaky transform (rift) in relation to plate kinematics. *TECTONOPHYSICS*, 80(1-4):81–108.

Garfunkel, Z. (2004). Origin of the Eastern Mediterranean basin: a reevaluation. *TECTONOPHYSICS*, 391(1-4):11–34. 1st International Symposium on Earth Sciences and Engineering, Istanbul, TURKEY, MAY 16-18, 2002.

Garfunkel, Z. and Almagor, G. (1984). Geology and structure of the continental-margin off northern israel and the adjacent part of the levantine basin. *MARINE GEOLOGY*, 62(1-2):105–131.

Garfunkel, Z., Arad, A., and Almagor, A. (1979). The Palmahim Disturbance and its regional setting. *Geological Survey of Israel Bulletin*, 72:56.

Gargani, J. and Rigollet, C. (2007). Mediterranean Sea level variations during the Messinian salinity crisis. *GEOPHYSICAL RESEARCH LETTERS*, 34(10).

Gelchinsky, B., Landa, E., and Shtivelman, V. (1985). Algorithms of group and phase correlations. *Geophysics*, 4(50):596–608.

Ginzburg, A., Cohen, S., Hayroe, H., and Rosenzweig, A. (1975). Geology of mediterranean shelf of israel. *AAPG BULLETIN-AMERICAN ASSOCIATION OF PETROLEUM GEOLOGISTS*, 59(11):2142–2160.

Girdler, R. and Southren, T. (1987). Structure and evolution of the northern red-sea. *NATURE*, 330(6150):716–721.

Gradmann, S., Hübscher, C., Ben-Avraham, Z., Gajewski, D., and Netzeband, G. (2005). Salt tectonics off northern israel. *Marine and Petroleum Geology*, 22:597–611.

Hale, D. (2007). A method for estimating apparent displacement vectors from time-lapse seismic image. *SEG Expanded Abstracts 26*.

Heilmann, Z., Mann, J., and Koglin, I. (2006). CRS-stack-based seismic imaging considering top-surface topography. *Geophysical Prospecting*, 50(4):681–695.

Heincke, B., Jegen, M., and Hobbs, R. (2006). Joint inversion of mt, gravity and seismic data applied to sub-basalt imaging. *SEG annual meeting, New Orleans, expanded abstracts*.

Herrmann, F. and Verschuur, D. (2004). Separation of primaries and multiples by non-linear estimation in the curvelet domain. *66th Annual International Meeting, EAGE, expanded abstracts*.

Hertweck, T., Mann, J., and Klüver, T. (2005). Event-consistent smoothing in the context of the CRS stack method. *Journal of Seismic Exploration*, 14:197–215.

Hertweck, T., Schleicher, J., and Mann, J. (2007a). Data stacking beyond CMP. *The Leading Edge*, (26).

Hertweck, T., Schleicher, J., and Mann, J. (2007b). Data stacking beyond CMP. *The leading Edge*, pages 818–827.

Hoeber, H., Coleou, T., Le Meur, D., Angerer, E., Lanfranchi, P., and Lecerf, D. (2003). On the use of geostatistical filtering techniques in seismic processing. *SEG annual meeting*.

Hofstetter, A., vanEck, T., and Shapira, A. (1996). Seismic activity along fault branches of the Dead Sea Jordan transform system: The Carmel-Tirtza fault system. *TECTONOPHYSICS*, 267(1-4):317–330.

Hsü, K., Cita, M., and Ryan, W. (1980). *The origin of the Mediterranean Evaporites*. U.S. Govt. Printing Office, Washington D.C.

Hubral, P. and Krey, T. (1980). *Interval velocities from seismic reflection traveltime measurements*. Soc. Expl. Geophys.

Hübscher, C., Cartwright, J., Cypionka, H., De Lange, G., Robertson, A., Suc, J., and Urai, J. (2007). Global look at salt giants. *EOS*, 88(16):177–179.

Hübscher, C. and Netzeband, G. (2007a). Evolution of a young salt giant: The example of the Messinian evaporates in the Levantine basin. *Mechanical behaviour of salt - understanding the THMC processes in salt, proceedings and monographs in engineering, water and earth sciences*, pages 175–182.

Hübscher, C. and Netzeband, G. (2007b). Evolution of a young salt giant: The example of the Messinian evaporites in the Levante basin. *In: Wallner, M.; Lux, K.-H.; Minkley, W.; Hardy, Jr., H.R. (Eds.) The Mechanical behavior of Salt - Understanding of THMC Processes of Salt, Taylor and Francis Group, London*, pages 175–184.

Hübscher, C., Tahchi, E., Klaucke, I., Maillard, A., and Sahling, H. (2009). Salt tectonics and mud volcanism in the latakia and cyprus basins, eastern mediterranean. *TECTONOPHYSICS*, 470:173–182.

Jabukowicz, H. (1998). Wave Equation Prediction and Removal of Interbed Multiples. *60th Meeting, EAGE, expanded abstracts*.

Jäger, R., Mann, J., Höcht, G., and Hubral, P. (2001). Common-Reflection-Surface stack: Image and attributes. *Geophysics*, 66:97–109.

Karna, D., Agarwal, S., and Nikam, S. (2008). Normalized Cross-correlation based Fingerprint Matching. *Computer Graphics, Imaging and Visualisation - modern techniques and applications, proceedings*.

Kearey, P. and Brooks, M. (1991). *An Introduction to Geophysical Exploration*. Blackwell Science, Oxford.

Kelamis, P. and Verschuur, D. (1996). Multiple elimination strategies for land data. *58th Meeting, EAGE, Expanded abstracts*, page B001.

Kempler, D. and Garfunkel, Z. (1994). Structures and kinematics in the northeastern mediterranean - a study of an irregular plate boundary. *TECTONOPHYSICS*, 234(1-2):19–32. Symposium on the Tectonics of the Eastern Mediterranean and Analogous Regions, at the XVII General Assembly of the European-Geophysical-Society, EDINBURGH, SCOTLAND, APR 08, 1992.

Kirkpatrick, S., Gelatt, C., and Vecchi, M. (1983). Optimisation by simulated annealing. *Science*, 220(4598):671–680.

Klüver, T. (2006). Velocity model building using migration to residual time. *SEG Technical Program Expanded Abstracts*, pages 2022–2026.

Klüver, T. and Mann, J. (2005). Event-consistent smoothing and automated picking in CRS-based seismic imaging. *SEG Technical Program Expanded Abstracts*, (24).

Koglin, I. (2005). *Estimation of residual static time shifts by means of the CRS based residual static correction approach*. Logos Verlag, Berlin.

Krijgsman, W., Hilgen, F., Raffi, I., Sierro, F., and Wilson, D. (1999). Chronology, causes and progression of the messinian salinity crisis. *Nature*, 400:652–655.

Lambaré, G., Alerini, M., Baina, R., and Podvin, P. (2004). Stereotomography: a semi-automatic approach for velocity macromodel estimation. *Geophysical Prospecting*, 52:671–681.

Letourzey, J., Coletta, R., and Chermette, J. (1995). Evolution of salt related structures in compressional settings. *in Jackson, M.P.A., Roberts, D.J., Snelson, S. (Eds), Salt Tectonics: A Global Perspective, vol. 65 AAPG memoir Tulsa, Oklahoma, USA*.

Loncke, L., Gaullier, V., Mascle, J., Vendeville, B., and Camera, L. (2006). The Nile deep-sea fan: An example of interacting sedimentation, salt tectonics, and inherited subsalt paleotopographic features. *MARINE AND PETROLEUM GEOLOGY*, 23(3):297–315.

MacKay, S. and Abma, R. (1992). Imaging and velocity estimation with depth-focussing analysis. *Geophysics*, 57:1608–1622.

Maillard, A., Gorini, C., Mauffret, A., Sage, F., Lofi, J., and Gaullier, V. (2006). Offshore evidence of polyphase erosion in the Valencia basin (Northwestern Mediterranean): Scenario for the Messinian Salinity Crisis. *SEDIMENTARY GEOLOGY*, 188(Sp. Iss. SI):69–91.

Mann, J. (2002). *Extensions and Applications of the Common-Reflection-Surface Stack Method*. Ph. D. thesis, University of Karlsruhe.

Mart, Y. and Bengai, Y. (1982). Some depositional patterns at continental-margin of southeastern mediterranean-sea. *AAPG BULLETIN-AMERICAN ASSOCIATION OF PETROLEUM GEOLOGISTS*, 66(4):460–470.

Mascle, J., Benkhelil, J., Bellaiche, G., Zitter, T., Woodside, J., Loncke, L., and Prismed II Sci Party (2000). Marine geologic evidence for a Levantine-Sinai plate, a new piece of the Mediterranean puzzle. *GEOLOGY*, 28(9):779–782.

Matheron, G. (1982). Pour une analyse krigeante des donnees regionalisees. *Report N-732, Centre de Geostatistique, ENSMP*.

Mayne, W. (1962). Common reflection point horizontal data stacking techniques. *Geophysics*, 27:927–938.

Mitchum, R., Vail, J., and Sangree, J. (1977). Seismic stratigraphy and global changes of sea-level, part 6: seismic stratigraphic interpretation procedure. *In: Seismic Stratigraphy - applications to Hydrocarbon exploration, American Association of Petroleum Geologists Memoirs*, 26:117–134.

Müller, G. (2001). *Digitale Signalbearbeitung*. Lecture notes, University of Hamburg.

Müller, N. (2007). *Determination of interval velocities by inversion of kinematic 3D wavefield attributes*. Ph. D. thesis, University of Karlsruhe.

Müller, T. (1999). *Die Methode des Common Reflection Surface stacks*. Logos Verlag, Berlin.

Neelamani, R., Baumstein, A., and Ross, W. (2008). Complex Curvelet-based Adaptive Subtraction of Several Noise Templates. *SEG Technical Program Expanded Abstracts*.

Neev, D. (1975). Tectonic evolution of middle-east and levantine basin (easternmost mediterranean). *GEOLOGY*, 3(12):683–686.

Neidell, N. and Taner, M. (1971). Semblance and other coherency measures for multichannel data. *Geophysics*, 71:482–497.

Nelder, J. and Mead, R. (1965). A simplex method for function minimization. *Computer Journal*, (7):308–313.

Netzeband, G., Gohl, K., C., H., Ben-Avraham, Z., Dehghani, A., Gajewski, D., and Liersch, P. (2006a). The Levantine Basin - crustal structure and origin. *Tectonophysics*, 418:178–188.

Netzeband, G., Hübscher, C., and Gajewski, D. (2006b). The structural evolution of the Messinian Evaporites in the Levantine Basin. *Marine Geology*, 230:249–273.

Oldenburg, D. (1974). Inversion and interpretation of gravity anomalies. *GEOPHYSICS*, 39(4):526–536.

Parker, R. (1972). Inverse theory with grossly inadequate data. *GEOPHYSICAL JOURNAL OF THE ROYAL ASTRONOMICAL SOCIETY*, 29(2):123–&.

Peacook, K. and Treitel, S. (1969). Predictive Deconvolution: Theory and Practice. *Geophysics*, 34(155).

Perez-Careta, E., Torres-Cisneros, M., Avina-Cervantes, J., Debeir, O., Ibarra-Manzano, O., Aguilera-Gomez, E., Perez-Pantoja, E., and Negrete-Romero, G. (2008). Cell Recognition and Tracking Using Nonlinear Cross-Correlation. *Digest of the Leos summer topical meetings*.

Piromallo, C. and Morelli, A. (2003). P wave tomography of the mantle under the alpine-mediterranean area. *Journal of Geophysical Research*, 108.

Press, W., Teukolsky, S., Vetterling, W., and Flannery, B. (2002). *Numerical Recipes in C++, Second Edition*. Cambridge University Press.

Roberts, G. and Peace, D. (2007). Hydrocarbon plays and prospectivity of the Levantine Basin, offshore Lebanon and Syria from modern seismic data. *GEOARABIA*, 12(3):99–124.

Robertson, A. and Comas, M. (1998). Collision-related processes in the mediterranean region - introduction. *TECTONOPHYSICS*, 298:1–4.

Rouchy, J. M. and Caruso, A. (2006). The Messinian salinity crisis in the Mediterranean basin: A reassessment of the data and an integrated scenario. *SEDIMENTARY GEOLOGY*, 188(Sp. Iss. SI):35–67.

Ryan, B., Stanley, D., Hersey, J., Fahlquist, D., and Allan, T. (1970). The tectonics of the mediterranean sea. *In: Maxwell, A.E. (Ed.), The Sea, 4. Wiley, New York*, pages 387–491.

Ryo, J. (1982). Decomposition (decom) approach applied to wave-field analysis with seismic reflection records. *Geophysics*, pages 869–883.

Santos, L., Schleicher, J., Costa, J., and Novais, A. (2008). Fast estimation of CRS parameters using local slopes. *WIT annual report*, pages 219–229.

Schattner, U., Ben-Avraham, Z., Lazar, M., and Hueebscher, C. (2006). Tectonic isolation of the Levant basin offshore Galilee-Lebanon - effects of the Dead Sea fault plate boundary on the Levant continental margin, eastern Mediterranean. *JOURNAL OF STRUCTURAL GEOLOGY*, 28(11):2049–2066. Symposium on Tectonic Inversion Processes and Structural Inheritance in Mountain Belts, Florence, ITALY, AUG, 2004.

Schleicher, J., Hubral, P., Tygel, M., and Jaya, M. (1997). Minimum apertures and fresnel zones in migration and demigration. *Geophysics*, 62:183–194.

Spinner, M. and Mann, J. (2007). CRS-based minimum-aperture time migration - a 2D land data case study. *77th Annual Internat. Mtg., Soc. Expl. Geophys., Session SPMI 6.4., Ext. Abstr., San Antonio*.

Stampfli, G. and Borel, G. (2002). A plate tectonic model for the Paleozoic and Mesozoic constrained by dynamic plate boundaries and restored synthetic oceanic isochrons. *EARTH AND PLANETARY SCIENCE LETTERS*, 196(1-2):17–33.

Sword, C. (1987). *Tomographic Determination of Interval Velocities from Reflection Seismic Data: The method of controlled directional reception*. Ph.D. thesis, Stanford University.

Tibor, G., Ben-Avraham, Z., Streckler, M., and Fligelman, H. (1992). Late tertiary subsidence history of the southern levant margin, eastern mediterranean-sea, and its implications to the understanding of the messinian event. *JOURNAL OF GEOPHYSICAL RESEARCH-SOLID EARTH*, 97(B12):17593–17614.

Vanelle, C. (2002). *Traveltime based true amplitude migration*. P.h.D. thesis, University of Hamburg.

Vendeville, B. (1999). Salt complexity out of repeated simplicity. *in American Association of Petroleum Geologists 1999 annual meeting, Annual Meeting Expanded Abstracts - American Association of Petroleum Geologists*.

Verschuur, D. (2006). *Seismic multiple removal techniques*. EAGE Publications.

Verschuur, D. and Berkhout, A. (1997). Estimation of multiple scattering by iterative inversion, Part II: Practical aspects and examples. *Geophysics*, 62:1596–1611.

Verschuur, D., Berkhout, A., and Wapenaar, C. (1992). Adaptive surface-related multiple elimination. *Geophysics*, pages 1166–1177.

Vidal, N., Klaeschen, D., Kopf, A., Docherty, C., Von Huene, R., and Krasheninnikov, V. (2000). Seismic images at the convergence zone from south of Cyprus to the Syrian coast, eastern Mediterranean. *TECTONOPHYSICS*, 329(1-4):157–170. 8th International Symposium on Deep Seismic Profiling of the Continents and their Margins, BARCELONA, SPAIN, SEP 20-25, 1998.

von Steht, M. and Mann, J. (2008). Velocity calibration and wavefield decomposition for walkover VSP data. *78th Annual Internat. Mtg., Soc. Expl. Geophys., Ext. Abstr., Las Vegas*.

Walley, C. (1998). Some outstanding issues in the geology of Lebanon and their importance in the tectonic evolution of the Levantine region. *TECTONOPHYSICS*, 298(1-3):37–62.

Warren, J. (2006). *Evaporites: sediments, resources and hydrocarbons*. Birkhäuser.

Wegelein, A., Gasparotto, F., Carvalho, P., and Stolt, R. (1997). An inverse-scattering series method for attenuating multiple reflections in seismic data. *Geophysics*, pages 1975–1989.

Woollard, G. (1979). New gravity system - changes in international gravity base values and anomaly values. *GEOPHYSICS*, 44(8):1352–1366.

Yilmaz, O. (2001). *Seismic data analyses*. Society of Exploration Geophysicists, Tulsa.

Zak, I. and Freund, R. (1981). Asymmetry and basin migration in the dead-sea rift. *TECTONOPHYSICS*, 80(1-4):27–38.

Zhang, Y. (2003). *Common-Reflection-Surface stack and the handling of top surface topography*. Logos Verlag, Berlin.